


**UCC Library and UCC researchers have made this item openly available.  
Please [let us know](#) how this has helped you. Thanks!**

<b>Title</b>	Quantitative textural analysis of sedimentary grains and basin subsidence modelling
<b>Author(s)</b>	Tunwal, Mohit
<b>Publication date</b>	2018
<b>Original citation</b>	Tunwal, M. 2018. Quantitative textural analysis of sedimentary grains and basin subsidence modelling. PhD Thesis, University College Cork.
<b>Type of publication</b>	Doctoral thesis
<b>Rights</b>	© 2018, Mohit Tunwal. <a href="http://creativecommons.org/licenses/by-nc-nd/3.0/">http://creativecommons.org/licenses/by-nc-nd/3.0/</a> 
<b>Embargo information</b>	Not applicable
<b>Item downloaded from</b>	<a href="http://hdl.handle.net/10468/7114">http://hdl.handle.net/10468/7114</a>

Downloaded on 2020-06-06T00:45:06Z

# **Quantitative textural analysis of sedimentary grains and basin subsidence modelling**

Thesis presented by

**Mohit Tunwal, Int. M.Tech.**

For the degree of

**Doctor of Philosophy**

National University of Ireland, Cork.

Geology, School of Biological, Earth and Environmental Sciences

February, 2018

Supervisors: Dr. Kieran F. Mulchrone, Dr. Patrick A. Meere

Advisor: Dr. David Jarvis

Head of Discipline: Prof. Andrew J. Wheeler

Head of School: Prof. Sarah C. Culloty

# Content

1 Introduction.....	1
1.1 Part 1 Textural characterisation of sedimentary grains.....	1
1.1.1 Basic concepts.....	1
1.1.2 Recent developments.....	3
1.1.3 Application of grain shape.....	4
1.1.4 Aims and objectives.....	5
1.2 Part 2 Basin subsidence modelling.....	6
1.2.1 Basic concepts.....	6
1.2.2 McKenzie Model.....	7
1.2.2.1 Instantaneous stretching.....	7
1.2.2.2 Thermal relaxation .....	10
1.2.3 Modification to the McKenzie Model.....	14
1.2.4 Aims and objectives.....	15
1.3 References.....	15
2 Mathematica code for quantitative characterisation of sedimentary grains.....	21
2.1 Introduction.....	22
2.2 Parameter for grain characterisation.....	24
2.2.1 Grain size.....	24
2.2.2 Grain shape.....	25
2.2.2.1 Roundness.....	25
2.2.2.2 Sphericity and Circularity.....	28

2.2.2.3 Irregularity.....	29
2.2.2.4 Angularity.....	32
2.2.2.5 Fractal dimension.....	33
2.2.2.6 Fourier method.....	35
2.2.2.7 Other Parameters.....	40
2.3 Methodology.....	40
2.4 Mathematica code.....	41
2.4.1 Image Analysis.....	41
2.4.2 Feature Extraction.....	42
2.4.3 Computation of shape and size.....	43
2.4.4 Results.....	44
2.5 Example analysis.....	44
2.5.1 Rock thin section.....	45
2.5.1 Loose sediment.....	48
2.6 Discussion.....	51
2.7 Conclusion.....	52
2.8 Acknowledgement.....	52
2.9 References.....	53
3 Quantitative characterisation of grain shape: Implications for textural maturity analysis and discrimination between depositional environments.....	57
3.1 Introduction.....	58
3.2 Sampling.....	60
3.3 Methodology.....	64
3.3.1 Image acquisition.....	64
3.3.2 Shape parameters.....	66

3.3.2.1 Roundness.....	66
3.3.2.2 Circularity.....	66
3.3.2.3 Angularity.....	68
3.3.2.4 Irregularity.....	68
3.3.2.5 Fractal Dimension.....	70
3.3.2.6 Other Parameters .....	70
3.3.3 Statistical analysis.....	71
3.4 Results.....	73
3.5 Discussion.....	80
3.6 Conclusion.....	84
3.7 Acknowledgement.....	84
3.8 References.....	85
4 A new approach to grain shape quantification using Inverse Radius of Curvature (IRC).....	89
4.1 Introduction.....	90
4.2 Shape quantification method.....	92
4.2.1 Scaling of grain boundary.....	92
4.2.2 Inverse Radius of Curvature (IRC) plot.....	93
4.2.3 Corner identification.....	93
4.2.4 Shape parameters for grain characterisation using the IRC.....	95
4.2.4.1 Number of Corners ( $v$ ).....	95
4.2.4.2 Cumulative Angularity ( $\alpha$ ).....	95
4.2.4.3 Sharpest Corner ( $\eta$ ).....	95
4.2.4.4 Straight Fraction ( $\phi$ ).....	95
4.3 Application to natural grains.....	97

4.3.1 Sampling sites.....	97
4.3.2 Sample treatment and image acquisition.....	98
4.4 Results.....	99
4.4.1 Assessment of Shape Parameters.....	99
4.4.1.1 $\eta$ vs $v$ plot.....	101
4.4.1.2 $\alpha$ vs $\eta$ plot.....	101
4.4.1.3 $\varphi$ vs $v$ plot.....	101
4.4.1.4 $\varphi$ vs $\alpha$ plot.....	101
4.4.1.5 $\alpha$ vs $v$ plot.....	102
4.4.1.6 $\varphi$ vs $\eta$ plot.....	102
4.4.2 Variation of shape parameters within sample.....	103
4.5 Discussion.....	106
4.6 Conclusion.....	111
4.7 Acknowledgement.....	112
4.8 References.....	113
5 Constraining basin parameters using a known subsidence history.....	114
5.1 Introduction.....	117
5.2 Numerical model.....	118
5.2.1 Initial Stretching.....	118
5.2.2 Gradual Subsidence.....	122
5.3 Curve fitting method.....	126
5.4 Case study.....	131
5.5 Conclusion.....	133
5.6 Acknowledgement.....	134
5.7 References.....	134

6 Conclusion.....	138
-------------------	-----

## List of Figures

Figure 1.1	Uniform stretching of a basin.....	10
Figure 1.2	Thermal transient representing solution of heat equation.....	12
Figure 1.3	Lithospheric configuration representing isostatic balance at time $t$ ..	14
Figure 2.1	Roundness measurement of a grain boundary.....	27
Figure 2.2	Circularity of a grain boundary.....	29
Figure 2.3	Diagram representing measurement of irregularity parameter after Blott and Pye, (2008).....	30
Figure 2.4	Measurement of grain irregularity.....	31
Figure 2.5	Angularity of a grain boundary.....	33
Figure 2.6	Fractal dimension calculation for a grain using the divider method.	34
Figure 2.7	Unrolling of a grain boundary.....	36
Figure 2.8	Grain boundary showing re-entrant angle problem.....	37
Figure 2.9	Reconstructed particle boundary with Fourier descriptors.....	39
Figure 2.10	Image analysis routine for thin section analysis.....	46
Figure 2.11	Result from thin section photomicrograph analysis of sandstone sample.....	47
Figure 2.12	Image analysis routine for loose sediment analysis.....	49

Figure 2.13	Results from photomicrograph analysis of loose sediment sample..	50
Figure 3.1	Map showing sampling locations for fluvial, glacial and beach samples in Ireland.....	61
Figure 3.2	Map of India showing sampling location for aeolian samples.....	62
Figure 3.3	Image acquisition of sand grains.....	65
Figure 3.4	Roundness measurement of a grain using image analysis technique	67
Figure 3.5	Angularity measurement of a grain by modified Rao et al. (2002)..	68
Figure 3.6	Irregularity measurement of a grain.....	69
Figure 3.7	Fractal dimension calculation for a grain using the divider method.	71
Figure 3.8	Box-plots showing the shape parameter distributions of the samples.....	74
Figure 3.9	Bivariate plots of comparing mean of shape parameters for the samples.....	75
Figure 3.10	Dendogram showing proximal relationship amongst the samples...	79
Figure 3.11	Bivariate plot for mean angularity versus mean fractal dimension...	82
Figure 4.1	Example of grain boundaries with roundness value of 0.60.....	92
Figure 4.2	Inverse Radius of Curvature calculation .....	94
Figure 4.3	IRC plots with their corresponding grain boundaries.....	96
Figure 4.4	Bivariate plots showing distribution of grains for the new shape parameters.....	100
Figure 4.5	Box-Whiskers plot showing distribution of $v$ , $\alpha$ , $\eta$ and $\phi$ values.....	103
Figure 4.6	Probability distribution plots showing distribution of $v$ , $\alpha$ , $\eta$ and $\phi$ values.....	104
Figure 4.7	Dendogram showing proximal relationship between the samples...	105



Figure 4.8	Regions within the bivariate plots indicating the grain shape characteristics for the new shape parameters.....	107
Figure 4.9	Bivariate plots of circularity and roundness .....	109
Figure 5.1	Basin configuration before and after uniform initial stretching.....	119
Figure 5.2	Basin configuration during thermal relaxation phase.....	123
Figure 5.3	Contour-Plot of $E_1$ and $E_2$ for comparison between known subsidence profile with the curves generated from subsidence models.....	129
Figure 5.4	Comparison between four synthetically generated subsidence curves and the subsidence models.....	130
Figure 5.5	Curve fitting method applied to the case study of Campos Basin...	133

## List of Tables

Table 2.1	List of size parameters implemented in the software package.....	25
Table 2.2	Table of simple geometrical parameters used in the study.....	40
Table 3.1	Details of samples collected for the study.....	63
Table 3.2	Table of simple geometrical parameters used in the study.....	70
Table 3.3	Pearson's correlation matrix showing correlation between shape parameters.....	76
Table 3.4	Comparative results for Kruskal-Wallis and ad hoc Dunn tests.....	76

Table 3.5	Importance of shape parameter.....	80
Table 4.1	Details of samples collected for the study.....	98
Table 4.2	Pearson’s correlation matrix showing correlation of the new shape parameters.....	102
Table 4.3	Table showing percentage of sediment grains from each environment.....	105
Table 4.4	Contrasting results from the new shape parameters and existing roundness and circularity parameter.....	110

## List of Abbreviations

AI	Angularity Index, angularity using outline slope
*.bmp	Bitmap image file
CART	Classification And Regression Tree
GRAD	Gradient Angularity Index
Q-Q	Quantile-Quantile
SAI	Smoothing Angularity Index
SEM	Scanning Electron Microscope

## **Declaration**

This is to certify that the work I am submitting is my own and has not been submitted for another degree, either at University College Cork or elsewhere. All external references and sources are clearly acknowledged and identified within the contents. I have read and understood the regulations of University College Cork concerning plagiarism.

Signed

Mohit Tunwal, author.

## **Acknowledgement**

Ph.D. is a journey in which the candidate quests for knowledge in an uncharted territory. This journey from beginning to the end is shaped by various people who meet enroute, walk along and make the journey exciting or even bear the torch in front and guide for the whole duration. I take this opportunity to acknowledge every such person for making it possible for me to bring this Ph.D. to conclusion.

First and foremost, I would like to thank my Principal Supervisor and mentor, Dr. Kieran Mulchrone, for guiding me on this Ph.D. For a research topic involving diverse concepts of geology, maths and computation, I could not think of a better person for my supervisor. It has been an absolute pleasure for me to work with him. He was there with a solution or a suggestion to tackle each problem I encountered. I was always given a room to debate and discuss ideas which led to unfold some novel approaches that were applied in this work. He trusted me at different stages and was always patient in dealing with me. I learned a lot from him, as a person and as a researcher, and this Ph.D. would not have been possible without his encouragement.

I am grateful to my Co-Supervisor, Dr. Pat Meere, for all the guidance and help he provided me during the Ph.D. He was always approachable for all the academic and administrative work, issued countless number of letters proving again and again that I am a legitimate student working at UCC. He took time out from his busy schedule to help me out in sampling and encouraged me at various stages to attend workshop and conferences. Both Kieran and Pat were wonderful supervisors and I'm blessed to have worked with them.

I am thankful to the academic staff at the Geology Department, UCC. The list includes Prof. Andy Wheeler, Dr. Ed Jarvis, Dr. Reginald J. Reavy and Dr. Maria McNamara. Andy has been of great help as the head of the discipline. I would like to give special thanks to Ed, a great guy to have as a Ph.D. advisor. He was there to advise me and have chat about cricket. John introduced me to the concept of ginoclock, without which geology department wouldn't be as charming as it is now.

The technical staff at Cooperage, especially Ms. Mary Lehane, was very kind and helpful for the sample processing work that I had carry out. I would like to thank Dr. Richard Unitt for his help in the Microscopy work. I am grateful to Ms. Eileen McCarthy for the helpful advise he offered to me.

I would like to thank the administrative staff: Prof. Sarah Culloty, Ms. Elaine Kelly, Ms. Mary McSweeney, Ms. Phil Fogaty and everyone I may have missed for all the work they have done for me whenever I have approached them and a lot of times behind the scenes. The life of an academician can only be easy because of them.

During the four years of my Ph.D., I attended a number of workshops and short courses at various places. I would like to thank each and everyone of them. They significantly broadened my knowledge in the field of my research and made it possible for me to learn a lot in a short duration.

I would like to acknowledge the great time I had sharing office space with various intellectuals, in particular, Dr. Lim and Dr. Fairey. The rituals of office Olympics made the life easier and fun filled. Special thanks to Aaron for all the GIS help he provided. Brenton has been kind enough to help me out in the field work and rock cutting. I could work peacefully at the office because I was relaxed most of the times at home, the home which changed from Upside down house to side ways house to now

fully upright house. In the process, I lived with really nice people: Ben, Brenton, Aidan, Juergen, Rob and now Siobhan and Pooja. Special thanks to Ben for organising a lot of house stuff and taking pressure off from rest of us. When I arrived at UCC, Dr. Dave Mccarthy helped me out starting with Mathematica. A lot of Postgrads at UCC were around and are now around who made this journey a lot more fun. A big shout to them: Greg, Darren, Juergen, Nidia, Siobhan, Valentina, Odhran and Aidan. Talking about Aidan, I must thank Holly without whom he would not have gone back to Australia leaving behind funds in the project which allowed me to finish this Ph.D.

I am grateful to Adnan Haq and Siddharth Kabra for the statistics related discussion I had with them which immensely helped the data analysis section of the thesis. I would like to acknowledge the effort taken by Tushar Bishnoi and Vibhore Goyal for reviewing various sections of the thesis.

Last but not the least, I must thank my family who provided constant support during the last four years of the Ph.D. It was possible for me to pursue this Ph.D., living away far from home, because they were always there on the other side of the world wishing for my success and providing support wherever possible.

## **Funding Acknowledgement**

*This project is funded by the Irish Shelf Petroleum Studies Group (ISPSG) of the Irish Petroleum Infrastructure Programme (PIP) Group 4. The ISPSG comprises: Atlantic Petroleum (Ireland) Ltd, Cairn Energy Plc, Chrysaor E&P Ireland Ltd, Chevron North Sea Limited, ENI Ireland BV, Europa Oil & Gas (Holdings) plc, ExxonMobil E&P Ireland (Offshore) Ltd., Kosmos Energy LLC, Maersk Oil North Sea UK Ltd, Petroleum Affairs Division of the Department of Communications, Energy and Natural Resources, Providence Resources plc, Repsol Exploración SA, San Leon Energy Plc, Serica Energy Plc, Shell E&P Ireland Ltd, Sosina Exploration Ltd, Statoil (UK) Ltd, Tullow Oil Plc and Woodside Energy (Ireland) Pty Ltd.*

# Abstract

## Part 1: Quantitative textural analysis

Shape analysis can provide important information regarding the origin, transport and deposition history of grains. Particle shape measurement has been an active area of research for sedimentologists since the 20th century. However, there is a lack of standardised methodology for quantitative characterisation of grain shapes. The main objective of this work is to develop methodologies that can be used by sedimentologists for quantitative textural analysis of grains such that the results obtained are comparable. A modular suite of code written in the Mathematica environment for the quantitative characterisation of sedimentary grains in 2-dimensions is presented. This image analysis package can be used to analyse consolidated as well as loose sediment samples. Using newly implemented image analysis methods, 20 loose sediment samples from four known depositional environments (beach, aeolian, glacial and fluvial) were analysed. This research aims to identify the most useful shape parameters for textural characterisation of populations of grains and determine the relative importance of the parameters. A key aspect of this study is to determine whether, in a particular sedimentary environment, textural maturity of the samples can be ranked based on their grain shape data. Furthermore, discrimination of sedimentary depositional environments is explored on the basis of grain shape. The available shape parameters suffer from a common shortcoming that particles, which are visually distinct, are not differentiated. To address this issue, the Inverse Radius of Curvature (IRC) plot which can be used to identify corners and measure their sharpness is introduced. Using the IRC plot, four shape parameters are proposed: number of corners, cumulative angularity, sharpest corner and straight fraction. This methodology is applied to a 4000 sand grain dataset. The textural analysis software package developed here allow users to quantitatively characterise large set of grains with a fast, cheap and robust methodology. This study indicate that textural maturity is readily categorised using automated grain shape parameter analysis. However, it is not possible to absolutely discriminate between different depositional environments on the basis of shape parameters alone. The four new shape parameters proposed here based on the IRC plot can be collectively used to quantitatively describe grains shape which correlates closely with visual



perceptions. This work opens up the possibility of using detailed quantitative textural dataset of sediment grains along with other standard analyses (mineralogy, bulk composition, isotopic analysis, etc) for diverse sedimentary studies.

## Part 2: Basin modelling

Subsidence modelling is an important part of basin analysis to better understand the tectonic evolution of sedimentary basins. The McKenzie model has been widely applied for subsidence modelling and stretching factor estimation for sedimentary basins formed in an extensional tectonic environment. In this contribution, a numerical model is presented that takes into account the effect of sedimentary cover on stretching factor estimation. Subsidence modelling requires values of physical parameters (crustal thickness, lithospheric thickness, stretching factor, etc.) which may not be always available. With a given subsidence history of a basin estimated using a stratigraphic backstripping method, these parameters can be estimated by quantitatively comparing the known subsidence curve with modelled subsidence curves. In this contribution, a method to compare known and modelled subsidence curves is presented aiming to constrain valid combinations of stretching factor, crustal thickness and lithospheric thickness of a basin. The parameter fitting method presented here is first applied to synthetically generated subsidence curves. Next, a case study using a known subsidence curve from the Campos Basin, offshore Brazil is considered. The range of stretching factors estimated for the Campos basin from this study is in accordance with previous work, with an additional estimate of corresponding lithospheric thickness. This study provides insights into the dependence of subsidence modelling methods on assumptions about input parameters as well as allowing for the estimation of valid combinations of physical lithospheric parameters, where the subsidence history is known.

# 1 Introduction

The research presented in this Ph.D. is in two distinct parts. The first part of the thesis deals with the textural characterisation of sedimentary grains. This part comprises Chapters 2, 3, and 4 of the thesis. The second part, comprising Chapter 5, concerns basin subsidence modelling. The first chapter introduces the basic concepts and provides a brief review of previous work. The aims and objectives of the two parts follows their respective introduction. The conclusion of the thesis is summarised in the last chapter (Chapter 6).

## 1.1 Part 1 Textural characterisation of sedimentary grains

### 1.1.1 Basic concepts

The definition of shape according to the Cambridge dictionary is "*the particular physical form or appearance of something*". Every solid object embodies a shape as perceived visually by humans. The physical form is 3 dimensional in nature and can vary to a great extent. The shape of an object as viewed in its final form is the result of the processes it has experienced from its formation up to its present form. Thus, researchers in various fields (Geology, Biology, Civil Engineering, Powder Technology to name a few) have taken an active interest in quantifying shapes so that different objects can be compared by virtue of their physical form.

The shape of sedimentary particles captivated the attention of sedimentologists for decades since the 20th century (Barrett, 1980; Blott and Pye, 2008 and references therein). The abrasive process that the clastic grains encounter during transportation and deposition alters their shape. Other factors that influence the shape of clastic grains are their mineralogy, composition and size (Friedman and Sanders, 1978). This led to numerous studies in which the concept of particle shape was defined, revised and improved upon (Barrett, 1980; Blott and Pye, 2008). As a result, a number of different

terminologies were used by different authors. This study follows the convention laid out in a recent review study (Blott and Pye, 2008) of particle shape, where the term “*morphology*” is used to describe the overall external expression consisting of two components: “*shape*” and “*surface texture*”. The shape characterises the broad and medium scale features of the particle morphology, whereas, surface texture concerns with the small scale surface features of the grain.

In sedimentology, the most commonly used aspects of shape are: form, sphericity and roundness. Form is described by the three orthogonal axes: longest (L), intermediate (I) and shortest (S) of the particle representing its tri-dimensional characteristics (Blott and Pye, 2008). The representation of form in terms of a binary plot of I/L and S/I ratios was first attempted by Zingg (1935) and later improved upon by others (Krumbein, 1941; Krumbein and Pettijohn, 1938).

The term sphericity and roundness were considered to be same by early researchers (Barrett, 1980), however, it was later demonstrated that they are different aspects of shape (Wadell, 1932). Sphericity is a measure of how close the shape of particle is to that of a sphere. Due to practical limitations of measuring sphericity parameters, a number of researchers focused on measuring circularity of particles in their 2-Dimensional projection (Riley, 1941; Wadell, 1933). The work in this thesis focuses on 2-Dimensional shape parameters.

Roundness of a particle is described as the roundness of its corners. The corners are the portions of the particle boundary, where the radius of curvature is lower than the radius of curvature of the largest inscribing circle (Wadell, 1932). The measure of roundness is taken to be the average radius of curvature of the corners divided by the radius of the largest inscribing circle. This definition is the most widely accepted in the sedimentology community (Barrett, 1980; Blott and Pye, 2008), however, a number of researchers have proposed usage of roundness of the sharpest corner instead of the average roundness of the corners (Cailleux, 1947; Dobkins and Folk, 1970; Kuenen, 1956; Wentworth, 1919).

Wadell’s measure of roundness is tedious and time consuming to manually measure. As a result, visual classification charts were prepared consisting of categories of roundness (Krumbein, 1941; Powers, 1953). This qualitative measurement of roundness is fast but comes with its own set of drawbacks. The visual comparison

method suffers from the operator bias and the results produced are thus irreproducible and difficult to compare (Blatt, 1992; Blatt et al., 1972).

### 1.1.2 Recent developments

With the advancement of computational power in recent time, image analysis tools are increasingly used for shape characterisation (Ben et al., 2017; Budiansky et al., 2016; Callahan et al., 2013; Cepuritis et al., 2017; Cepuritis et al., 2016; Garboczi and Bullard, 2004; Heilbronner and Barrett, 2014; Lieberman et al., 2015). This also led to the introduction of sophisticated mathematical tools, e.g. Fourier analysis (Dowdeswell, 1982; Schwarcz and Shane, 1969; Suzuki et al., 2015; Thomas et al., 1995), for measurement of particle shape. Use of image analysis tools is widespread in some scientific domains, however, this is less evident in sedimentology.

A probable reason for continued usage of qualitative grain shape analysis by sedimentologists (e.g., Dadd and Foley (2016); Kleesment (2009)) may be the lack of a standardised methodology. Most of the currently available image analysis tools for shape measurement are applicable only to loose particles (Charpentier et al., 2013; Iwata and Ukai, 2002; Schneider et al., 2012). Currently available algorithms for automatic grain boundary segregation of thin section microphotographs are not yet adequate for producing high quality grain boundary information of the type required for sophisticated shape measurement (Gorsevski et al., 2012; Lu et al., 2009; Mingireanov Filho et al., 2013; Roy Choudhury et al., 2006).

Many shape parameters proposed by various researchers are either conceptual (Takashimizu and Iiyoshi, 2016) or are presented in standalone software (Charpentier et al., 2013). The most widely used open source software for image analysis, ImageJ, was developed primarily for use by Biologists (Schneider et al., 2012). Hence, the *shape descriptors* present are basic geometrical shape measures related to overall macro feature of the particle shape rather than detailed characterisation of particle outline as required for roundness measurement.

Mathematically sophisticated shape measurement methods like the Fourier descriptor method suffers from the shortcoming that their result (sometimes of the order of 100 numerical descriptors for a single grain) can be difficult to relate to the physical

attributes of the particle (Bowman et al., 2001; Charpentier et al., 2013; Suzuki et al., 2015; Thomas et al., 1995). Another drawback of the current shape parameters is that they are poor at discriminating between grains which are quite visually distinct (Tafesse et al., 2013). Recent studies have recommended the development of methods for grain corner identification and sharpness measurement (Tafesse et al., 2013), particularly of the sharpest corner (Roussillon et al., 2009). Use of multiple shape parameters for grain characterisation has also been suggested (Blott and Pye, 2008).

### 1.1.3 Application of grain shape

Siliciclastic rock types vary according to the texture. Sedimentary texture comprises the size, shape and fabric of grains in a rock. An important example of two different types of siliciclastic rocks differentiated based on their grain shape is a conglomerate (with rounded clasts) and a breccia (angular clasts). The term "*textural maturity*", proposed by Folk (1951), comprises the degree of sorting, shape of grains and amount of clay content in a rock or sediment sample. A higher degree of textural maturity refers to a highly sorted sample with well rounded grains encompassing very low clay content. It is postulated that the higher the modifying energy expended during the transportation and depositional phase, the higher the textural maturity of sample. In the context of this study, the term "*textural maturity*" refers to the roundness and smoothness of the grain boundary due to the abrasive processes they encounter during transport and depositional phase. In a recent study, shape analysis was applied with limited success to distinguish sedimentary facies based on their textural maturity (Campaña et al., 2016).

The use of grain shape as a tool to discriminate between different sedimentary environments has been a matter of debate (Boggs, 2009; Tucker, 2001; Reineck and Singh, 1975). With image analysis and improved computational tools available, the classical sedimentology problem relating to the validity of using grain shape to classify depositional environment is ripe for investigation. However, there is a paucity of studies addressing this question. One recent study (Suzuki et al., 2015) used an elliptical Fourier transform along with principal component analysis to discriminate sedimentary environments; however, only 15 grains per sample were used. In another study (Eamer et al., 2017), utilising aspect ratio, roundness, circularity and solidity,

samples from aeolian and littoral environment were subjected to discrimination based on their shape.

#### 1.1.4 Aims and objectives

The main objective of this work is to standardise the methodology for quantitative grain shape analysis for sedimentologists which may be of use to researchers from other fields. The first obvious step in this direction is to review and assess the different shape measurement concepts and to suggest improvements if required. The next step is to develop a software tool kit that can be used for shape analysis. This can be applied to thin section and loose sediment data and outputs a suite of shape parameters. The shape analysis toolbox needs to be tested on natural grains and a methodology needs to be established for grain shape data analysis. It is also important to note that the validity of grain shape analysis needs to be assessed for its potential use in sedimentology. A new shape quantification method is necessitated for quantitatively characterising grains such that the results can be better visually correlated. In this regard, the aims of this work is presented below in order of the thesis chapters.

A comprehensive image analysis toolbox for grain shape and size analysis, primarily focused on sedimentological application, is presented in **Chapter 2**. This chapter seeks to:

- 1) review and select a suite of relevant shape parameters currently used for grain shape measurement
- 2) suggest improvements, if required, to available shape parameters
- 3) present a software package along with methodology for grain shape measurement that can be used for loose sediment as well as thin section image data

Next, in **Chapter 3**, a total of 20 loose sediment samples from four depositional environments (glacial, aeolian, fluvial and beach) are analysed using the newly implemented image analysis toolbox. This chapter aims to:

- 4) identify which of the many shape parameters are useful in the textural characterisation of sediments
- 5) determine the potential of ranking samples in order of their textural maturity based on the grain shape dataset

- 6) empirically explore the validity of using population level measurements to discriminate between different environments

Finally, a new shape quantification methodology, addressing the shortcomings of currently used shape parameters, is proposed in **Chapter 4**. The aim of this chapter is to:

- 7) propose a methodology to identify the corners of a particle and measure their sharpness
- 8) present a suite of new shape parameters using this methodology (from Aim 7) that can collectively represent a grain boundary in visually meaningful way.
- 9) assess the shape quantification methodology proposed (Aim 7 and 8) here by application to a natural dataset.
- 10) demonstrate the relationship between the proposed parameters and the visual perception of grain shape.

## 1.2 Part 2 Basin subsidence modelling

### 1.2.1 Basic concepts

The work described in this section deals with the processes involved in sedimentary basin formation by subsidence. A brief description of important related concepts are first reviewed. The Earth's interior is divided into crust, mantle and core. The crust and the upper mantle constitute the lithosphere. There is a density contrast within the lithosphere marking the Moho boundary which differentiates between the crust and the mantle. Underneath the lithosphere lies the asthenosphere which is the lower part of the mantle. Lithosphere represents the thermal boundary layer restricted to heat transfer by conduction. The lithospheric base is defined by rheological boundary between lithosphere and convecting mantle (Fischer et al., 2010). The lithosphere is sometimes modelled as a body floating on a fluid asthenospheric mantle, which is valid over geological time scales. The dynamics of lithosphere and crustal thicknesses are governed by the principle of isostasy.

The term Isostasy is derived from the Greek words "*iso*" and "*stasis*" meaning "equal standing". Isostasy is the state of gravitational equilibrium between the earth's

lithosphere and asthenosphere such that the tectonic plates "float" at an elevation which depends on their thickness and density. There are two main models of isostasy: the Airy model and the Pratt model. Airy isostasy assumes that there is no lateral variation in density of crust and different topographic heights are accommodated due to their depth. On the other hand, Pratt's isostasy assumes equal crustal depth and the variation in topographic height may be explained by the variation of crustal density. There are specific examples where both the models are valid (Watts, 2001). Airy isostasy accommodates variation in lateral density and can be more generally applied and it is incorporated into the types of 1D subsidence models considered here.

### 1.2.2 McKenzie model

McKenzie (1978) provided the first physical concept for the development and evolution of a sedimentary basin due to stretching of lithosphere. The McKenzie model explains the formation of an extensional basin by subsidence due to stretching, thinning and heating up of lithosphere followed by its gradual cooling. Since the original paper describing the model is very brief, a description of the McKenzie model is provided here. Further details on the model can be found in basin analysis textbooks (for e.g., Wangen (2010)). According to this model, basin development undergoes two phases: 1) Uniform instantaneous stretching of the lithosphere by pure shear 2) thermal cooling of the thinned lithosphere.

#### 1.2.2.1 Instantaneous stretching

The lithosphere is assumed to be stretched and thinned by a stretching factor,  $\beta$ . Figure 1.1 depicts the original and stretched state of the lithosphere along with their respective thermal profile. The stretching of lithosphere is assumed to be instantaneous. The thinning of lithosphere results in passive upwelling of the asthenosphere. As a result of thinning of the lithosphere and upwelling of the asthenosphere, the thermal gradient of the stretched lithosphere rises from  $T_a/a$  to  $\beta \cdot T_a/a$  (see Fig. 1.1). It is assumed that the thermal dependence of crustal and mantle density may be approximated to first order as follows:



$$\rho_c(T) = \rho_{c,0}(1 - \alpha(T - T_0)) \quad \rho_m(T) = \rho_{m,0}(1 - \alpha(T - T_0)) \quad Eq. 1.1$$

where  $\alpha$  is the thermal expansibility constant assumed to be same for both crust and mantle.  $\rho_{c,0}$  and  $\rho_{m,0}$  are density at 0°C for crust and mantle respectively. The temperature profile as a function of depth in the undisturbed state (Eq. 1.2) and after stretching (Eq. 1.3) are given by:

$$T_U(z) = T_a \frac{z}{a} \quad Eq. 1.2$$

$$T_I(z, t) = \begin{cases} T_a \beta \frac{z}{a}, & 0 \leq z \leq \frac{a}{\beta} \\ T_a, & \frac{a}{\beta} < z \leq a \end{cases} \quad Eq. 1.3$$

To maintain isostasy at the depth  $a$ , the pressure before and after lithospheric stretching are equated:

$$\int_0^c \rho_c(T_U(z)) dz + \int_c^a \rho_m(T_U(z)) dz = \int_0^{c/\beta} \rho_c(T_I(z)) dz + \int_{c/\beta}^{a/\beta} \rho_m(T_I(z)) dz + \left(a - \frac{a}{\beta} - s_I\right) \rho_m(T_a) + s_I \rho_s \quad Eq. 1.4$$

**1**
**2**

**3**
**4**
**5**

The pressure at any depth calculated as  $\rho(\text{density}) * g(\text{gravitational const.}) * z(\text{depth})$ . The non-zero term  $g$  is common throughout right-hand and left-hand side of the Eq 1.4 and thus cancels out of the equation. The left hand-side of the Eq 1.4 represents the pressure at the depth  $a$  before initial stretching and the right hand-side represents the pressure at depth  $a$  after stretching. The numbers 1 to 4 label the terms in Eq. 1.4 for clarity in Figure 1.1. The sedimentary cover ( $s_I$ ) is assumed to be too thin to affect temperature profile  $T_I(z)$ . It is assumed that sediments will be immediately accommodated in the space generated through the initial instantaneous subsidence ( $s_I$ ) due to stretching. The density of the deposited sediments is assumed to be constant ( $\rho_s$ ). Using the thermal dependency of crustal and mantle density (Eq 1.1), the temperature gradient from the Eq 1.2 and Eq 1.3 are used. Thus, solving Eq 1.4 for  $s_I$  gives:

$$s_I = a \left(1 - \frac{1}{\beta}\right) \frac{(\rho_{m,0} - \rho_{c,0}) \left(\frac{c}{a}\right) \left(1 - \frac{1}{2} \alpha T_a \frac{c}{a}\right) - \frac{1}{2} \rho_{m,0} \alpha T_a}{\rho_{m,0} \left(1 - \frac{1}{2} \alpha T_a\right) - \rho_s} \quad \text{Eq. 1.5}$$

The term  $s_I$  denotes the subsidence due to uniform and instantaneous stretching. The next phase deals with the subsidence due to gradual thermal relaxation of the thinned and hot lithosphere over relatively longer period of time.

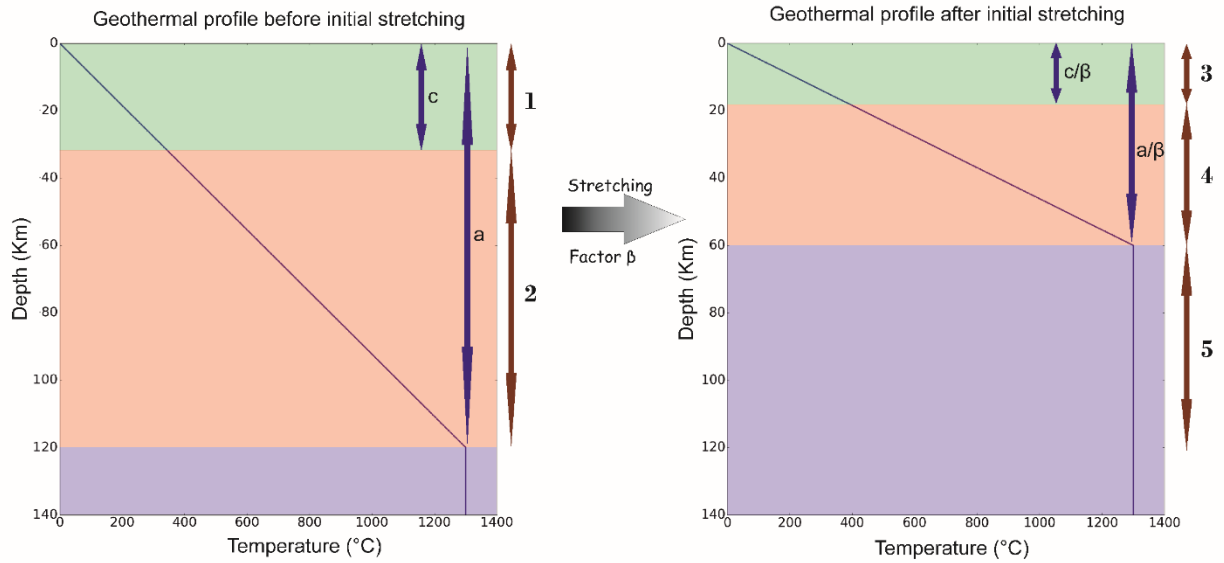


Figure 1.1: Uniform stretching of a basin. Left panel shows the lithospheric configuration at an unstretched state before stretching. Right panel shows the thinned lithosphere and upwelled asthenosphere. The thermal gradient is steepened as a result of lithospheric thinning. The thickness of original crust and lithosphere is assumed to be 36 Km and 120 Km respectively. Stretching factor  $\beta$  is taken as 2. The colour green, orange and violet represents crust, lithospheric mantle and asthenosphere respectively.

#### 1.2.2.2 Thermal relaxation

Due to stretching of lithosphere, the asthenosphere of temperature  $T_a$  rises up effectively heating up the thinned lithosphere. This hotter lithosphere gradually cools down to its original state by conductive cooling. Since the density of crust and mantle is temperature dependent (Eq 1.1), the thermal relaxation causes an increase in density resulting in ongoing gradual subsidence. This is termed thermal subsidence. The following equation governs thermal cooling by conduction:

$$\frac{\partial T}{\partial t} - \kappa \frac{\partial^2 T}{\partial z^2} = 0 \quad \text{Eq. 1.6}$$

where  $\kappa$  is the coefficient of thermal cooling and is assumed to be identical for crust and mantle. Figure 1.1 shows the initial thermal gradient at the initiation of cooling phase and the final thermal gradient to be achieved at time  $t \rightarrow \infty$ . The boundary conditions for Eq 1.6 are:

$$T(0, t) = 0 \quad T(a, t) = T_a \quad \text{Eq. 1.7}$$

The Eq 1.6 along with the boundary condition Eq 1.7 can be solved in terms of Fourier coefficients by separation of variables. The temperature solution is given by:

$$\frac{T}{T_a} = 1 - \frac{z}{a} + \frac{2}{\pi} \sum_{n=1}^{\infty} \frac{(-1)^{n+1}}{n} \left[ \frac{\beta}{n\pi} \sin \frac{n\pi}{\beta} \right] * e^{\left(\frac{-n^2 t}{\tau}\right)} \sin \frac{n\pi z}{a} \quad \text{Eq 1.8}$$

where  $\tau = \frac{a^2}{\pi^2 \kappa}$

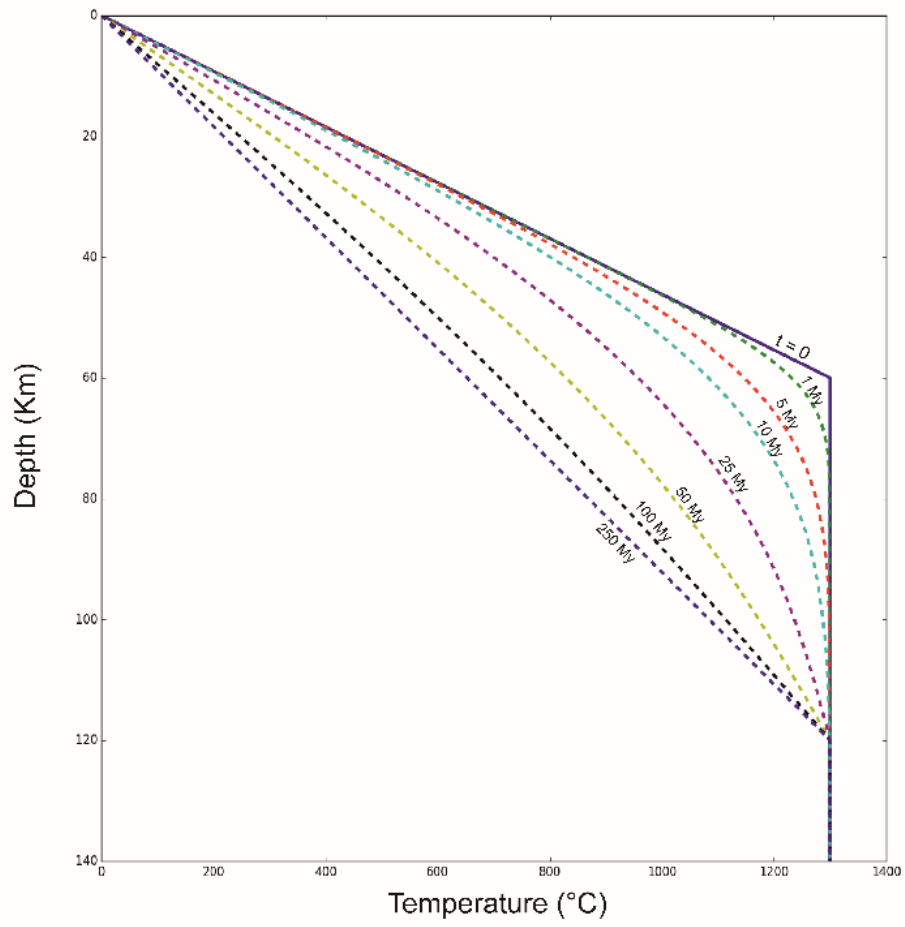


Figure 1.2: Thermal transient representing solutions of Eq. 1.8 at different time 0, 1 My, 5 My, 10 My, 20 My, 50 My, 100 My and 250 My after stretching.

The thermal transients given by Eq. 1.8 is plotted in Figure 1.2. Thermal subsidence governed by isostasy can be calculated by the following equation:

$$\begin{aligned}
 \int_0^a \rho_m(T(z, t)) dz + \rho_s s_T(t) = & \\
 \mathbf{1} \qquad \qquad \mathbf{2} & \\
 = \int_0^a \rho_m(T_I(z)) dz + \rho_m(T_a) s_T(t) & \qquad \text{Eq. 1.9} \\
 \mathbf{3} \qquad \qquad \mathbf{4} &
 \end{aligned}$$

where  $s_T(t)$  is the thermal subsidence at any time  $t$ . The right hand-side of the Eq. 1.9 represents the pressure in asthenosphere at depth  $a + s_T(t)$  at the start of thermal relaxation following instantaneous stretching. On the left hand-side, the terms in Eq. 1.9 represents the pressure at the depth  $a + s_T(t)$  at any time  $t$  during thermal relaxation. The integral terms of Eq. 1.9 are shown in Figure 1.3 for clarity. The sedimentary basin is assumed to be thin in order to neglect its effect on temperature solution in Eq. 1.8. The crust is assumed to be thin compared to the lithospheric thickness, thus taking density  $\rho_m$  for the overall lithospheric density on both the side of Eq. 1.9. The solution of Eq. 1.9, in terms of thermal subsidence is:

$$s_T(t) = a \frac{4\beta\alpha T_a \rho_{m,0}}{(\rho_{m,0} - \rho_s)} \sum_{m=0}^{\infty} \frac{\sin((2m+1)\pi/\beta)}{((2m+1)\pi)^3} \left(1 - e^{-((2m+1)\pi)^2 t/t_0}\right) \quad \text{Eq 1.10}$$

where  $t_0 = a^2/\kappa$

The overall subsidence in a basin due to lithospheric thinning is thus sum of initial subsidence and thermal subsidence.

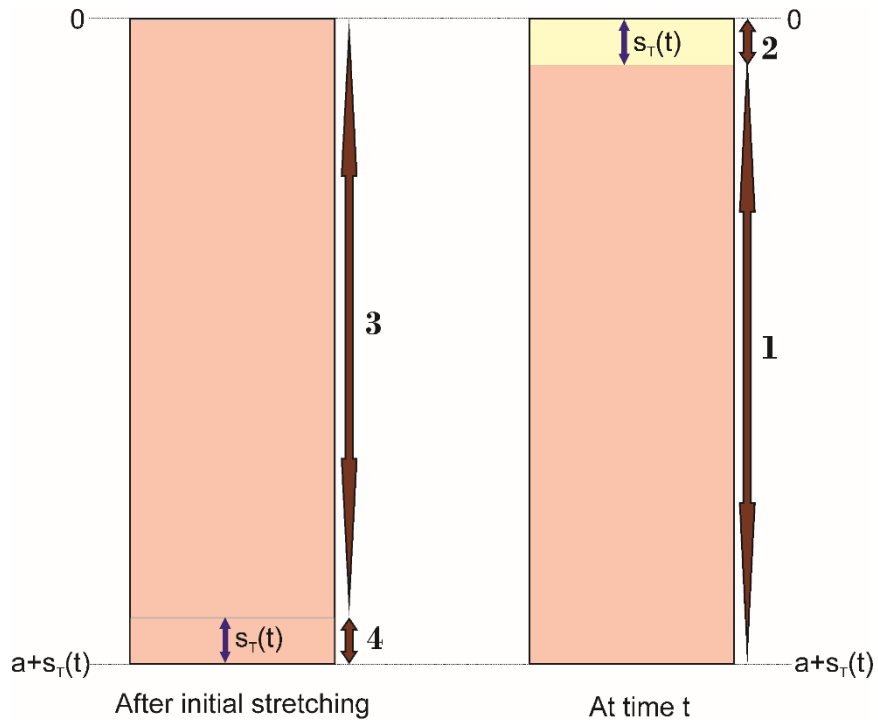


Figure 1.3: The lithospheric configuration after initial stretching and at a time  $t$  is represented by left and right panel respectively. The integral terms of Eq. 1.9 are represented by numbers 1 to 4 on the figure for clarity.

### 1.2.3 Modification to the McKenzie model

A number of variations to the McKenzie model have been suggested to relax some assumptions of the model (Allen and Allen, 2013). Some of the proposed modifications consider: a finite time stretching phase (Jarvis and McKenzie, 1980); non-uniform stretching (Rowley and Sahagian, 1986; Royden and Keen, 1980); simple shear (Wernicke, 1981; Wernicke, 1985) or a combination of pure and simple shear (Kusznir et al., 1991) as the type of stretching; the effect of magmatic activity (White and McKenzie, 1989); radiogenic heat flow (Hantschel and Kauerauf, 2009); lithospheric flexure (Watts et al., 1982); mineral phase transition (Kaus et al., 2005); blanketing effect of the sediments (Wangen, 1995); and depth of lithospheric necking along with rift shoulder erosion (Kooi et al., 1992; van Balen et al., 1995).

#### 1.2.4 Aims and objectives

Basin subsidence models are reliant on physical parameters such as crustal and lithospheric depth prior to extension, density of rocks and sediments, stretching factor, thermal diffusivity and expansibility constants, etc. Thickness of unstretched crust is usually estimated at basin margins using deep seismic and gravity surveys. However, in case of lithospheric thickness, most models assume that the thickness of the original lithospheric column is 120 or 125 Km which may not always be the case (Fischer et al., 2010). Stretching factor is often estimated by comparing a backstripped subsidence profile with forward subsidence models (Allen and Allen, 2013; Steckler and Watts, 1978). However, these models strongly depend on the values of the physical parameters chosen.

The objective of this study is to present a curve fitting method which can compare basin subsidence history from reverse modelling methods e.g. backstripping with the forward subsidence models. This allows model parameters such as stretching factor, original crustal and lithospheric depth to be constrained and estimated. In this regard, we aim to:

- 1) present a 1-Dimensional numerical model which takes into consideration the effect of sediment cover.
- 2) propose a curve fitting method to estimate basin subsidence parameters from a known subsidence history of a basin.

This work is presented in **Chapter 5** of the thesis.

### 1.3 References

**Allen, P.A. and Allen, J.R.** (2013) *Basin analysis: Principles and application to petroleum play assessment*. John Wiley & Sons, Malaysia, 619 pp.

**Barrett, P.J.** (1980) The shape of rock particles, a critical review. *Sedimentology*, **27**, 291-303.

**Ben, B., Tresa, P. and Linda, P.** (2017) Segmentation-free image processing and analysis of precipitate shapes in 2D and 3D. *Modelling and Simulation in Materials Science and Engineering*, **25**, 045009.



- Blatt, H.** (1992) *Sedimentary Petrology*. W. H. Freeman and Company, New York, 514 pp.
- Blatt, H., Middleton, G.V. and Murray, R.C.** (1972) *Origin of sedimentary rocks*. Prentice-Hall Inc., New Jersey, 634 pp.
- Blott, S.J. and Pye, K.** (2008) Particle shape: a review and new methods of characterization and classification. *Sedimentology*, **55**, 31-63.
- Boggs, S.** (2009) *Petrology of sedimentary rocks*. Cambridge University Press, Cambridge, 612 pp.
- Bowman, E.T., Soga, K. and Drummond, W.** (2001) Particle shape characterisation using Fourier descriptor analysis. *Géotechnique*, **51**, 545-554.
- Budiansky, N., Dennies, D.P., Forman, J., Wong, D. and Tucker, J.** (2016) Computed X-ray Tomography of Powder Metallurgy Product for Rapid, Quantitative Size and Shape Distribution Analysis. *Microscopy and Microanalysis*, **22**, 1756-1757.
- Cailleux, A.** (1947) L'indice d'emousse: definition et premiere application. *CRS Soc. géol.*, 250-252.
- Callahan, P.G., Simmons, J.P. and Graef, M.D.** (2013) A quantitative description of the morphological aspects of materials structures suitable for quantitative comparisons of 3D microstructures. *Modelling and Simulation in Materials Science and Engineering*, **21**, 015003.
- Campaña, I., Benito-Calvo, A., Pérez-González, A., Bermúdez de Castro, J.M. and Carbonell, E.** (2016) Assessing automated image analysis of sand grain shape to identify sedimentary facies, Gran Dolina archaeological site (Burgos, Spain). *Sedimentary Geology*, **346**, 72-83.
- Cepuritis, R., Garboczi, E.J., Jacobsen, S. and Snyder, K.A.** (2017) Comparison of 2-D and 3-D shape analysis of concrete aggregate fines from VSI crushing. *Powder Technology*, **309**, 110-125.
- Cepuritis, R., Jacobsen, S., Pedersen, B. and Mørtzell, E.** (2016) Crushed sand in concrete – Effect of particle shape in different fractions and filler properties on rheology. *Cement and Concrete Composites*, **71**, 26-41.
- Charpentier, I., Sarocchi, D. and Rodriguez Sedano, L.A.** (2013) Particle shape analysis of volcanic clast samples with the Matlab tool MORPHEO. *Computers & Geosciences*, **51**, 172-181.

- Dadd, K. and Foley, K.** (2016) A shape and compositional analysis of ice-rafted debris in cores from IODP Expedition 323 in the Bering Sea. *Deep Sea Research Part II: Topical Studies in Oceanography*, **125**, 191-201.
- Dobkins, J.E. and Folk, R.L.** (1970) Shape development on Tahiti-nui. *Journal of Sedimentary Research*, **40**, 1167-1203.
- Dowdeswell, J.A.** (1982) Scanning electron micrographs of quartz sand grains from cold environments examined using Fourier shape analysis. *Journal of Sedimentary Research*, **52**, 1315-1323.
- Eamer, J.B.R., Shugar, D.H., Walker, I.J., Lian, O.B. and Neudorf, C.M.** (2017) Distinguishing Depositional Setting For Sandy Deposits In Coastal Landscapes Using Grain Shape. *Journal of Sedimentary Research*, **87**, 1-11.
- Fischer, K.M., Ford, H.A., Abt, D.L. and Rychert, C.A.** (2010) The Lithosphere-Asthenosphere Boundary. *Annual Review of Earth and Planetary Sciences*, **38**, 551-575.
- Folk, R.L.** (1951) Stages of textural maturity in sedimentary rocks. *Journal of Sedimentary Research*, **21**, 127-130.
- Friedman, G.M. and Sanders, J.E.** (1978) *Principles of Sedimentology*. John Wiley & Sons, New York, 792 pp.
- Garboczi, E.J. and Bullard, J.W.** (2004) Shape analysis of a reference cement. *Cement and Concrete Research*, **34**, 1933-1937.
- Gorsevski, P.V., Onasch, C.M., Farver, J.R. and Ye, X.** (2012) Detecting grain boundaries in deformed rocks using a cellular automata approach. *Computers & Geosciences*, **42**, 136-142.
- Hantschel, T. and Kauerauf, A.I.** (2009) *Fundamentals of basin and petroleum systems modeling*. Springer Berlin, 475 pp.
- Heilbronner, R. and Barrett, S.** (2014) *Image analysis in earth sciences: microstructures and textures of earth materials*. Springer 520 pp.
- Iwata, H. and Ukai, Y.** (2002) SHAPE: A Computer Program Package for Quantitative Evaluation of Biological Shapes Based on Elliptic Fourier Descriptors. *Journal of Heredity*, **93**, 384-385.
- Jarvis, G.T. and McKenzie, D.P.** (1980) Sedimentary basin formation with finite extension rates. *Earth and Planetary Science Letters*, **48**, 42-52.

- Kaus, B.J.P., Connolly, J.A.D., Podladchikov, Y.Y. and Schmalholz, S.M.** (2005) Effect of mineral phase transitions on sedimentary basin subsidence and uplift. *Earth and Planetary Science Letters*, **233**, 213-228.
- Kleesment, A.** (2009) Roundness and surface features of quartz grains in Middle Devonian deposits of the East Baltic and their palaeogeographical implications. *Estonian Journal of Earth Sciences*, **58**, 71-84.
- Kooi, H., Cloetingh, S. and Burrus, J.** (1992) Lithospheric necking and regional isostasy at extensional basins 1. Subsidence and gravity modeling with an application to the Gulf of Lions Margin (SE France). *Journal of Geophysical Research: Solid Earth*, **97**, 17553-17571.
- Krumbein, W.C.** (1941) Measurement and geological significance of shape and roundness of sedimentary particles. *Journal of Sedimentary Research*, **11**, 64-72.
- Krumbein, W.C. and Pettijohn, F.J.** (1938) Manual of sedimentary petrography.
- Kuenen, P.H.** (1956) Experimental abrasion of pebbles: 2. Rolling by current. *The Journal of Geology*, **64**, 336-368.
- Kusznir, N.J., Marsden, G. and Egan, S.S.** (1991) A flexural-cantilever simple-shear/pure-shear model of continental lithosphere extension: applications to the Jeanne d'Arc Basin, Grand Banks and Viking Graben, North Sea. *Geological Society, London, Special Publications*, **56**, 41-60.
- Lieberman, E.J., Rollett, A.D., Lebensohn, R.A. and Kober, E.M.** (2015) Calculation of grain boundary normals directly from 3D microstructure images. *Modelling and Simulation in Materials Science and Engineering*, **23**, 035005.
- Lu, B., Cui, M., liu, Q. and Wang, Y.** (2009) Automated grain boundary detection using the level set method. *Computers & Geosciences*, **35**, 267-275.
- McKenzie, D.** (1978) Some remarks on the development of sedimentary basins. *Earth and Planetary Science Letters*, **40**, 25-32.
- Mingireanov Filho, I., Vallin Spina, T., Xavier Falcão, A. and Campana Vidal, A.** (2013) Segmentation of sandstone thin section images with separation of touching grains using optimum path forest operators. *Computers & Geosciences*, **57**, 146-157.
- Powers, M.C.** (1953) A new roundness scale for sedimentary particles. *Journal of Sedimentary Research*, **23**, 117-119.
- Reineck, H. and Singh, I.** (1975) *Depositional Sedimentary Environments*. Springer—Verlag, New York, 439 pp.

- Riley, N.A.** (1941) Projection sphericity. *Journal of Sedimentary Research*, **11**, 94-97.
- Roussillon, T., Piégay, H., Sivignon, I., Tougne, L. and Lavigne, F.** (2009) Automatic computation of pebble roundness using digital imagery and discrete geometry. *Computers & Geosciences*, **35**, 1992-2000.
- Rowley, D.B. and Sahagian, D.** (1986) Depth-dependent stretching: A different approach. *Geology*, **14**, 32-35.
- Roy Choudhury, K., Meere, P.A. and Mulchrone, K.F.** (2006) Automated grain boundary detection by CASRG. *Journal of Structural Geology*, **28**, 363-375.
- Royden, L. and Keen, C.E.** (1980) Rifting process and thermal evolution of the continental margin of Eastern Canada determined from subsidence curves. *Earth and Planetary Science Letters*, **51**, 343-361.
- Schneider, C.A., Rasband, W.S. and Eliceiri, K.W.** (2012) NIH Image to ImageJ: 25 years of image analysis. *Nature Methods*, **9**, 671.
- Schwarcz, H.P. and Shane, K.C.** (1969) Measurements of particle shape by Fourier analysis. *Sedimentology*, **13**.
- Steckler, M.S. and Watts, A.B.** (1978) Subsidence of the Atlantic-type continental margin off New York. *Earth and Planetary Science Letters*, **41**, 1-13.
- Suzuki, K., Fujiwara, H. and Ohta, T.** (2015) The evaluation of macroscopic and microscopic textures of sand grains using elliptic Fourier and principal component analysis: Implications for the discrimination of sedimentary environments. *Sedimentology*, **62**, 1184-1197.
- Tafesse, S., Robison Fernlund, J.M., Sun, W. and Bergholm, F.** (2013) Evaluation of image analysis methods used for quantification of particle angularity. *Sedimentology*, **60**, 1100-1110.
- Takashimizu, Y. and Iiyoshi, M.** (2016) New parameter of roundness R: circularity corrected by aspect ratio. *Progress in Earth and Planetary Science*, **3**, 2.
- Thomas, M.C., Wiltshire, R.J. and Williams, A.T.** (1995) The use of Fourier descriptors in the classification of particle shape. *Sedimentology*, **42**, 635-645.
- Tucker, M.E.** (2001) *Sedimentary petrology: an introduction to the origin of sedimentary rocks*. . Blackwell Science Ltd, Oxford.
- van Balen, R.T., van der Beek, P.A. and Cloetingh, S.A.P.L.** (1995) The effect of rift shoulder erosion on stratal patterns at passive margins: Implications for sequence stratigraphy. *Earth and Planetary Science Letters*, **134**, 527-544.

- Wadell, H.** (1932) Volume, Shape, and Roundness of Rock Particles. *The Journal of Geology*, **40**, 443-451.
- Wadell, H.** (1933) Sphericity and roundness of rock particles. *The Journal of Geology*, **41**, 310-331.
- Wangen, M.** (1995) The blanketing effect in sedimentary basins. *Basin Research*, **7**, 283-298.
- Wangen, M.** (2010) *Physical principles of sedimentary basin analysis*. Cambridge University Press, Cambridge, 527 pp.
- Watts, A.B.** (2001) *Isostasy and Flexure of the Lithosphere*. Cambridge University Press, Cambridge, 459 pp.
- Watts, A.B., Karner, G.D. and Steckler, M.S.** (1982) Lithospheric flexure and the evolution of sedimentary basins. *Philosophical Transactions of the Royal Society of London. Series A, Mathematical and Physical Sciences*, **305**, 249-281.
- Wentworth, C.K.** (1919) A laboratory and field study of cobble abrasion. *The Journal of Geology*, **27**, 507-521.
- Wernicke, B.** (1981) Low-angle normal faults in the Basin and Range Province: nappe tectonics in an extending orogen. *Nature*, **291**, 645-648.
- Wernicke, B.** (1985) Uniform-sense normal simple shear of the continental lithosphere. *Canadian Journal of Earth Sciences*, **22**, 108-125.
- White, R. and McKenzie, D.** (1989) Magmatism at rift zones: The generation of volcanic continental margins and flood basalts. *Journal of Geophysical Research: Solid Earth*, **94**, 7685-7729.

## **2 Mathematica code for quantitative characterisation of sedimentary grains**

*Mohit Tunwal<sup>1)2)</sup>\*, Kieran F. Mulchrone<sup>2)</sup> and Patrick A. Meere<sup>1)</sup>*

(Current status: ready for submission)

*<sup>1)</sup> School of Biological, Earth and Environmental Sciences, University College Cork, Distillery Fields, North Mall, Cork, Ireland*

*<sup>2)</sup> School of Mathematical Sciences, University College Cork, Western Gateway Building, Western Road, Cork, Ireland*

### **Abstract**

Shape analysis can provide vital information regarding the origin, transport and deposition history of grains. Particle shape measurement has been an active area of research for sedimentologists since the 20th century. With advancement in the field of computation and image analysis, shape analysis can be done in a faster and much more accurate way compared to manual measurements. The results obtained are reproducible as compared to visual qualitative analysis. However, there is a lack of image analysis software tools aimed at the field of sedimentology where the fine details of a particle boundaries are required. A modular suite of code written in the Mathematica environment for the quantitative characterisation of sedimentary grains in 2-dimensions is presented. This image analysis package can be used to analyse consolidated as well as loose sediment samples. A total of 12 parameters are available for shape measurement comprising conventional shape parameters (roundness, angularity, circularity and irregularity), mathematically complex shape parameters (fractal dimension and Fourier descriptors) and common geometrical shape parameters (aspect ratio, convexity, solidity, mod ratio, rectangularity and compactness). Grain size can be extracted and the 2-D size distribution can be transformed to a 3-D size distribution. Example analyses have been carried out on a sandstone and a loose sediment sample. This contribution aims to standardise textural

analysis methodology used by sedimentologists and allow users to quantitatively characterise large set of grains with a fast, cheap and robust methodology.

\*Corresponding author: [mohittunwal@gmail.com](mailto:mohittunwal@gmail.com)

Keywords: grain shape, grain size, image analysis, texture, roundness, shape

## 2.1 Introduction

Shape analysis of sedimentary particles provides vital information regarding its origin, transport and deposition history (Pettijohn, 1957). This area of research has occupied sedimentologists for over a century (Barrett, 1980; Blott and Pye, 2008 and references therein). However, shape analysis studies suffer from two common shortcomings 1) with a plethora of available shape parameters, a standardised methodology is lacking 2) most of these shape parameters are time consuming and tedious to calculate manually. Visual comparison charts were proposed to ease the effort required for shape analysis (Krumbein, 1941; Powers, 1953). However, qualitative comparison methods suffer from user bias and reproducibility issues (Blatt, 1992; Blatt et al., 1972).

In the recent years, with the advancement of computational power and image analysis techniques, shape analysis has been getting a renewed focus (Campaña et al., 2016; Eamer et al., 2017; Lira and Pina, 2009; Sochan et al., 2015; Suzuki et al., 2015). Most of these methods have been primarily applied to loose sediments where it is easier to define grain boundaries automatically. On the other hand, the currently available automated grain boundary segmentation algorithms (Gorsevski et al., 2012; Lu et al., 2009; Mingireanov Filho et al., 2013; Roy Choudhury et al., 2006) do not produce the quality of grain boundary data from thin section microphotographs required for shape analysis. A high resolution microphotograph with clear distinction between matrix and clasts is usually required (Roduit, 2007) for such automated grain boundary segmentation but this is the exception rather than the rule.

Another shortcoming in presently available image analysis tools is that they do not offer a wide range of shape parameters for a comprehensive shape analysis study. One of the most widely used image analysis software platforms, ImageJ, was developed primarily for use by biologists (Schneider et al., 2012). Hence, the *shape descriptors* present are basic geometrical shape measures related to overall macro features of the particle shape rather than a detailed characterisation of the particle outline as required for example for roundness measurement. Furthermore, recently proposed shape parameters by various researchers are either conceptual (Takashimizu and Iiyoshi, 2016) or are presented in standalone software (Charpentier et al., 2013).

The objective of this contribution is to present an image analysis software package that offers a wide range of size and shape parameters to quantitatively characterise grains from both loose sediments and rock thin section microphotographs. In this regard, this paper aims to:

- 1) review and select a suite of relevant shape parameters currently used for grain shape measurement
- 2) suggest improvements, if required, to available shape parameters
- 3) present a software package along with methodology for grain shape measurement that can be used for loose sediment as well as thin section image data

In the case of loose sediments, a fully automated approach is presented. On the other hand, manual tracing of grain boundaries is suggested for thin section photomicrographs. The image analysis package is developed on the Mathematica platform which offers a variety of in-built powerful image analysis and computational routines.

The parameters available in the software package are described in the next section followed by a methodology for use. Implementation details and example analyses of both loose and consolidated sediments are provided. The image analysis toolbox presented in this paper aims to establish a standardised methodology for reproducible and comparable quantitative textural analysis of grains.



## 2.2 Parameter for grain characterisation

Measurements in this paper are focused on a 2-dimensional projection of the grain boundary along its intermediate and long axis. Roundness, circularity, irregularity, angularity, fractal dimension and the Fourier method are described along with other geometrical shape and size parameters.

### 2.2.1 Grain size

Measurement techniques vary depending on sample grain size and level of consolidation. Larger grains such as boulders, cobbles and pebbles are usually manually measured. Unconsolidated sediments comprising granules and sand sized grains are analysed using sieving and settling tube analysis. Image analysis can be applied to both unconsolidated sediments and lithified rocks for granule and sand size particle measurement. Clay sized particles in lithified rocks are primarily measured using SEM imagery. In the case of unconsolidated sediments pipette analysis, sedimentation balances, sedigraph, laser diffractory and electro-resistance size analysis can also be employed (Boggs 2009).

In this paper, the size of sand grains is measured using image analysis techniques on a microphotograph. However, the methodology presented here can be extended to images of particles from other size fractions. The size of a grain in 2-D projection can be measured by multiple parameters (see Table 2.1). The software package presented here offers to compute the grain size and outputs all the size parameters summarised in Table 2.1.

Due to slicing of grains in thin section, the measured size of a grain from a thin section microphotograph is usually less than the size measured from the projection on a loose grain (Burger and Skala, 1976). Some authors have recommended using a simple multiplication factor to transform a 2-D grain size distribution to a 3-D size distribution (for example, Harrell and Eriksson (1979); Kong et al. (2005)), however, others have recommended using a size distribution transformation algorithm (Heilbronner and Barrett, 2014; Higgins, 2000; Peterson, 1996). In this paper, one such algorithm, which assumes an initial uniform size distribution, is adopted (Heilbronner and Barrett, 2014).

Size parameter	Formula	Description
$S_c$	$D_c$	Diameter of smallest circumscribing circle over a grain boundary
$S_p$	$P/\pi$	Perimeter of grain boundary divided by $\pi$
$S_d$	$\sqrt{4A/\pi}$	Diameter of equivalent disk area of the grain
$S_a$	$L_{major}$	Long axis of the best fit ellipse
$S_b$	$L_{minor}$	Short axis of the best fit ellipse
$S_m$	$\frac{2 \sum_{i=1}^n (d_i)}{n}$	Twice of the mean distance between centre and grain boundary

*Table 2.1: List of size parameters implemented in the software package.*

## 2.2.2 Grain shape

A large number of parameters have been proposed to quantify grain shape (Barrett, 1980; Blott and Pye, 2008 and references therein). It is difficult to select one parameter out of the many available, that allows for consistent, reliable and accurate distinction between grains of different shapes. As a result, the relative merits of different shape parameters have been extensively reviewed along with the many practical studies making comparisons (Barrett, 1980; Blott and Pye, 2008; Cox and Budhu, 2008; Illenberger, 1991). In light of their applicability to 2-D image data, the following parameters are discussed and implemented here: roundness, circularity, irregularity, angularity, fractal dimension, Fourier descriptors and a number of other simpler parameters such as aspect ratio, rectangularity, convexity, modratio, compactness and solidity.

### 2.2.2.1 Roundness

Radius of curvature was first used to quantify roundness (Wentworth, 1919), prior to which, visual classification was used. Roundness and sphericity were originally

considered to be the same parameter but were later recognised to be independent (Wadell, 1932). The most widely accepted definition of roundness (Wadell, 1932) is that it is the average roundness of the corners of a grain in a 2-D sectional plane. Let  $r$  be the radius of curvature of the boundary and let  $r_{max}$  be the radius of the largest inscribed circle to the grain boundary. Corners are those parts of the grain boundary where  $r < r_{max}$ . Grain roundness is average radius of curvature of the corners  $\sum r_i / n$  divided by the  $r_{max}$ .

$$R = \frac{1}{n r_{max}} \sum_{i=1}^n r_i$$

Although widely accepted, this approach to roundness is labour intensive and time consuming. It led to the introduction of visual comparators where the degree of roundness can be visually estimated on the basis of standard charts. A popular chart was based on pre-determined Wadell (1932) roundness values (Krumbein, 1941) and categorised pebble roundness from 0.1 to 0.9 for ease of use. However, the use of visual comparison charts suffers from subjectivity and leads to poor reproducibility.

Roundness can now be determined in a time efficient and objective manner using computational image analysis techniques. For example, roundness may be determined using the radius of curvature estimated at each pixel of the grain boundary (Roussillon et al., 2009). Here the radius of curvature at each pixel of the grain boundary curve is determined as the radius of that circle circumscribing three points: 1)  $i$ th pixel at which radius of curvature is to be determined, 2)  $(i+n)$ th pixel and 3)  $(i-n)$ th pixel. The value of  $n$  is normalised on the basis of total number of boundary points in the particle (see Fig. 2.1a).

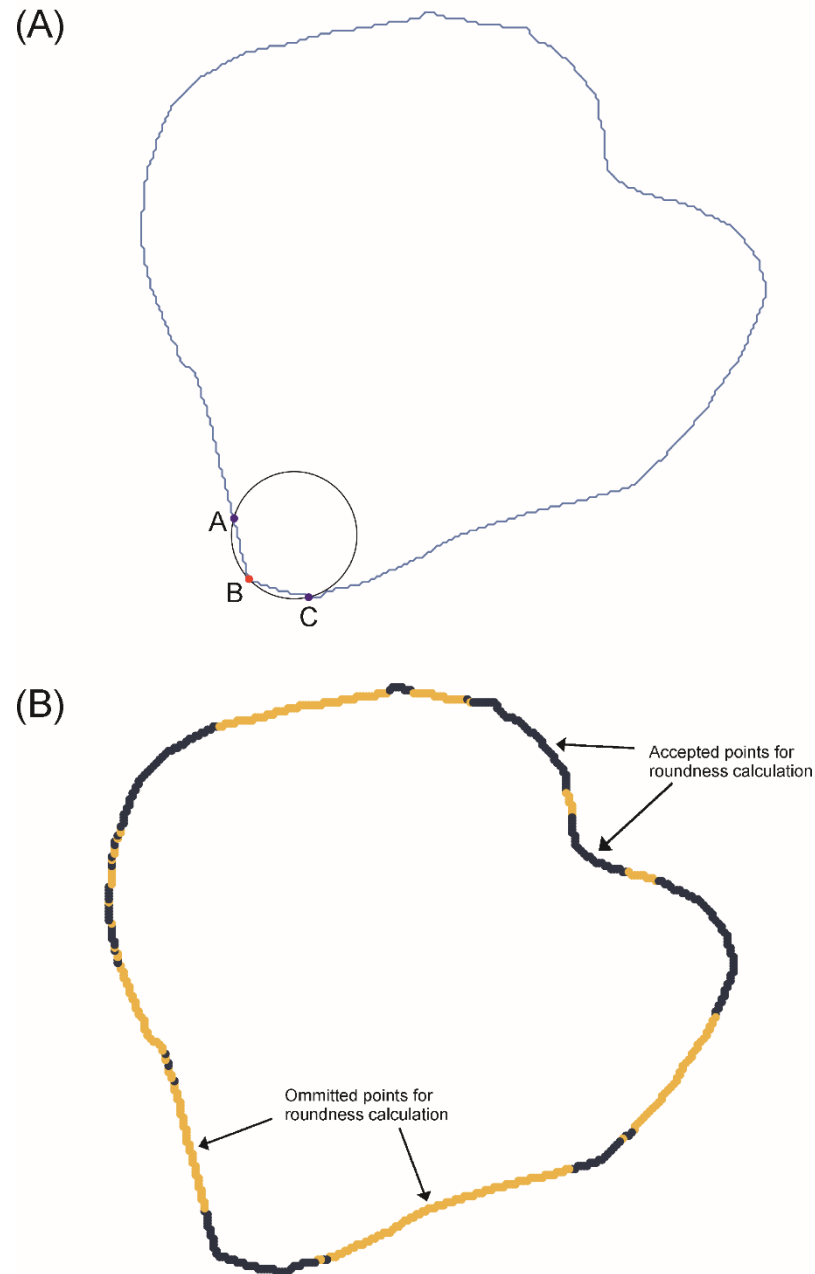


Figure 2.1: Roundness measurement of a grain boundary. (a) Calculation of radius of curvature at the  $i$ th pixel point  $B$  is the radius of circle that passes through the points  $A, B$  and  $C$ . The points  $A$  and  $C$  are the  $(i + n)$ th pixel and  $(i - n)$ th pixel where  $n$  is normalised on the basis total number of boundary points. (b) The grain boundary points with radius of curvature lower than the radius of largest inscribing circle represents the corner region and are thus accepted for roundness calculation.

### 2.2.2.2 Sphericity and Circularity

Sphericity is defined as how closely a grain approximates a sphere. It has been used as a parameter to define the general form of a grain and is sometimes confused with roundness. Sphericity was first proposed to be the ratio of grain volume to that of the circumscribing sphere (Wadell, 1932). However, this definition also encompasses roundness (Barrett, 1980). *Intercept sphericity* was also proposed as a possible measure whereby the grain is compared to an ellipsoid (Krumbein, 1941). It is measured using the major orthogonal axes of the best-fit ellipsoid of a grain and the diameter of the circumscribing sphere. *Working sphericity* was suggested as an improvement where rocks were represented by a more general form of tetrakaidekahedron instead of ellipsoid (Aschenbrenner, 1956). *Maximum projection sphericity* recognises that grain shape is related to its behaviour in a fluid (Sneed and Folk, 1958).

Practical difficulties associated with measuring three orthogonal axes, surface area and volume led to the introduction of *Circularity* as a proxy to sphericity. Circularity is a 2-D measure applied to a planar section through a grain. A measure of circularity was proposed as the ratio of diameter of the equivalent disk area of the grain, to the diameter of the smallest circumscribing circle on the grain boundary (Wadell, 1935). Another measure of circularity, called the inscribed circle sphericity, was suggested as the square root of the ratio of diameter of the largest inscribed circle to the diameter of smallest circumscribing circle (Riley, 1941). It is given by:

$$C = \sqrt{(D_I/D_c)}$$

where  $C$  is the circularity,  $D_I$  is the diameter of largest inscribed circle and  $D_c$  is the diameter of smallest circumscribing circle (see Fig. 2.2). Typical circularity parameters (Cox, 1927; Janoo, 1998; Pentland, 1927; Riley, 1941; Wadell, 1933; Wadell, 1935) were applied to 23 gravel particles in a comparison study (Blott and Pye, 2008). They found that the methods of Wadell (1935) and Riley (1941) provided optimal results. Due to its simplicity and similarity to Wadell (1935), Riley (1941) was considered to be the best parameter and is implemented in this package.

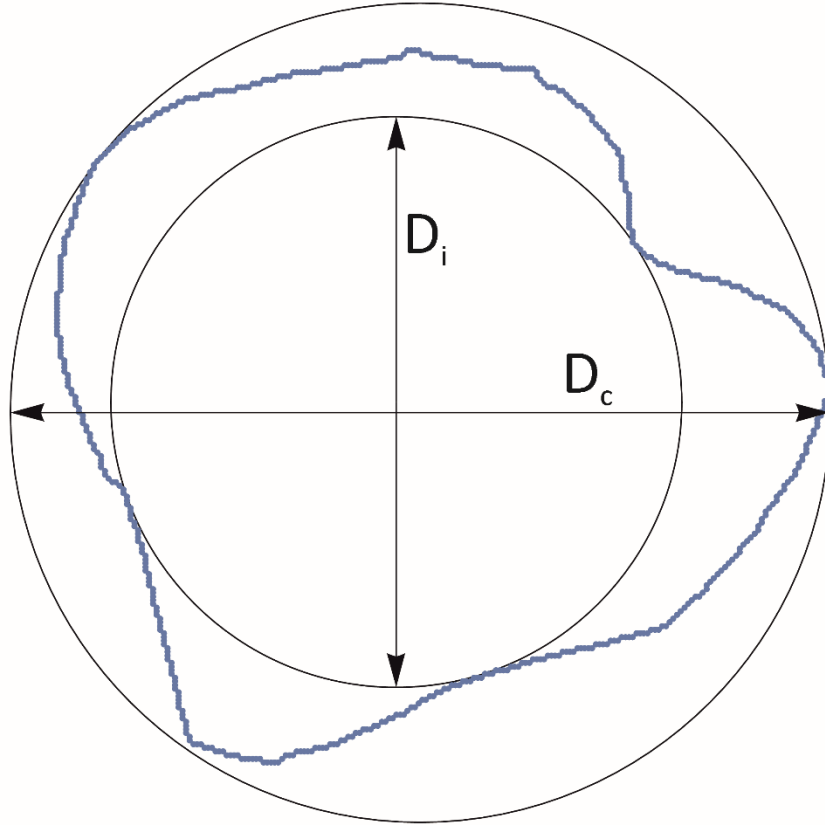


*Figure 2.2: Circularity of grain measured by square root over the ratio of diameter of the largest inscribed circle ( $D_i$ ) divided by the diameter of the smallest circumscribed circle ( $D_c$ ).*

### 2.2.2.3 Irregularity

Irregularity has been recently suggested as a parameter to describe grain shape (Blott and Pye, 2008). It is defined as a way to measure the indentations and projections of a grain with respect to the centre of the largest inscribed circle of the grain. It is calculated as:

$$\text{Irreg} = \sum \frac{y-x}{y}$$

where  $x$  is the furthest point from the edge of the convex hull which spans a concavity and  $y$  is the distance to the convex hull in the same direction from the centre of the

largest inscribed circle. In some cases, projections are missed because this measure picks out only one point within the span of concavity (see Fig. 2.3).

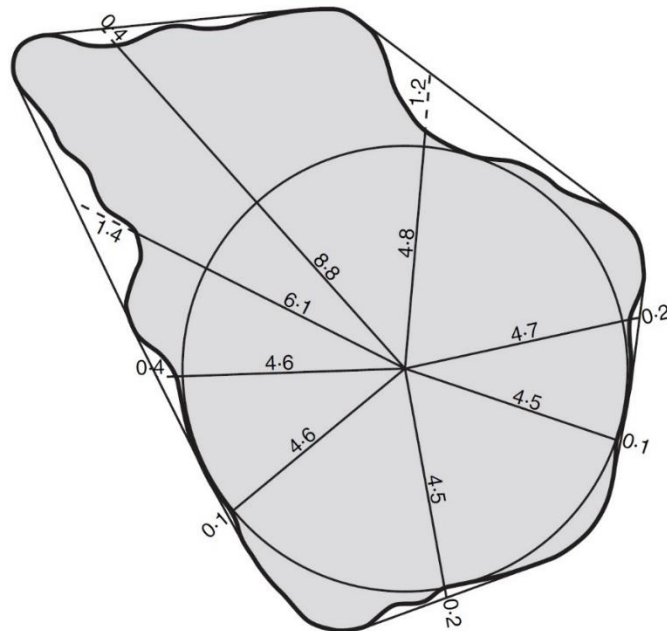


*Figure 2.3 Diagram representing measurement of irregularity parameter after Blott and Pye, (2008).*

An alternative approach is suggested here based on comparison with a regular shape. It is necessary to choose a standard regular shape to compare the irregularity of sedimentary grains. A circle is an obvious choice, however the focus is on irregularity and not circularity, which is already considered. The best-fit ellipse is a more general regular shape, and is thus selected.

The best-fit ellipse of the grain particle is super imposed on the grain boundary. Deviations from the ellipse are the indentations and projections of grain. Irregularity can be quantified in two ways:

- 1) Sum over the grain boundary the difference between the ellipse and the grain boundary along a direction from the common centre.
- 2) The ratio of non-overlapping area between the grain boundary and best-fit ellipse, to the area of ellipse (see Fig. 2.4).

The former approach was used to quantify angularity (Masad et al., 2001). However, this approach cannot deal with the re-entrant angle problem (refer to section 2.2.2.6).

Therefore, in this package the latter approach is adopted because is simple to implement and does not suffer from the re-entrant angle problem. It is given by:

$$I = A_U/A_E$$

Where  $I$  is the irregularity,  $A_U$  is the non-overlapping area and  $A_E$  is the area of ellipse (see Fig. 2.4c).

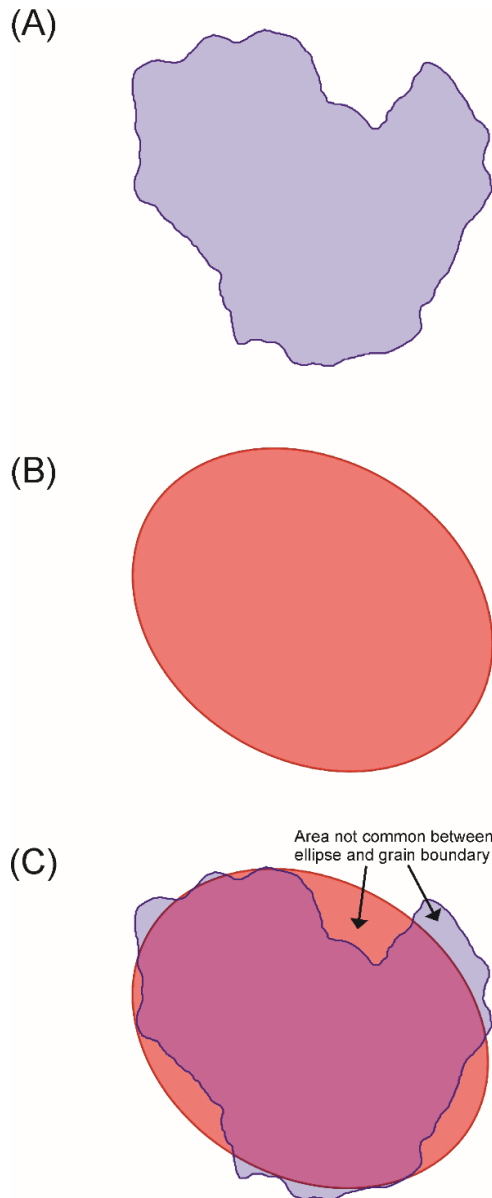


*Figure 2.4 Measurement of grain irregularity. (a) Grain boundary to be analysed. (b) Best fit ellipse for the grain boundary to be analysed. (c) Overlap of best fit ellipse over the grain boundary. Irregularity is measured as a ratio of area not common between ellipse and grain boundary divided by the area of ellipse.*



#### 2.2.2.4 Angularity

Angularity is usually considered the opposite of roundness, however it is formally defined as a shape parameter based on acuteness of angle of corners, number of corners and projection of corners from the centre of grain particle (Lees, 1964). This parameter has been used in civil engineering applications for classification of clast shape in gravels.

A comparison study (Al-Rousan et al., 2007) evaluated angularity parameters based on angularity using Fourier analysis (FRANG), surface erosion dilation (STI), fractal dimension (FRCTL), gradient angularity Index (GRAD), radius angularity index (RAD) and angularity using outline slope (AI) (Chandan et al., 2004; Masad et al., 2000; Masad and Button, 2000; Masad et al., 2001; Rao et al., 2002; Wang et al., 2003). Based on correlation of measured angularity values with visual chart and the ability to distinguish grain types, GRAD and AI were found to perform best. Tafesse et al. (2013) evaluated these two parameters along with angularity factor (AF, Wang et al. (2012)) and smoothing angularity index (SAI, Tafesse et al. 2013) and they found that the GRAD and SAI methods to be most effective. The evaluation was based on the effectiveness of the various methods to differentiate between samples that were already classified based on a visual chart (Tafesse et al., 2013). However, different approaches in the two comparison studies, from image acquisition to computation, may account for the variation between them.

AI and GRAD were tested on basic shapes, and AI was empirically found to perform better than the GRAD method in classifying grains. SAI has much to recommend it, however, it is computationally more intensive for small gains. In this package, a modification to AI (Rao et al., 2002) is implemented. To measure angularity, the boundary of a grain particle is represented by a  $n$  sided polygon. The internal angle at each vertex is computed, which is represented by  $\alpha_1$  to  $\alpha_n$ . The difference between the pair of consecutive angles ( $\alpha_1-\alpha_2$ ,  $\alpha_2-\alpha_3$  to  $\alpha_n-\alpha_1$ ) of the polygon is calculated for all vertices (see Fig. 2.5). The average of the five largest differences of angles is the Angularity.

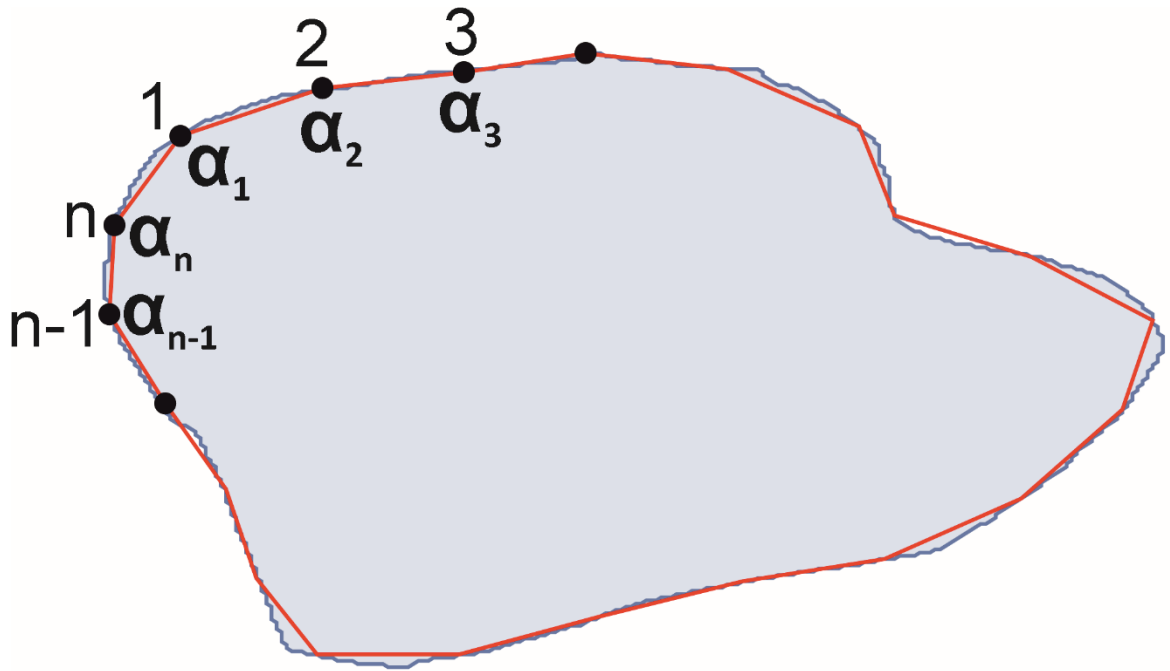


*Figure 2.5: Angularity measurement of a grain by modified Rao et al. (2002). Grain boundary is represented by  $n$  sided polygon. Internal angles  $\alpha_1, \alpha_2, \alpha_3$  till  $\alpha_n$  for the polygon is measured. Differences within the successive internal angles is measured and the five largest differences of internal angles are averaged to calculate angularity.*

#### 2.2.2.5 Fractal dimension

Benoit Mandelbrot is credited with discovering the field of Fractal geometry in mathematics to characterise irregular shapes and quantify their roughness (Mandelbrot, 1982). Fractals are geometric shapes with complex boundaries, which usually possess a degree of self-similarity. They are strongly reminiscent of natural objects such as trees, clouds and mountains. The notion of fractal dimension has been applied to natural objects as a means of quantifying the roughness of a shape. Using fractal dimension as a measure of roughness in granular materials is already established (Hyslip and Vallejo, 1997). Fractal dimension has been measured using divider and box counting methods. Based on testing both of the methods on geometrical shapes, the divider method was found to be more robust in characterising shape and was thus selected here.

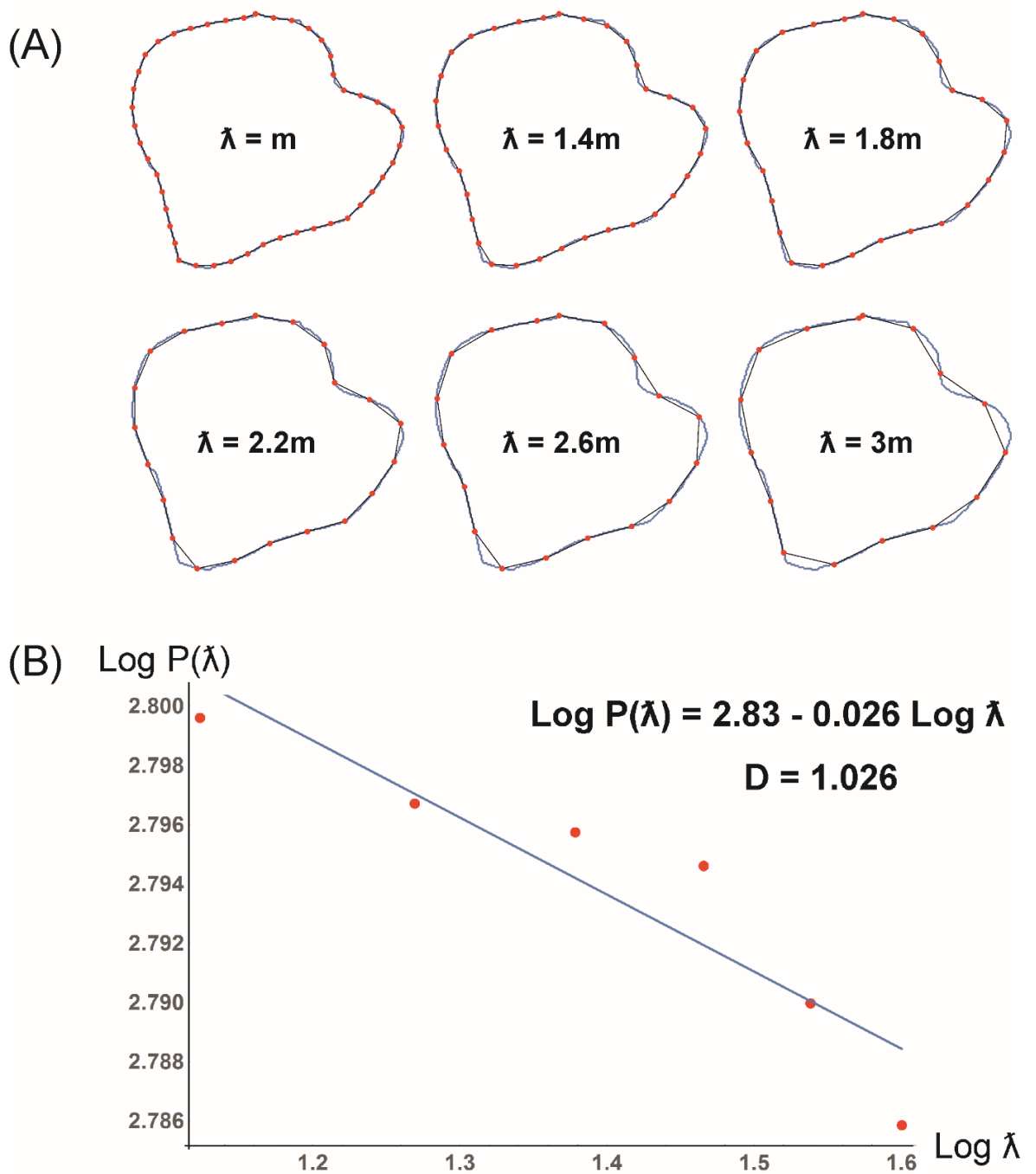


Figure 2.6: Fractal dimension calculation for a grain using the divider method. (a) Grain boundary perimeter  $P(\lambda)$  measured by increasing unit length  $\lambda$ . The value of  $m$  is 13.28 pixel dimension based on the size of the grain. (b)  $\text{Log } P(\lambda)$  versus  $\text{Log } \lambda$  showing the fractal dimension ( $D$ ) calculation.

The divider method essentially measures the length of the boundary using different measuring sticks and uses the relationship between the two to estimate the fractal dimension (see Fig. 2.6a). If the length of the boundary of a shape is measured to be  $P(\lambda)$ , using measure of length  $\lambda$  then

$$P(\lambda) = n\lambda^{1-D}$$

where  $D$  is the fractal dimension and  $n$  is a constant of proportionality, which depends on the actual length of the boundary being analysed. Lower values of  $\lambda$  result in more accurate and increased estimates of boundary length  $P(\lambda)$ . Taking logarithms:

$$\log P(\lambda) = \log n + (1 - D) \log \lambda$$

thus  $D$  may be readily estimated by finding the best fit straight line to a set of data of  $(\log \lambda, \log P(\lambda))$  (see Fig. 2.6b).

#### 2.2.2.6 Fourier method

Ehrlich and Weinberg (1970) introduced Fourier analysis for sediment grains as an accurate way to characterise their shape and roughness. Fourier analysis is based on the fact that any periodic function can be represented by a series of sine and cosine terms, i.e.:

$$R(\theta) = a_0 + \sum_{n=1}^N (a_n \cos n\theta + b_n \sin n\theta)$$

Where  $R(\theta)$  represents the distance from the centre to the boundary of a grain at angle  $\theta$ ,  $N$  is the number of terms in the series,  $a_n$  and  $b_n$  are the Fourier coefficients.

Fourier analysis is applied in shape characterisation by unrolling the particle boundary and treating it as periodic wave function (see Fig. 2.7) and using the centroid of the grain as the origin. The particle boundary can be reconstructed to a high degree of accuracy by using a suitable number of terms.

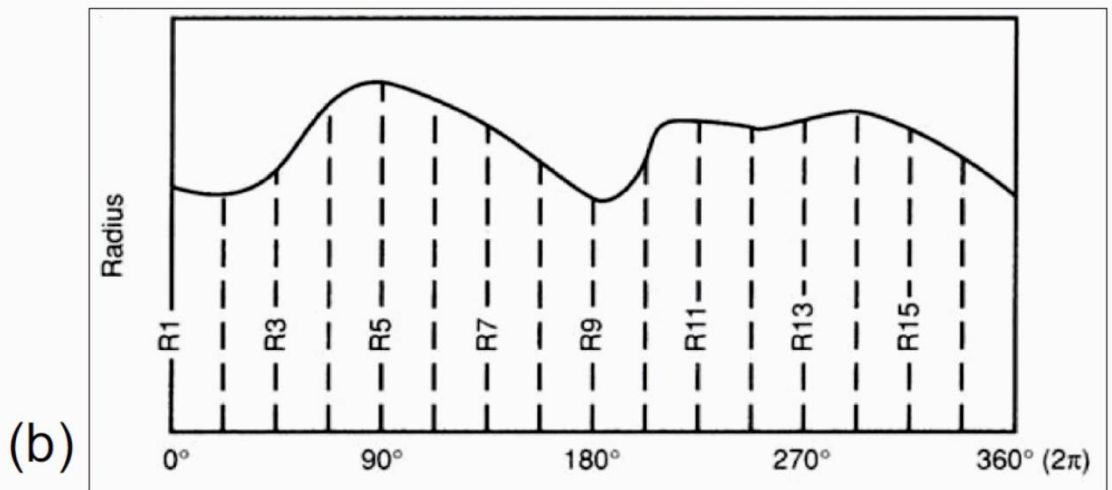
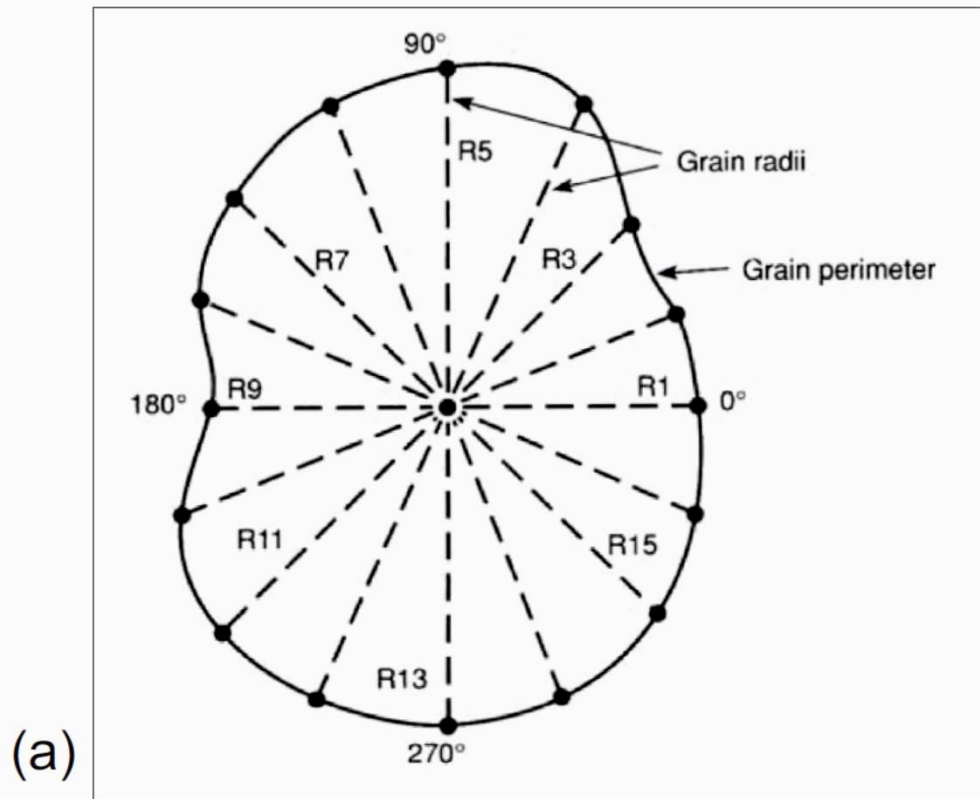
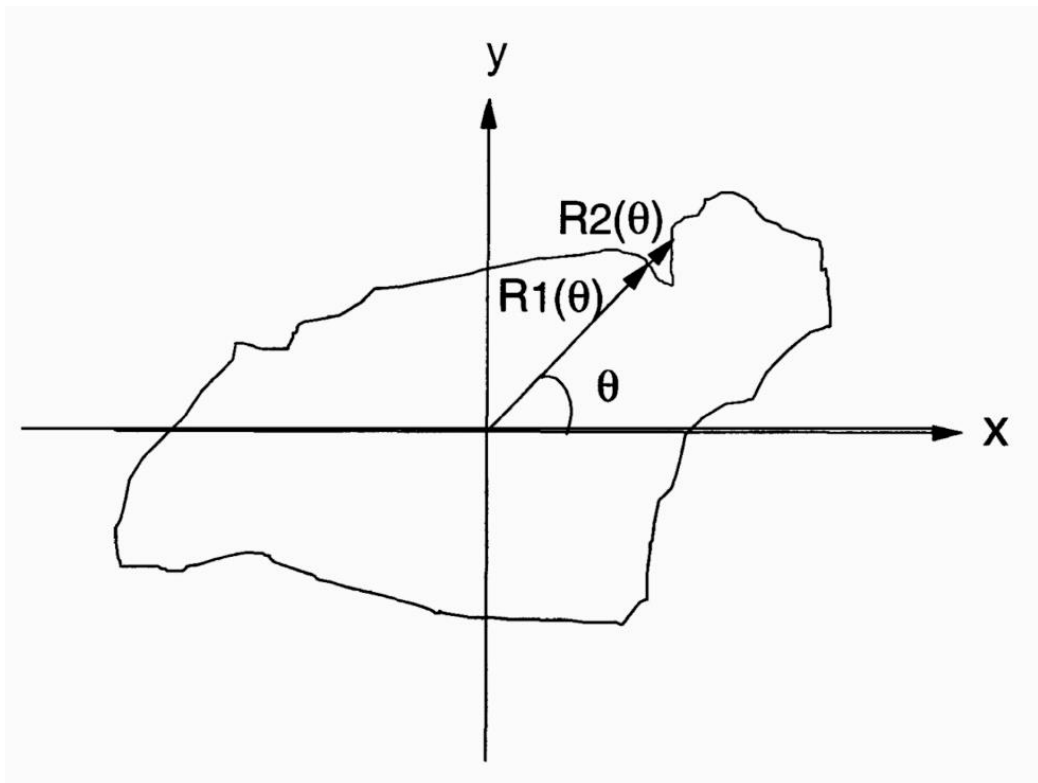


Figure 2.7: Unrolling of a grain boundary. (a) Grain boundary showing distance  $R(\theta)$  measurement from the centre of the grain. (b) Unrolled grain boundary represented by plot of  $\theta$  versus  $R(\theta)$  after Boggs, 2009.

In spite of being robust, Fourier analysis in this context is not ideal due to the re-entrant angle problem. Re-entrants are due to jagged or crenellate edge morphology in irregular shaped grains (Orford and Whalley, 1983) and leads to re-entrant angle or multi-valued function problem (Bowman et al., 2001; Thomas et al., 1995). This means that a displacement vector extended from the centroid towards the boundary intersects the boundary at two or more places (see Fig. 2.8). To overcome the shortcoming of re-entrant angle, Fourier descriptors are used.



*Figure 2.8: Grain boundary showing re-entrant angle problem (after Bowman et al, 2000). For a particular angle  $\theta$ ,  $R(\theta)$  is a multivalued function.*

Fourier descriptors were initially considered for shape analysis, but were discarded due to mathematical complexities and Fourier analysis was preferred at that time (Clark, 1981; Full and Ehrlich, 1982). However, later on, the benefits of the Fourier descriptor technique were recognised for image analysis applications in particular (Thomas et al., 1995). Using grain boundaries obtained from SEM images, Bowman

et al. (2001) demonstrated that grain morphology may be accurately represented using small numbers of Fourier descriptors.

In this technique, the grain boundary is first sampled at regular intervals. Each boundary point is represented in the complex plane by:

$$z_m = x_m + i y_m$$

where  $(x_m, y_m)$  are the coordinates,  $m$  goes from 0 to  $(N - 1)$  and  $N$  is the total number of sampled points.

The discrete Fourier transform is applied to the list of boundary points to obtain the list of descriptors as follows:

$$Z_k = \frac{1}{N} \sum_{m=0}^{N-1} z_m e^{-i \frac{2\pi m k}{N}} = \frac{1}{N} \sum_{m=0}^{N-1} z_m \left( \cos \frac{2\pi m k}{N} - i \sin \frac{2\pi m k}{N} \right)$$

The Fourier descriptors are  $Z_k = a_k + i b_k$  where  $k$  takes the values 0 to  $N - 1$ .

Applying the inverse Fourier transform to the descriptors retrieves estimates of the boundary points of a grain and thus can be used to reconstruct the original shape of the grain.

Often only a subset of the full set of Fourier descriptors are utilised for a grain. As the number of Fourier descriptors used to describe a shape increases, the boundary retrieved by the inverse transform becomes more accurate (see Fig. 2.9). Descriptors with low values of  $k$  tend to describe the major features of a grain whereas those with high values of  $k$  describe the finer morphological details.

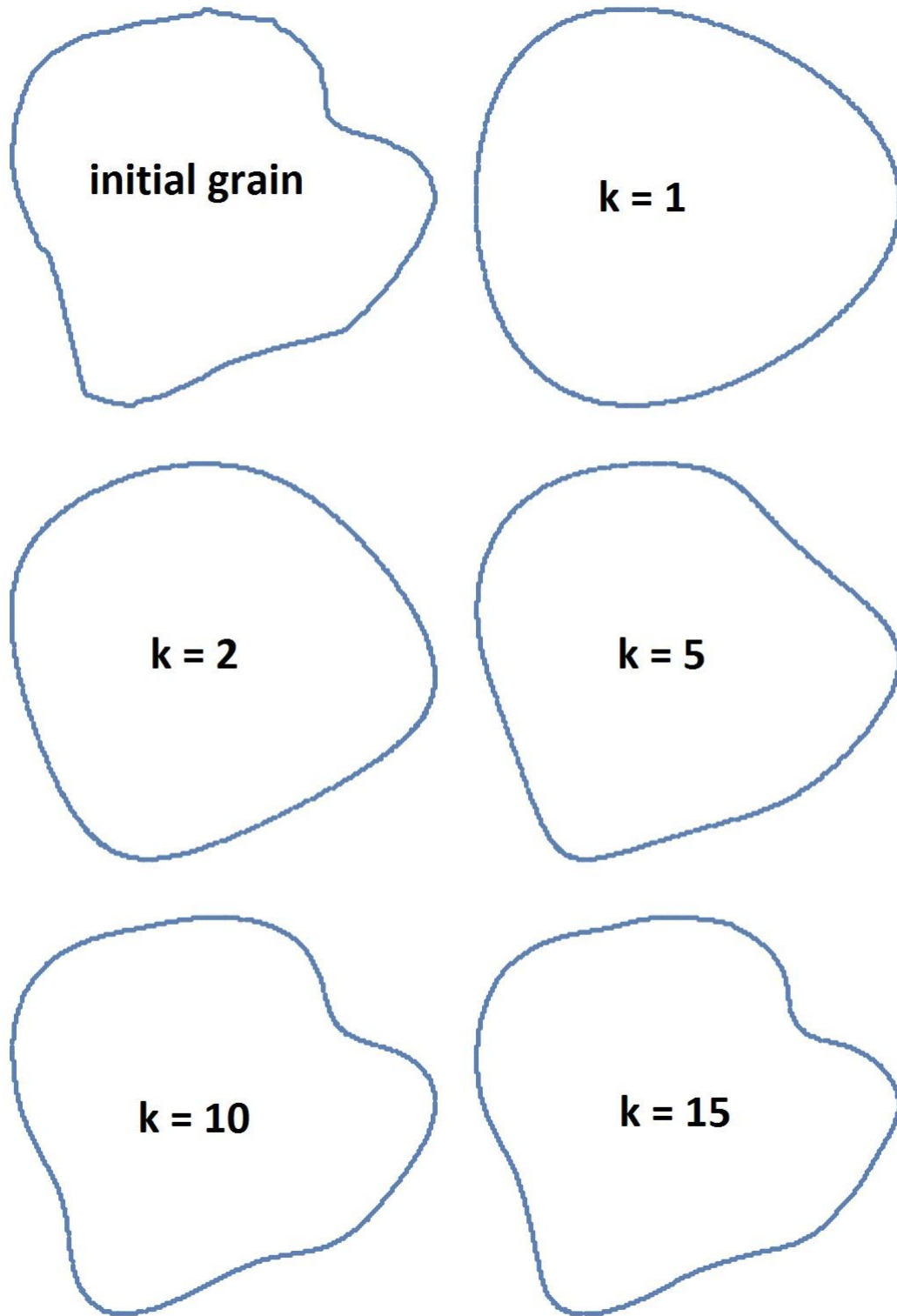


*Figure 2.9: Reconstructed particle boundary with the number of Fourier descriptors used from  $k=1$  to 15. Shows the increasing accuracy of the grain boundary with the number of descriptors used.*



### 2.2.2.7 Other parameters

Shape parameters, which are traditionally not taken into account from a sedimentological point of view but can prove useful in discriminating different types of sedimentary grains, are also included in this software. Cox and Budhu (2008) studied many simple parameters and identified key parameters to discriminate amongst sedimentary grains (see Table 2.2).

Shape Parameter	Formula	Description
Aspect Ratio	$L_{\text{major}}/L_{\text{minor}}$	Length of major axis by length of minor axis
Compactness	$\sqrt{4A/\pi}/L_{\text{major}}$	Diameter of circle of equivalent area to grain by length of major axis
ModRatio	$2R_i/\text{Feret}$	Diameter of largest inscribed circle divided by Feret diameter
Solidity	$A/A_{\text{convex}}$	Area by convex area
Convexity	$P_{\text{convex}}/P$	Convex perimeter by perimeter of grain
Rectangularity	$A/ A_{\text{BR}}$	Area of grain by area of bounding rectangle

*Table 2.2: Table of simple geometrical parameters used in the study.*

## 2.3 Methodology

Mathematica is used as the basis for this code and is a powerful technical computing environment with an excellent array of features and applications that run on a variety of operating systems such as Windows, Mac OS and Linux. Here it is used primarily for image analysis, feature extraction and general computation of size and shape parameters.

In the case of grains from lithified samples such as sandstone, photomicrographs of thin sections are used. Manual tracing of grain boundaries is performed because automated image analysis techniques are not yet satisfactory (Gorsevski et al., 2012; Lu et al., 2009; Mingireanov Filho et al., 2013; Roy Choudhury et al., 2006). It is recommended that tracing paper and black inking pens are used for tracing or,

alternatively, a graphics tablets may be used. Images consisting of black boundaries on a white background are the required input for the software (see Fig. 2.10b).

If a sample of unconsolidated (loose) sediment is to be analysed, then the process is much simpler and fully automated. Grains are recommended to be setup on the stage such that they do not touch each other. The image can be taken either using transmitted light below the stage or through a reflected light from above the stage. In case of image from transmitted light, the background is expected to be white with exceptions of dark region(s) representing grain(s). On the other hand, a black background with contrasting light coloured region(s) containing grain(s) is recommended for reflected light source image. Standard image analysis routines are provided to extract the boundary information in the required format (see Fig. 2.12b).

If grain size parameters are to be estimated, then an indication of the actual width of the image is also required. This ensures conversion of size parameters from pixel dimension to standard physical units. Once the required input file is generated the size and shape parameters can be computed through the code described in the next section. Additionally, results may be exported to variety of formats for further analysis if required.

## 2.4 Mathematica code

The Mathematica code is wrapped up in a single Mathematica package. Additionally, one example Mathematica notebook is provided demonstrating the analysis of a thin section and a loose sediment sample. These notebooks guide the user through the procedure, i.e. from image import to image analysis, feature extraction, and computation of all the parameters discussed in section 2. The implementation details are as follows:

### 2.4.1 Image Analysis

The **GrainBoundary** function is present only in the loose sediment analysis notebook. It detects the grain boundary using a threshold which can be changed, if required, by the user. The output of this step generates image similar to the manually traced image. All subsequent the steps are same for both loose sediment and thin section image analysis.

Two functions (**ProcessImage** and **RefineImage**) are written for image analysis purposes. The **ProcessImage** function takes as an argument the traced image file in bitmap (\*.bmp) format in the case of thin section analysis. For loose sediment analysis, the output of **GrainBoundary** is used as the input for the **ProcessImage** function. It performs the following tasks:

- (i) converts the input image into a binary image
- (ii) changes the image from step (i) to its inverted image
- (iii) generates a matrix by applying the Watershed transformation on the image from step (ii), at this stage all the grains are separately identified
- (iv) using the built-in Mathematica function (ComponentMeasurement), all the initial geometric information regarding the grains (e.g. length, width, orientation, centroid) are computed
- (v) another matrix is generated using the built-in Mathematica functions (Erosion, Thinning and Pruning) for identifying the boundary points of each grain.

After the ProcessImage function runs, it outputs a colourised image displaying individual grain regions in different colours with a unique label number (see Fig. 2.10c and 2.12c). Erroneous identifications may remain at this point, usually it occurs where boundaries of neighbouring grains meet and form a closed loop.

**RefineImage** is a function allowing users to remove any erroneously identified regions. It accepts as an argument a list of the labels of unacceptable grains and removes them from further processing. Once RefineImage is run, a revised colourised image of identified grain regions is presented. This step may be repeated until the user is satisfied with the output.

#### 2.4.2 Feature extraction

After the image analysis, the data is extracted from the image using the function **ExtractData**. This function extracts the coordinates of all the points lying on boundary, all the points lying inside the boundary and the relevant geometric data generated from **ProcessImage** function (from task (iv)). These data are passed on collectively as input to further functions to compute the shape and size of grains.

### 2.4.3 Computation of size and shape

The radius and the centre of the largest inscribed circle of each grain is computed by the function **InscribedCircle**. Here the Minimum distance from any point inside the grain boundary to the grain boundary is maximised using discrete optimisation with multiple starting points. Similarly, **CircumscribedCircle** function computes the smallest circumscribing circle over the grain boundary by minimising the maximum distance from any point inside the grain boundary to the grain boundary.

**SizeData** function is written to compute the actual size of grain regions by parameters listed in Table 2.1. This requires additional information about the width of the input image in a unit of the users choosing (i.e. microns or millimetres). Thus it has three arguments: the output from ProcessImage, CircumscribedCircle and the scaling factor.

The **FractalDivider** function computes the fractal dimension of each grain using the divider method. The unit divider lengths depend on the size of each individual grain (depending on the axes of the best fit ellipse).

The **Irregularity** function generates two matrices for each grain: the first represents points belonging to the grain and the second consists of points inside the best-fit ellipse of the grain. Thus, addition of the matrices identifies the non-overlapping region used for calculating irregularity.

The **Angularity** function converts the grain boundary into a  $n$  sided polygon and calculates the angle differences for the vertices (see section 2.2.4). The mean of the five highest differences is then calculated to calculate angularity. The number of sides of regular polygon that represents the grain boundary and the number of highest differences of consecutive angles can be varied by user.

The **Roundness** function first calculates the radius of curvature at each point on the boundary. It makes use of the function **CircumRadius**, which finds circle defined by three points (see Fig. 2.1a), and also uses the function **InscribedCircle** described earlier. Points with a radius of curvature greater than radius of the largest inscribed circle of the grain are omitted (see Fig. 2.1b) and the mean of the radius of curvature of the remaining points divided by radius of the largest inscribed circle is the roundness.

The **CircularityFactor** takes radius of the largest inscribed circle of the grain using **InscribedCircle** and the radius of the smallest circumscribing circle of the grain to compute circularity.

Fourier descriptors are computed using the **FourierDescriptor** function. In this function, the boundary is sampled at regular interval to take a total of  $n$  points for each grain, where  $n$  can be set by user. The centre of the grain boundary is shifted to the origin to compute the  $n$  number of Fourier descriptors. The output to a file type of user's choice can be exported using **FourierOutput** function.

#### 2.4.4 Results

Results obtained for all grains in a sample can be summarised in tabular form and exported to an excel file. Users can specify the parameters they wish to include in the output. The function **ResultTable**[*exdata\_*, *parameters\_*, *others\_*, *sizedata\_*] is written for this purpose. The argument *parameters\_* specifies the list of parameters that are required by the user. This provides flexibility and saves execution time. The third argument *others\_* may be either *True* or *False* and indicates whether or not to include in the output the other parameters in the result table. The fourth argument *sizedata\_* takes in the output from **SizeData**, if size is required. These other parameters include simple geometric data such as aspect ratio, rectangularity, convexity, modratio, compactness and solidity (see Table 2.1).

The **SizeTransform** function is available to convert a 2-D size distribution to a 3-D size distribution. This function takes size data from **SizeData** as input along with class distribution width and the numeral code for the type of size parameter to be used. A uniform distribution of initial 3-Dimensional size grains is assumed and the algorithm follows the method described in Heilbronner and Barrett (2014).

Finally, a data visualisation function called **GrainMapping** is present to display regions of grain using varying colour scheme based on output of a chosen shape or size parameter. This feature has been used in other image analysis tools (e.g. Heilbronner and Barrett, 2014) and is presented here for completeness.

## 2.5 Example analysis

One sample each of consolidated (rock thin section) and unconsolidated (loose sediment) is analysed to demonstrate the usage of this software package. A total of 60

grains were analysed for both examples. Details of the samples, their image preparation methodology and the sample analysis results are discussed below.

### 2.5.1 Rock thin section

A sandstone sample from Dingle Basin, South-West Ireland was collected for thin section analysis. The sample collected is from the Eask Sandstone Formation of the Dingle group and is relatively undeformed. The sediment grains in the sample were deposited in a fluvial type of depositional environment during the Lower Devonian (Allen and Crowley, 1983). The sample shows poorly sorted quartz grains surrounded by a clay matrix (Fig. 2.10a). The grains lie within the sub-rounded to angular category by visual analysis.

Thin section images of each sample in cross-polarised light were used for tracing out grain boundaries. Using more than one image of the same field of view at different stage orientations in cross-polarised light may increase clarity for tracing grain boundaries. An Intuos Pro Graphics Tablet was used to digitally trace the boundaries in CorelDRAW, which is a vector graphics editing software. Digital tracing of grain boundaries allows the flexibility of zooming in and out on the field of view and browse through microphotographs at different stage orientations while tracing. Each grain boundary is traced carefully so that they form a closed loop otherwise they are not detected as a separate region during the image processing step. It is important to ensure that the grain boundaries do not touch each other (Fig. 2.10b). The grain boundaries can be alternately traced physically on a tracing sheet and digitised for analysis (refer to Mulchrone et al. (2013) for details). The traced image is 1.86 Mb in size (1600\*1200 pixels). The physical size of the thin section image is 1640\*2186 Microns determined using Leica Microscope software.

The result of grain shape analysis from the sandstone thin section is presented in Figure 2.11. The datasets of roundness, circularity, irregularity and angularity exhibit normal distributions, whereas, fractal dimension and aspect ratio show positively skewed distributions. The mean and standard deviation of: roundness is 0.60 and 0.04; circularity is 0.76 and 0.06; irregularity is 0.17 and 0.05; and angularity is 53.92 and 10.94. The median of fractal dimension and aspect ratio is 1.03 and 1.51 respectively.

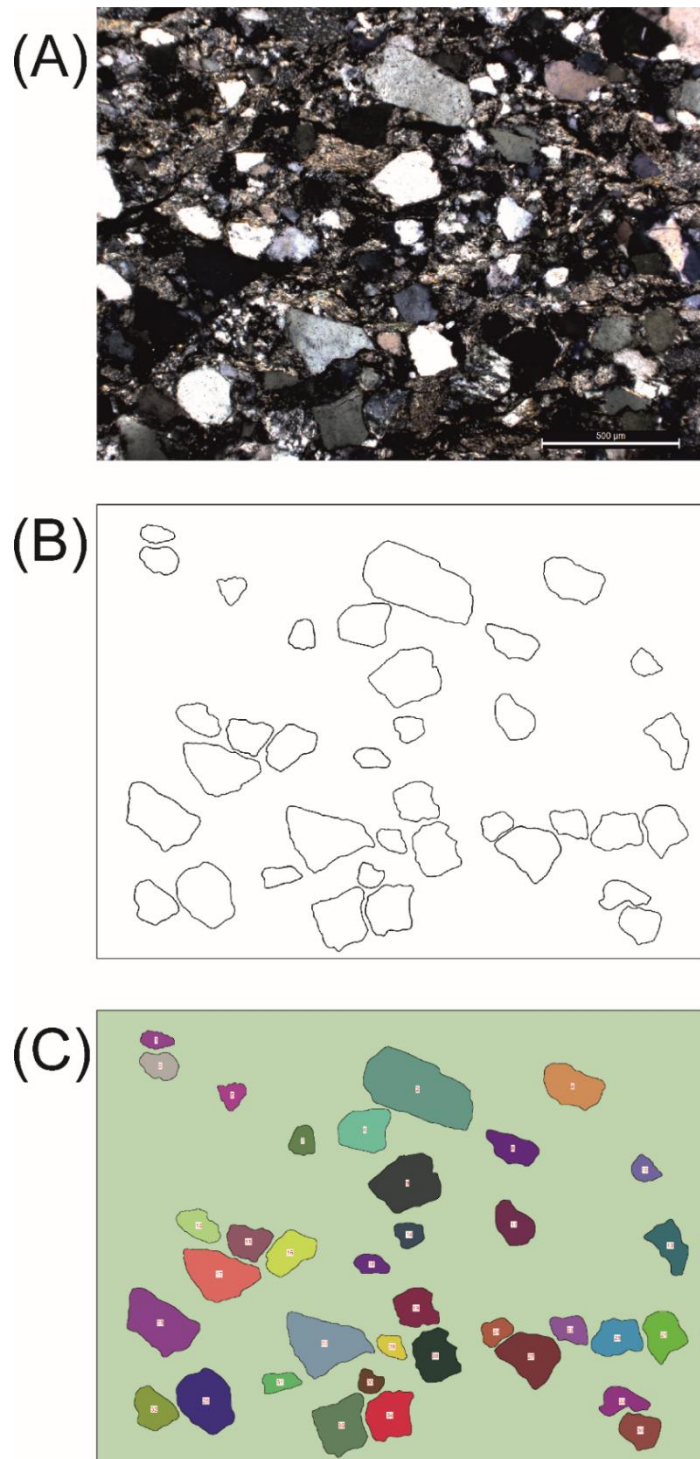


*Figure 2.10: (a) Shows thin section microphotograph of sandstone sample collected from Dingle, County Kerry, Ireland. (b) Grain boundary of the clasts from thin section is manually traced using graphics tablet (c) image analysis of traced grain boundary shows region in randomly assigned colours identified as individual grains.*

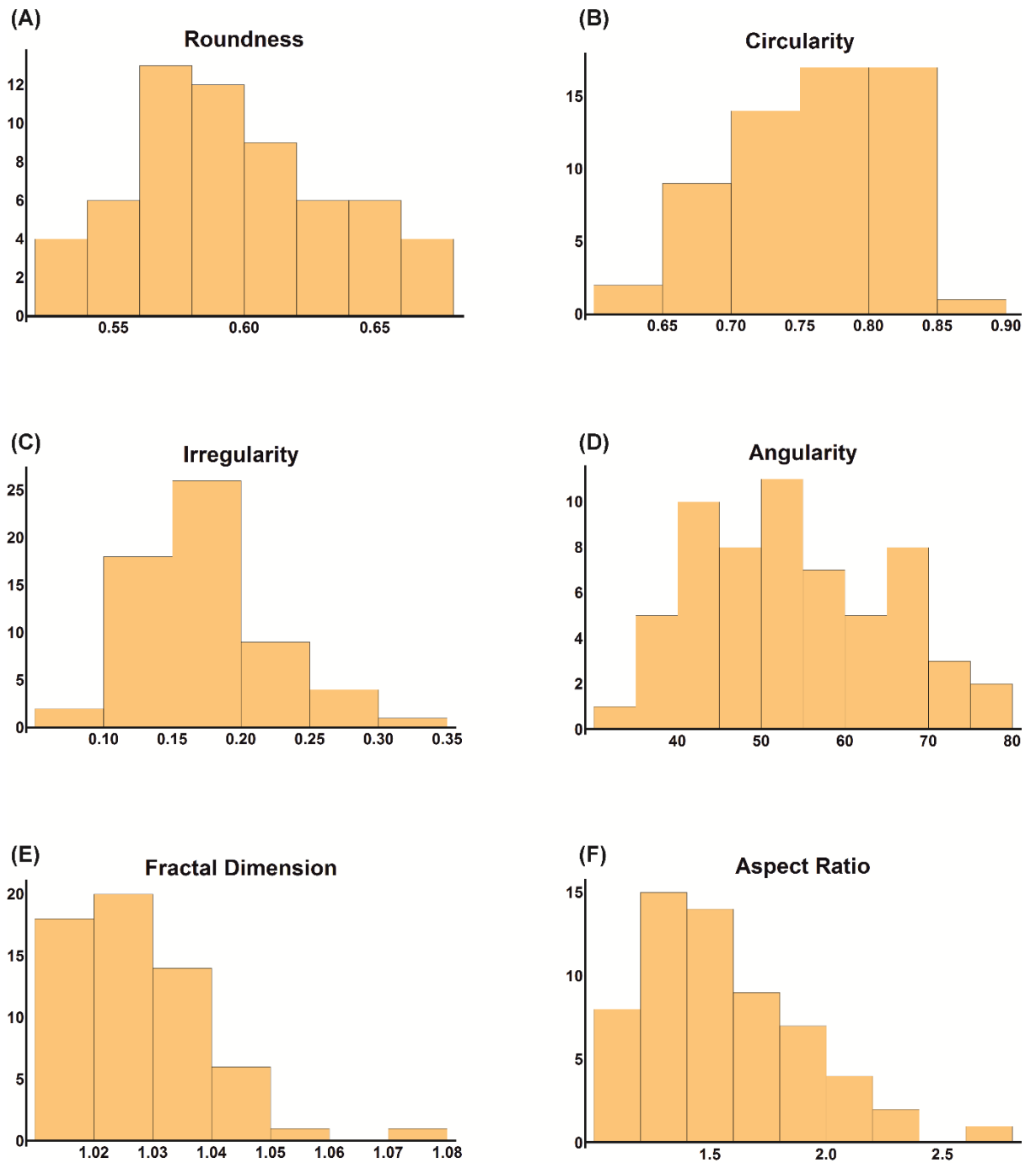


*Figure 2.11: Results from thin section photomicrograph analysis of sandstone sample represented by histogram for: (a) roundness; (b) circularity; (c) irregularity; (d) angularity; (e) fractal dimension; and (f) aspect ratio data*



### 2.5.2 Loose sediment

A loose sediment sample from Ballycotton beach, County Cork, Ireland was collected for grain shape analysis. The Devonian Old Red Sandstone clastic sedimentary rocks is assumed to be the source of beach sediments.

The sample is treated with diluted Hydro Chloric acid to remove any biogenic particles, if present. It is then dried in an oven at 40 °C for 24 hours. Next, the sample is dry sieved to separate the different size fractions. For this analysis, the 250 to 500 Microns size fraction is used. The sand grains are carefully settled on the microscope stage parallel to their longest and intermediate axis. Using a paint brush, these grains are set up such that they do not touch each other and remain within the field of view of the microscope. For each field of view, 5-7 grains were imaged (see Fig. 2.12a). The images were captured at 140X for 1640\*2186 microns field of view at 1200\*1600 Pixel resolution. The following settings were used for the microscope for transmitted light from beneath the stage: exposure 61.4 ms; saturation: 1.3; gain: 1.0X; gamma 1.29.

Figure 2.13 shows the population distribution of shape parameters for the loose sediment sample. Roundness, angularity, irregularity and fractal dimension data display a normal distribution. Circularity data for the population show a negative skew, whereas, there is positive skewness in the aspect ratio data distribution. The mean and standard deviation of: roundness is 0.61 and 0.04; angularity is 54.04 and 10.93; irregularity is 0.14 and 0.05; and fractal dimension is 1.02 and 0.01 respectively. The median of circularity and aspect ratio data is 0.82 and 1.32 respectively.

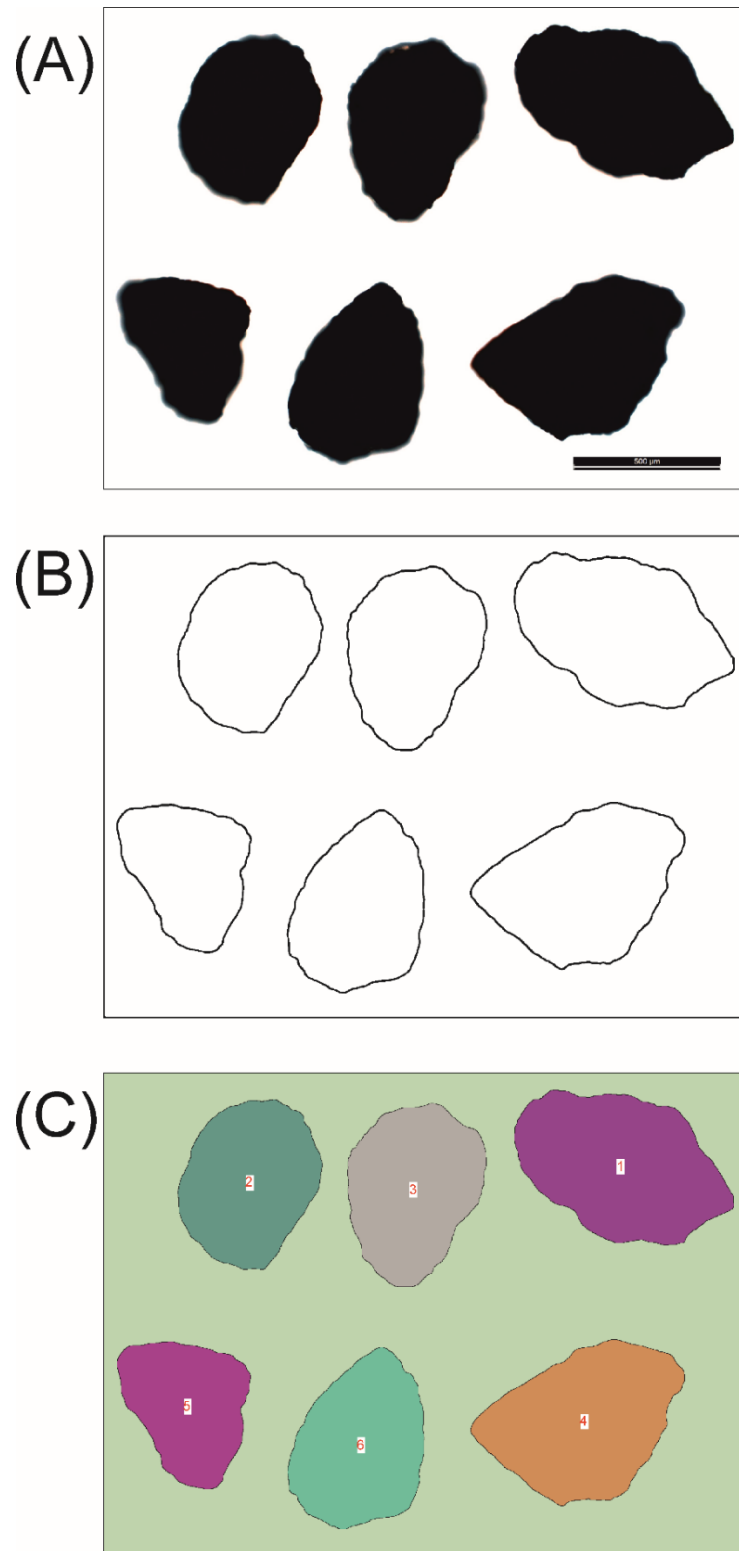


*Figure 2.12: Image analysis routine for loose sediment analysis. (a) Shows thin section microphotograph of loose sand sample collected from Ballycotton, County Cork, Ireland. (b) Grain boundary of the clasts from thin section is manually traced using graphics tablet (c) image analysis of traced grain boundary shows region in randomly assigned colours identified as individual grains.*

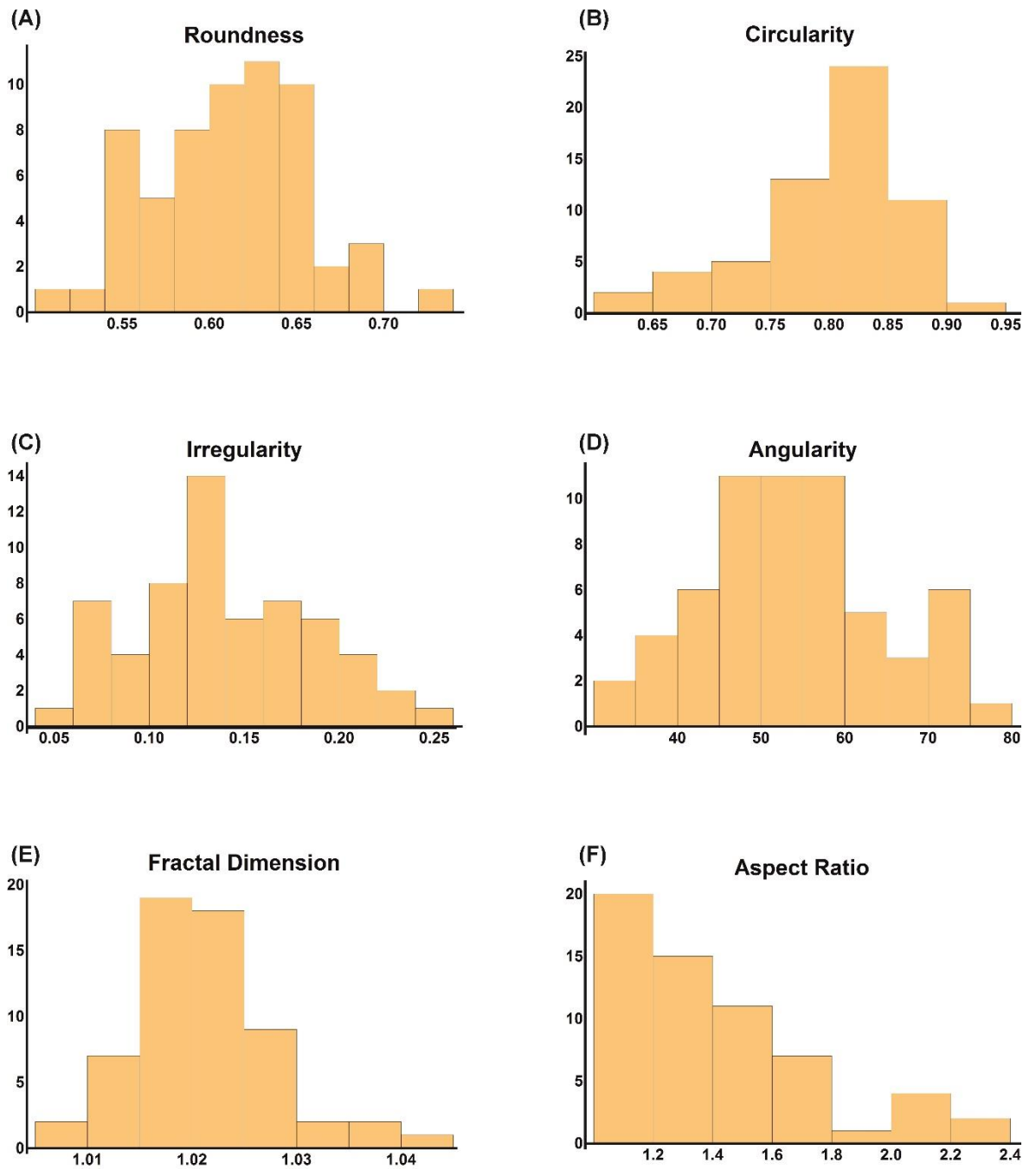


Figure 2.13: Results from photomicrograph analysis of loose sediment sample represented by histogram for: (a) roundness; (b) circularity; (c) irregularity; (d) angularity; (e) fractal dimension; and (f) aspect ratio data

## 2.6 Discussion

The image analysis package presented in this paper can be used to measure a range of size and shape parameters. Different measures of size give different grain size distributions for the same population of grains (Heilbronner and Barrett, 2014). Therefore, a suite of size parameters implemented here gives the user the freedom to pick the parameters of choice. For thin section images, 2-Dimensional grain size distribution should be transformed into 3-Dimensional size distribution for analysis.

The software package offers a variety of shape parameters for analysis. More than one shape parameter can be used to better characterise a grain (Blott and Pye, 2008). The shape parameters implemented here were tested on regular geometric shapes (Blott and Pye, 2008) and were found to perform well. Apart from the parameters presented here, some additional information regarding the grains can be further obtained implicitly from the results. For example, area and perimeter of grains can be calculated from the size measures  $S_d$  and  $S_p$ . Such information can be extracted, if required by the users.

The manual grain boundary tracing for thin section analysis can be regarded by some as a tedious exercise. However, in the light of unavailability of an automated grain boundary segmentation algorithm that can be used for any type of thin section image, manual grain boundary tracing provides the best alternative at present. High quality shape and size information can be easily obtained once the boundary is traced. Furthermore, the whole methodology is relatively cheap to perform. If new analysis techniques emerge which can process messy natural data, the analysis software presented here will be fully compatible and the process can be fully automated.

The shape parameters calculated using grain boundary data in this package is independent of size. However, a grain of a very small pixel size is prone to be affected by its size for shape calculation (Kröner and Doménech Carbó, 2013). Regular geometric and irregular shape with increasing pixel count were used to test this package to check variation of parameter values with varying pixel count for a fixed shape. It was found it is not affected by size ( $S_c$ ) above 85 pixels. Thus a higher pixel resolution is recommended for good results.

The contribution presented here will help in standardising shape analysis methodology used in the domain of sedimentology. The use of the software package introduced here

has been demonstrated by examples with sand sized grains. However, it can be used for particles of any size. Therefore, the image analysis package can be of use to variety of users for diverse shape analysis objectives.

## 2.7 Conclusion

In this paper, a Mathematica package for analysis and determination of textural elements of siliciclastic grains is presented. Following a brief review of currently used shape and size measurement parameters, a suite of 12 shape parameters (roundness, circularity, angularity, irregularity, fractal dimension, Fourier descriptors, aspect ratio, mod ratio, compactness, rectangularity, convexity and solidity) and 6 size parameters ( $S_d$ ,  $S_a$ ,  $S_b$ ,  $S_p$ ,  $S_c$  and  $S_m$ ) are selected for implementation in the image analysis package. Improvement have been suggested to the angularity and the irregularity parameters. The usage of presented software code has been demonstrated using photomicrographs from a sandstone thin section and a loose sediment sample. Manual tracing of grains of thin section grain boundaries is recommended, whereas, a fully automated approach is available for loose sediment analysis.

The software along with the methodology proposed in this paper, has the potential for allowing access to quantitative data for textural elements of siliciclastic grains. Thus, it has the potential to provide important information for a wide range of sedimentary studies. Future work in the direction of quantitative textural analysis of sedimentary grains include development of a statistical approach aimed at synthesis and analysis of distributions of sediment grain shape population data.

## 2.8 Acknowledgement

This project is funded by the Irish Shelf Petroleum Studies Group (ISPSG) of the Irish Petroleum Infrastructure Programme (PIP) Group 4. The ISPSG comprises: Atlantic Petroleum (Ireland) Ltd, Cairn Energy Plc, Chrysaor E&P Ireland Ltd, Chevron North Sea Limited, ENI Ireland BV, Europa Oil & Gas (Holdings) plc, ExxonMobil E&P Ireland (Offshore) Ltd., Kosmos Energy LLC, Maersk Oil North Sea UK Ltd, Petroleum Affairs Division of the Department of Communications, Energy and Natural Resources, Providence Resources plc, Repsol Exploración SA, San Leon

Energy Plc, Serica Energy Plc, Shell E&P Ireland Ltd, Sosina Exploration Ltd, Statoil (UK) Ltd, Tullow Oil Plc and Woodside Energy (Ireland) Pty Ltd.

## 2.9 References

- Al-Rousan, T., Masad, E., Tutumluer, E. and Pan, T.** (2007) Evaluation of image analysis techniques for quantifying aggregate shape characteristics. *Construction and Building Materials*, **21**, 978-990.
- Allen, J. and Crowley, S.** (1983) Lower Old Red Sandstone fluvial dispersal systems in the British Isles. *Earth and Environmental Science Transactions of The Royal Society of Edinburgh*, **74**, 61-68.
- Aschenbrenner, B.C.** (1956) A new method of expressing particle sphericity. *Journal of Sedimentary Research*, **26**, 15-31.
- Barrett, P.J.** (1980) The shape of rock particles, a critical review. *Sedimentology*, **27**, 291-303.
- Blatt, H.** (1992) *Sedimentary Petrology*. W. H. Freeman and Company, New York, 514 pp.
- Blatt, H., Middleton, G.V. and Murray, R.C.** (1972) *Origin of sedimentary rocks*. Prentice-Hall Inc., New Jersey, 634 pp.
- Blott, S.J. and Pye, K.** (2008) Particle shape: a review and new methods of characterization and classification. *Sedimentology*, **55**, 31-63.
- Boggs, S.** (2009) *Petrology of sedimentary rocks*. Cambridge University Press, Cambridge, 612 pp.
- Bowman, E.T., Soga, K. and Drummond, W.** (2001) Particle shape characterisation using Fourier descriptor analysis. *Géotechnique*, **51**, 545-554.
- Burger, H. and Skala, W.** (1976) Comparison of sieve and thin-section technique by a Monte-Carlo model. *Computers & Geosciences*, **2**, 123-139.
- Campaña, I., Benito-Calvo, A., Pérez-González, A., Bermúdez de Castro, J.M. and Carbonell, E.** (2016) Assessing automated image analysis of sand grain shape to identify sedimentary facies, Gran Dolina archaeological site (Burgos, Spain). *Sedimentary Geology*, **346**, 72-83.
- Chandan, C., Sivakumar, K., Masad, E. and Fletcher, T.** (2004) Application of Imaging Techniques to Geometry Analysis of Aggregate Particles. *Journal of Computing in Civil Engineering*, **18**, 75-82.
- Charpentier, I., Sarocchi, D. and Rodriguez Sedano, L.A.** (2013) Particle shape analysis of volcanic clast samples with the Matlab tool MORPHEO. *Computers & Geosciences*, **51**, 172-181.

- Clark, M.W.** (1981) Quantitative shape analysis: A review. *Journal of the International Association for Mathematical Geology*, **13**, 303-320.
- Cox, E.P.** (1927) A method of assigning numerical and percentage values to the degree of roundness of sand grains. *J Paleontol*, **1**.
- Cox, M.R. and Budhu, M.** (2008) A practical approach to grain shape quantification. *Engineering Geology*, **96**, 1-16.
- Eamer, J.B.R., Shugar, D.H., Walker, I.J., Lian, O.B. and Neudorf, C.M.** (2017) Distinguishing Depositional Setting For Sandy Deposits In Coastal Landscapes Using Grain Shape. *Journal of Sedimentary Research*, **87**, 1-11.
- Ehrlich, R. and Weinberg, B.** (1970) An exact method for characterization of grain shape. *Journal of Sedimentary Research*, **40**.
- Full, W.E. and Ehrlich, R.** (1982) Some approaches for location of centroids of quartz grain outlines to increase homology between Fourier amplitude spectra. *Journal of the International Association for Mathematical Geology*, **14**, 43-55.
- Gorsevski, P.V., Onasch, C.M., Farver, J.R. and Ye, X.** (2012) Detecting grain boundaries in deformed rocks using a cellular automata approach. *Computers & Geosciences*, **42**, 136-142.
- Harrell, J. and Eriksson, K.** (1979) Empirical conversion equations for thin-section and sieve derived size distribution parameters. *Journal of Sedimentary Research*, **49**, 273-280.
- Heilbronner, R. and Barrett, S.** (2014) *Image analysis in earth sciences: microstructures and textures of earth materials*. Springer 520 pp.
- Higgins, M.D.** (2000) Measurement of crystal size distributions. *American Mineralogist*, **85**, 1105-1116.
- Hyslip, J.P. and Vallejo, L.E.** (1997) Fractal analysis of the roughness and size distribution of granular materials. *Engineering Geology*, **48**, 231-244.
- Illenberger, W.K.** (1991) Pebble shape (and size!). *Journal of Sedimentary Research*, **61**, 756-767.
- Janoo, V.C.** 1998. Quantification of Shape, Angularity and Surface Texture of Base Course Materials., US Army Corps of Engineers Cold Regions Research and Engineering Laboratory, Hanover, NH.
- Kong, M., Bhattacharya, R.N., James, C. and Basu, A.** (2005) A statistical approach to estimate the 3D size distribution of spheres from 2D size distributions. *GSA Bulletin*, **117**, 244-249.
- Kröner, S. and Doménech Carbó, M.T.** (2013) Determination of minimum pixel resolution for shape analysis: Proposal of a new data validation method for computerized images. *Powder Technology*, **245**, 297-313.

- Krumbein, W.C.** (1941) Measurement and geological significance of shape and roundness of sedimentary particles. *J Sediment Petrol*, **11**, 64-72.
- Lees, G.** (1964) A new method for determining the angularity of particles. *Sedimentology*, **3**, 2-21.
- Lira, C. and Pina, P.** (2009) Automated grain shape measurements applied to beach sands. *J Coastal Res Spec Issue*, **56**, 1527-1531.
- Lu, B., Cui, M., liu, Q. and Wang, Y.** (2009) Automated grain boundary detection using the level set method. *Computers & Geosciences*, **35**, 267-275.
- Mandelbrot, B.B.** (1982) *The fractal geometry of nature*. WH freeman New York, New York, 468 pp.
- Masad, E., Button, J. and Papagiannakis, T.** (2000) Fine-Aggregate Angularity: Automated Image Analysis Approach. *Transportation Research Record: Journal of the Transportation Research Board*, **1721**, 66-72.
- Masad, E. and Button, J.W.** (2000) Unified Imaging Approach for Measuring Aggregate Angularity and Texture. *Computer-Aided Civil and Infrastructure Engineering*, **15**, 273-280.
- Masad, E., Olcott, D., White, T. and Tashman, L.** (2001) Correlation of Fine Aggregate Imaging Shape Indices with Asphalt Mixture Performance. *Transportation Research Record: Journal of the Transportation Research Board*, **1757**, 148-156.
- Mingireanov Filho, I., Vallin Spina, T., Xavier Falcão, A. and Campana Vidal, A.** (2013) Segmentation of sandstone thin section images with separation of touching grains using optimum path forest operators. *Computers & Geosciences*, **57**, 146-157.
- Mulchrone, K.F., McCarthy, D.J. and Meere, P.A.** (2013) Mathematica code for image analysis, semi-automatic parameter extraction and strain analysis. *Computers & Geosciences*, **61**, 64-70.
- Orford, J.D. and Whalley, W.B.** (1983) The use of the fractal dimension to quantify the morphology of irregular-shaped particles. *Sedimentology*, **30**, 655-668.
- Pentland, A.** (1927) A method of measuring the angularity of sands. *Proceedings and Transactions of the Royal Society of Canada*, **21**, 43.
- Peterson, T.D.** (1996) A refined technique for measuring crystal size distributions in thin section. *Contributions to Mineralogy and Petrology*, **124**, 395-405.
- Pettijohn, F.J.** (1957) *Sedimentary rocks*. Harper and Row Publishers, New York, 718 pp.
- Powers, M.C.** (1953) A new roundness scale for sedimentary particles. *Journal of Sedimentary Research*, **23**, 117-119.
- Rao, C., Tutumluer, E. and Kim, I.T.** (2002) Quantification of Coarse Aggregate Angularity Based on Image Analysis. *Transportation Research Record: Journal of the Transportation Research Board*, **1787**, 117-124.
- Riley, N.A.** (1941) Projection sphericity. *Journal of Sedimentary Research*, **11**, 94-97.



- Roduit, N.** (2007) *JMicroVision: A Multipurpose Image Analysis Software Tool* University of Geneva Geneva, 128 pp.
- Roussillon, T., Piégay, H., Sivignon, I., Tougne, L. and Lavigne, F.** (2009) Automatic computation of pebble roundness using digital imagery and discrete geometry. *Computers & Geosciences*, **35**, 1992-2000.
- Roy Choudhury, K., Meere, P.A. and Mulchrone, K.F.** (2006) Automated grain boundary detection by CASRG. *Journal of Structural Geology*, **28**, 363-375.
- Schneider, C.A., Rasband, W.S. and Eliceiri, K.W.** (2012) NIH Image to ImageJ: 25 years of image analysis. *Nature Methods*, **9**, 671.
- Sneed, E.D. and Folk, R.L.** (1958) Pebbles in the lower Colorado River, Texas a study in particle morphogenesis. *The Journal of Geology*, **66**, 114-150.
- Sochan, A., Zieliński, P. and Bieganski, A.** (2015) Selection of shape parameters that differentiate sand grains, based on the automatic analysis of two-dimensional images. *Sedimentary Geology*, **327**, 14-20.
- Suzuki, K., Fujiwara, H. and Ohta, T.** (2015) The evaluation of macroscopic and microscopic textures of sand grains using elliptic Fourier and principal component analysis: Implications for the discrimination of sedimentary environments. *Sedimentology*, **62**, 1184-1197.
- Tafesse, S., Robison Fernlund, J.M., Sun, W. and Bergholm, F.** (2013) Evaluation of image analysis methods used for quantification of particle angularity. *Sedimentology*, **60**, 1100-1110.
- Takashimizu, Y. and Iiyoshi, M.** (2016) New parameter of roundness R: circularity corrected by aspect ratio. *Progress in Earth and Planetary Science*, **3**, 2.
- Thomas, M.C., Wiltshire, R.J. and Williams, A.T.** (1995) The use of Fourier descriptors in the classification of particle shape. *Sedimentology*, **42**, 635-645.
- Wadell, H.** (1932) Volume, Shape, and Roundness of Rock Particles. *The Journal of Geology*, **40**, 443-451.
- Wadell, H.** (1933) Sphericity and roundness of rock particles. *The Journal of Geology*, **41**, 310-331.
- Wadell, H.** (1935) Volume, shape, and roundness of quartz particles. *The Journal of Geology*, **43**, 250-280.
- Wang, L., Park, J. and Mohammad, L.** (2003) Quantification of morphology characteristics of aggregate from profile images. In: *Proceedings of 82nd Transportation Research Board Annual Meeting, Washington, DC*.
- Wang, L.D., Sun, W., E.M., L., A., W. and Druta, C.** 2012. Application of LADAR in the Analysis of Aggregate Characteristics., *NCHRP 4-34 report*, Washington DC.
- Wentworth, C.K.** (1919) A laboratory and field study of cobble abrasion. *The Journal of Geology*, **27**, 507-521.

### **3 Quantitative characterisation of grain shape: Implications for textural maturity analysis and discrimination between depositional environments**

*Mohit Tunwal<sup>1)2)</sup>\*, Kieran F. Mulchrone<sup>2)</sup> and Patrick A. Meere<sup>1)</sup>*

(Current status: accepted for publication, *Sedimentology*)

*<sup>1)</sup> School of Biological, Earth and Environmental Sciences, University College Cork, Distillery Fields, North Mall, Cork, Ireland*

*<sup>2)</sup> School of Mathematical Sciences, University College Cork, Western Gateway Building, Western Road, Cork, Ireland*

#### **Abstract**

Grain shape plays an important role in textural analysis of sedimentary grains. Textural analysis helps determine the formation, transportation and deposition processes of sedimentary rocks. However, there is a lack of standardised methodology for quantitative characterisation of grain shapes. The utility of fully automated image analysis for grain shape measurement is assessed in this paper. This research aims to identify the most useful shape parameters for textural characterisation of populations of grains and determine the relative importance of the parameters. A key aspect of this study is to determine whether, in a particular sedimentary environment, textural maturity of the samples can be ranked based on their grain shape data. Furthermore, discrimination of sedimentary depositional environments is explored on the basis of grain shape. In this study, 20 loose sediment samples from four known depositional environments (beach, aeolian, glacial and fluvial) were analysed using newly implemented automatic image analysis methods. For each sample, a set of 11 shape parameters were calculated for 200 grains. The data demonstrates a progression in textural maturity in terms of roundness, angularity, irregularity, fractal dimension, convexity, solidity and rectangularity. Furthermore, statistical analysis provides strong support for significant differences between samples grouped by environment and

generates a ranking consistent with trends in maturity. Based on novel application of machine learning algorithms, angularity and fractal dimension are found to be the two most important parameters in texturally classifying a grain. The results of this study indicate that textural maturity is readily categorised using automated grain shape parameter analysis. However, it is not possible to absolutely discriminate between different depositional environments on the basis of shape parameters alone. This work opens up the possibility of detailed studies of the relationship between textural maturity and sedimentary environment, which may be more complicated than previously considered.

\*Corresponding author: [mohittunwal@gmail.com](mailto:mohittunwal@gmail.com)

Keywords: Grain shape, texture, sedimentary environment discrimination, image analysis, textural maturity, shape measurement

### 3.1 Introduction

Sedimentary textures, encompassing size, shape and fabric, can provide information on the sedimentological history of a clastic sediment particularly in relation to mode of transportation and depositional environment (Pettijohn, 1957). Study of such features has been a popular area of research in sedimentology over the years and is of continuing interest (e.g. Suzuki et al., 2015; Takashimizu and Iiyoshi, 2016). In the past century many shape parameters have been proposed for textural analysis of sediments and their efficacy has been assessed (Barrett, 1980; Blott and Pye, 2008). However, there still needs to be some consensus within the sedimentological community to standardise the use of grain shape data and optimal measurement methodologies. A probable reason for this, up until quite recently, may be related to tedious manual grain shape measurements and associated complex shape parameter calculations (Pettijohn et al., 1972). Visual charts were used in the past to overcome such challenges (Krumbein, 1941; Powers, 1953) but such analysis is subjective and qualitative in nature.

Qualitative shape characterisation is typically subject to sub-conscious operator bias (Blatt, 1992). Thus results obtained from different studies are difficult to compare. Even with the same researcher it cannot be guaranteed that the same result is reproduced (Blatt et al., 1972). Other issues with qualitative analysis concerns the way results are presented. For example, a sample might be described by a single phrase, e.g. subrounded to subangular, and intended to categorically characterise the overall grain population. However, there is a loss of information because the variation within the grain population distribution is not communicated. Studies in which each grain of the population is classified individually using visual chart typically results in an ordinal dataset. By contrast, quantitative analysis results a continuous dataset.

With the rapid progress made in computation, image analysis techniques are increasingly being employed for grain shape measurement in the field of civil engineering in particular (Al-Rousan et al., 2007; Tafesse et al., 2013). However, evidence for such rapid development in not so clear in sedimentology. To address this deficit in quantitative approaches to sedimentary petrology, this paper seeks to:

1. Identify which of the many grain shape parameters are useful in the textural characterisation of sediments.
2. Determine a suite of parameters correlated with textural maturity and their potential in ordering samples in relative order of maturity.
3. Empirically explore the validity of using population level measurements to discriminate between different sedimentary environments.

Selection of grain shape parameters needs to be done with two objectives in mind: 1) to assess their potential in characterisation of individual grains and 2) to evaluate their usefulness in for specific purposes in sedimentology. For example, the Krumbein chart has been used as a reference scale to select shape parameters for grain shape characterisation, however, this approach has been demonstrated to suffer from objectivity (Sochan et al., 2015).

Textural maturity of sediments depends on the clay content, sorting of non-clay particles and shape of grains (Folk, 1951). It is postulated that with an increase in total modifying energy expended on sediments, their textural maturity increases (Ehlers and Blatt, 1982; Friedman and Sanders, 1978). Grain shape for textural maturity is usually

studied in terms of roundness. In this paper, textural maturity refers to the roundness and smoothness of grain boundaries due to the abrasive processes that the grain encounters. Shape analysis has previously been applied with some success to distinguish textural maturity between sedimentary facies using convexity, circularity and aspect ratio (Campaña et al., 2016).

Shape measurements can provide insight into the depositional history of grains (Tucker, 2001). However, their sole use in discriminating depositional environment has been a matter of debate (Boggs, 2009). Nonetheless, they can be employed in typifying a given sand body in ancient examples (Reineck and Singh, 1975). Even with the introduction of image analysis and computational techniques there has been a dearth of work in this area. One study uses elliptic Fourier analysis along with principle component analysis in an attempt to discriminate sedimentary environments using 15 grains per sample for 48 samples (Suzuki et al., 2015). In another study, samples from known aeolian and littoral environments were subjected to quantitative shape analysis (Eamer et al., 2017) to assess potential for discrimination of environment, however, the study was limited to four parameters.

This work builds on and contributes to recent efforts in the direction of quantitative analysis of sand grains (Lira and Pina, 2009; Suzuki et al., 2015; Sochan et al., 2015; Campaña et al., 2016; Eamer et al., 2017). Using a consistently large sample size (i.e. 200 grains) and employing a range of shape parameters with suggested improvements, this work hopes to open up the avenue for future grain shape distribution studies.

## 3.2 Sampling

Loose sediment samples from four different sedimentary environments: fluvial, glacial, beach and aeolian were collected for this study. A total of 20 sampling sites of which 6 were fluvial, 4 glacial, 6 beach and 4 aeolian were studied (see Table 3.1). Multiple sampling sites for the same depositional environment were selected to investigate the variation within them as well as between the four environment types. The sediment source lithology type for all the samples is sedimentary in nature.

Glacial sediments were sampled from the Late Pleistocene deposits of the Last Glacial Maximum (LGM) in County Cork, Ireland (Ó Cofaigh et al., 2012). Two samples were

collected from a glacial till at Myrtleville (G1 and G2) and one sample each from glacial tills at Ballycotton and Church Bay (G3 and G4, see Fig. 3.1). The source of these glacial sediments are local Devonian-Carboniferous siliciclastic sedimentary rocks.

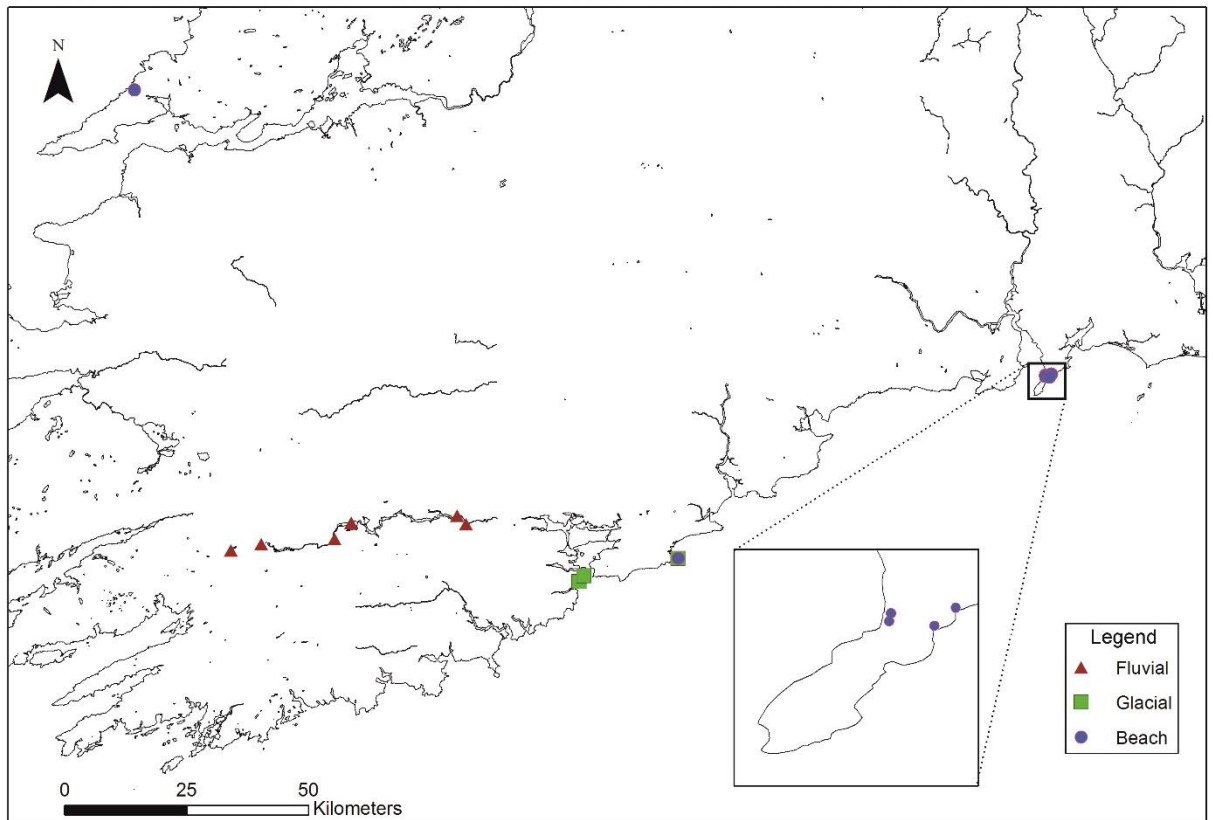


*Figure 3.1: Map showing sampling locations for fluvial, glacial and beach samples in Ireland.*

Aeolian sediments were sampled from the Thar desert, India (see Fig. 3.2). The source for the aeolian sand is attributed to the underlying alluvial sediments which were later reworked by aeolian processes (Pant, 1993). The four sampling sites are Bikaner (A1), Jaisalmer (A2), Salasar (A3) and Jodhpur (A4). In terms of dune types, sand sheets are present at Jodhpur and Jaisalmer, transitional parabolic dunes are present at Salasar, and transverse dunes are present at Bikaner (Singhvi and Kar, 2004).

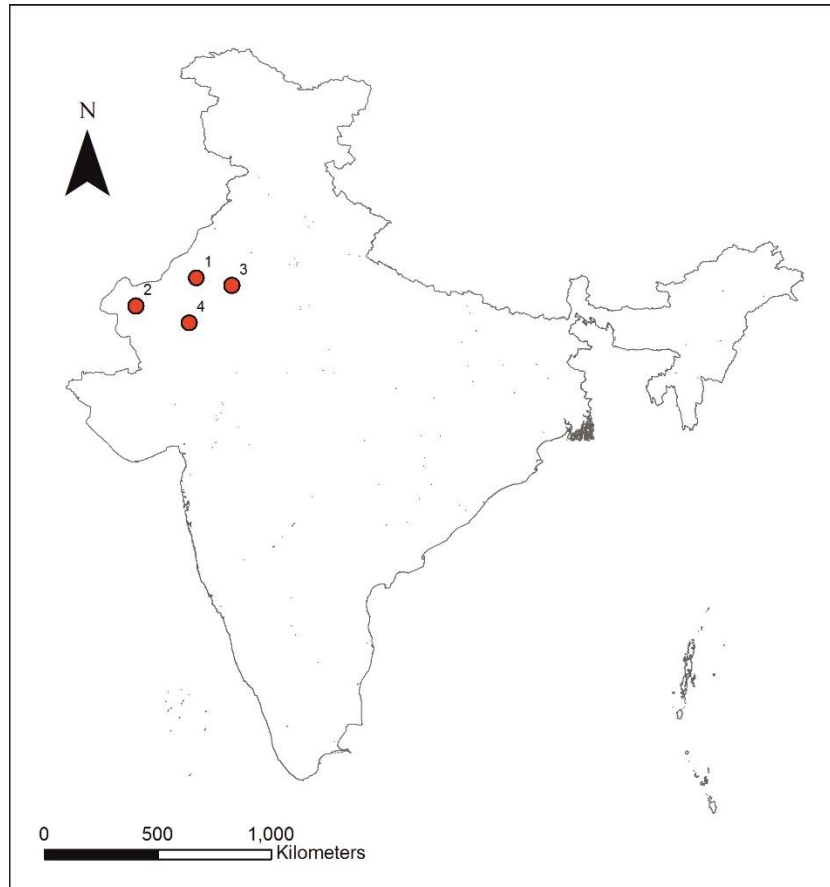


*Figure 3.2: Map of India showing sampling location for aeolian samples. Geographical location of Bikaner, Jaisalmer, Churu and Jodhpur are represented by the numbers 1, 2, 3 and 4 respectively.*

Beach sediments were collected from Kilkee, Co. Clare, Ballycotton, Co. Cork and the Hook Peninsula, Co. Wexford, Ireland (see Fig. 3.1). One sample was collected from each of Kilkee and Ballycotton (B1 and B2). Four samples were collected from around the Hook Peninsula. Sample B3 from Oldtown Bay and B4 from Lumsdin Bay were obtained from the western side of the peninsula. Sample B5 from Sandeel Bay and sample B6 from Woarwoy Bay were taken from the eastern side.

The source for beach sediments are assumed to be mainly the proximal onshore outcrop. In the case of Kilkee beach, these are grey Upper Carboniferous siliciclastic rocks (Pulham, 1989) and red Upper Devonian siliciclastic rocks are the source for sediments present on Ballycotton beach (Pracht et al., 2002), Oldtown Bay and Sandeel Bay (Tietzsch-Tyler and Sleeman, 1994). Whereas, Lower Carboniferous

siliciclastic rocks provide source for beach at Lumsdin Bay and Woarway Bay (Tietzsch-Tyler and Sleeman, 1994).

Fluvial sediments were sampled from the River Lee, Co. Cork, Ireland (see Fig. 3.1). A total of 6 samples were collected at regular intervals starting from Inishcarra, close to Cork Harbour, up to the source of the river at Gougane Barra (F1 to F6 upstream) for a stretch of about 55 km. The average gradient of the river during this length is 0.18 degree. The River Lee flows in an E-W direction through Devonian Old Red Sandstone clastic sedimentary rocks which is the source of sediments it carries (Farrington, 1960).

Environment	Locality	Sample no.	Latitude and Longitude	Source of sediments
Glacial	Myrtleville, Ireland	G1, G2	51°46'59.0"N 8°17'43.2"W	Sedimentary rocks
	Ballycotton, Ireland	G3	51°49'34.7"N 8°00'05.7"W	
	Churchbay, Ireland	G4	51°47'39.9"N 8°16'50.5"W	
Aeolian	Bikaner, India	A1	27°58'50.6"N 73°16'44.9"E	Alluvial deposits
	Jaisalmer, India	A2	26°54'00.7"N 70°54'42.9"E	
	Salasar, India	A3	27°43'25.6"N 74°42'18.7"E	
	Jodhpur, India	A4	26°20'43.8"N 73°01'27.2"E	
Beach	Kilkee, Ireland	B1	52°40'47.5"N 9°39'02.7"W	Sedimentary rocks
	Ballycotton, Ireland	B2	51°49'35.5"N 8°00'03.5"W	
	Hookhead, Ireland	B3,B4,B5,B6	52°09'22.3"N-52°09'39.8"N 6°52'56.6"W- 6°54'01.0"W	
Fluvial	River Lee, Ireland	F1, F2, F3, F4, F5, F6	51°50'02.8"N-51°54'12.9"N 8°37'54.2"W-9°19'52.8"W	Sedimentary rocks

*Table 3.1: Details of samples collected for the study.*



### 3.3 Methodology

The sand samples collected from each site were of the order of 200-500 grams. They were dried in the oven at 40°C for 24 hours to measure their dry weight. Aeolian samples were dry sieved but the other samples were wet sieved and dried once more in the oven. This was done to ensure that the grain particles were free from clay and were not clogged together. Beach samples were further treated with 10% dilute HCL to dissolve any organic and carbonate content present. For each sample, the size fraction of 250um to 500um was selected for consistency.

#### 3.3.1 Image acquisition

Multiple photomicrographs of sets of sand grains from each sample were obtained using a Leica VZ700C microscope (Leica Microsystems, Germany). At a magnification of 140X the field of view (1640µm\*2186µm) was captured in an image with a 1200\*1600-pixel resolution. Each image typically contains 5 to 7 non touching grains without losing grain boundary details (see Fig. 3.3(a)). A total of 200 grains were processed per sample. Transmitted light from below the stage was used with the following settings: - Exposure: 61.4ms; Saturation: 1.3; Gain:1.0x; Gamma: 1.29. The images were processed using Mathematica and included converting the image to binary followed by detection of grain boundaries (see Fig. 3.3(b)).



Figure 3.3: Image acquisition of sand grains. (a) Microphotograph of 6 sand grains captured using transmitted light on a microscope. (b) Processed image identifying individual grains to be used for grain shape measurements.

### 3.3.2 Shape parameters

Shape parameters were computed using code developed by the authors on the Mathematica platform. In this study, improvements to existing parameters such as angularity and irregularity are proposed to improve grain shape characterisation. On the other hand, roundness and circularity, which have been assessed in earlier studies (Wadell, 1932; Riley, 1941; Blott and Pye, 2008; Roussillon et al., 2009) are used without modification. Fractal dimension and a plethora of other geometrical shape parameters are also used here to test their potential application in sedimentology. These parameters are briefly discussed below:

#### 3.3.2.1 Roundness

Roundness of a particle is defined as the average radius of the circles that are fitted to the corners of the grain divided by the radius of the largest inscribed circle of the grain (Wadell, 1932). The expression for roundness ( $r$ ) is:

$$r = \sum_{i=1}^n \frac{r_i}{n R}$$

where  $r_i$  is the radius of curvature of the corners of the grain boundary,  $n$  is number of corners of the grain and  $R$  the radius of the largest inscribed circle. A corner is defined as the region having a radius of curvature less than the radius of the largest inscribed circle. In this paper, a modified form of roundness (Roussillon et al., 2009) is used where the radius of curvature at each boundary point is evaluated instead of at the corners alone (see Fig. 3.4).

#### 3.3.2.2 Circularity

Circularity is a measure of how close the shape of a particle is to a circle (Blott and Pye, 2008; Riley, 1941). It is calculated as:

$$C = \sqrt{\frac{D_i}{D_c}}$$

where,  $D_i$  is the diameter of the largest inscribed circle of the grain and  $D_c$  is diameter of the smallest circumscribing circle of the grain.

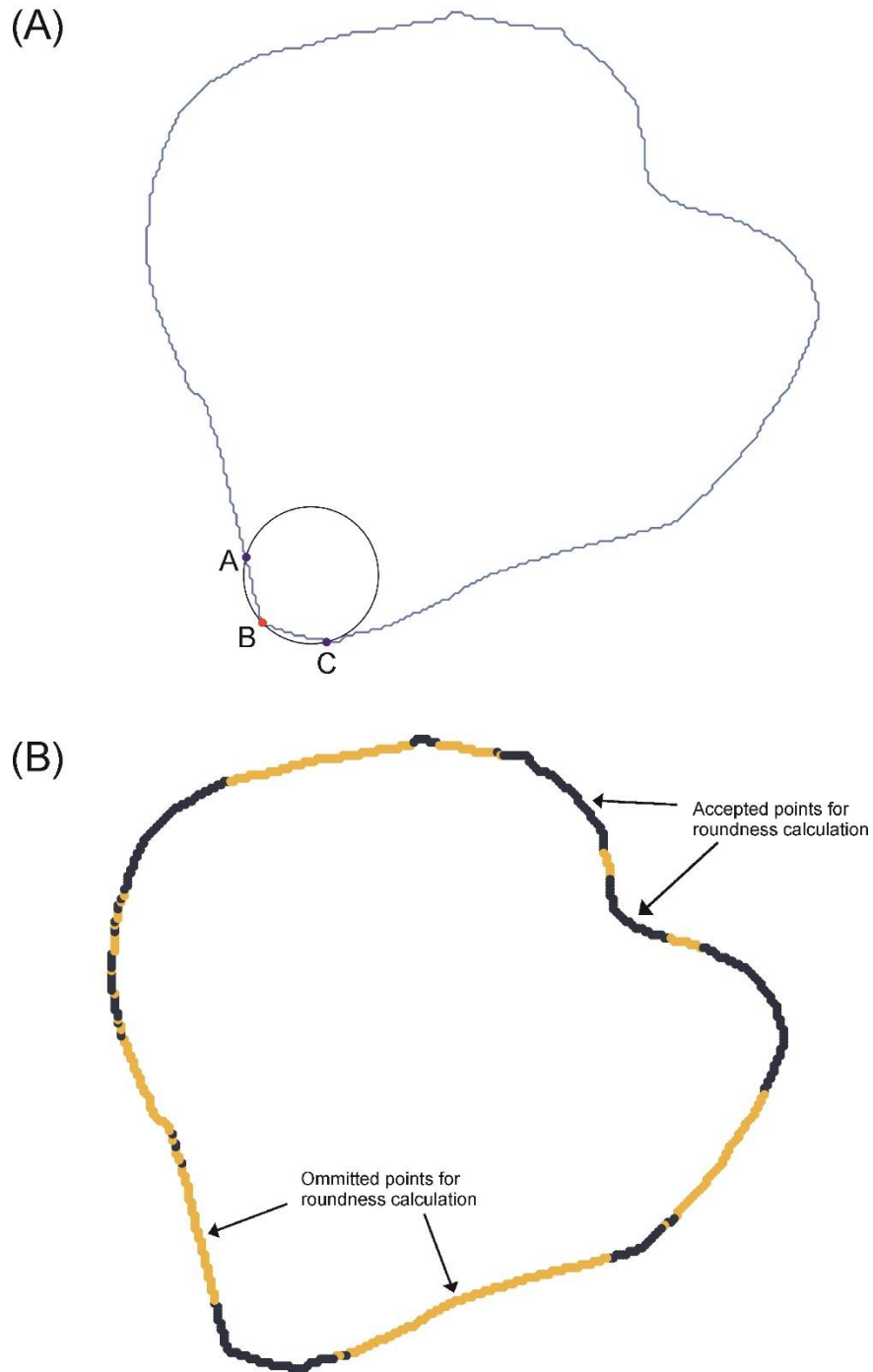


*Figure 3.4: Roundness measurement of a grain using image analysis technique. (a) Radius of curvature at each individual boundary point of the grain is calculated. In this case, radius of curvature is calculated at point B using the circle formed by the three points A, B and C (see Roussillon et al. (2009) for details) (b) All the boundary points having radius of curvature greater than the radius of largest inscribing circle within the grain are identified and omitted. Average of the remaining radius of curvature is averaged to calculate roundness.*

### 3.3.2.3 Angularity

In this paper, a modified version of the angularity measure proposed by Rao et al. (2002) is used. The grain boundary is interpolated as a  $n$ -sided polygon (see Fig. 3.5). Fifty points were used to represent the grain for the purpose of angularity measurement. The difference between consecutive internal angles are calculated and an average of the 5 highest differences in angles is used to represent angularity. This approach was taken because most methods tend to average all angular differences thereby masking the presence of extreme values characteristic of sharp corners.

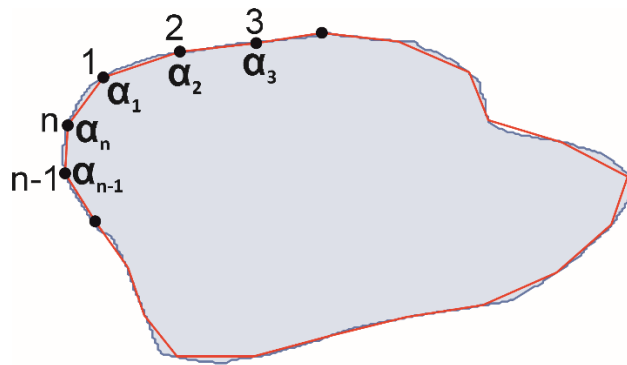


*Figure 3.5: Angularity measurement of a grain by modified Rao et al. (2002). Grain boundary is represented by  $n$  sided polygon. Internal angles  $\alpha_1, \alpha_2, \alpha_3$  until  $\alpha_n$  for the polygon is measured. Differences within the successive internal angles is measured and the five largest differences of internal angles are averaged to calculate angularity.*

### 3.3.2.4 Irregularity

Irregularity is a parameter introduced and described by Blott and Pye (2008). It is a measure to quantify the depth of concavities in the grain boundary with reference to its convex hull. However, here irregularity is measured by comparison with a standard geometrical shape because this is more robust and can quantify both the indentations and projections for the grain boundary. A best fitting ellipse is used here as the standard geometry (Mulchrone and Choudhury, 2004). Irregularity is thus measured as the ratio of the area not in common between the grain and the best fitting ellipse when projected over the grain and the area of ellipse (see Fig. 3.6). Values for irregularity range from 0 to 1 (less to more irregular) inclusive.

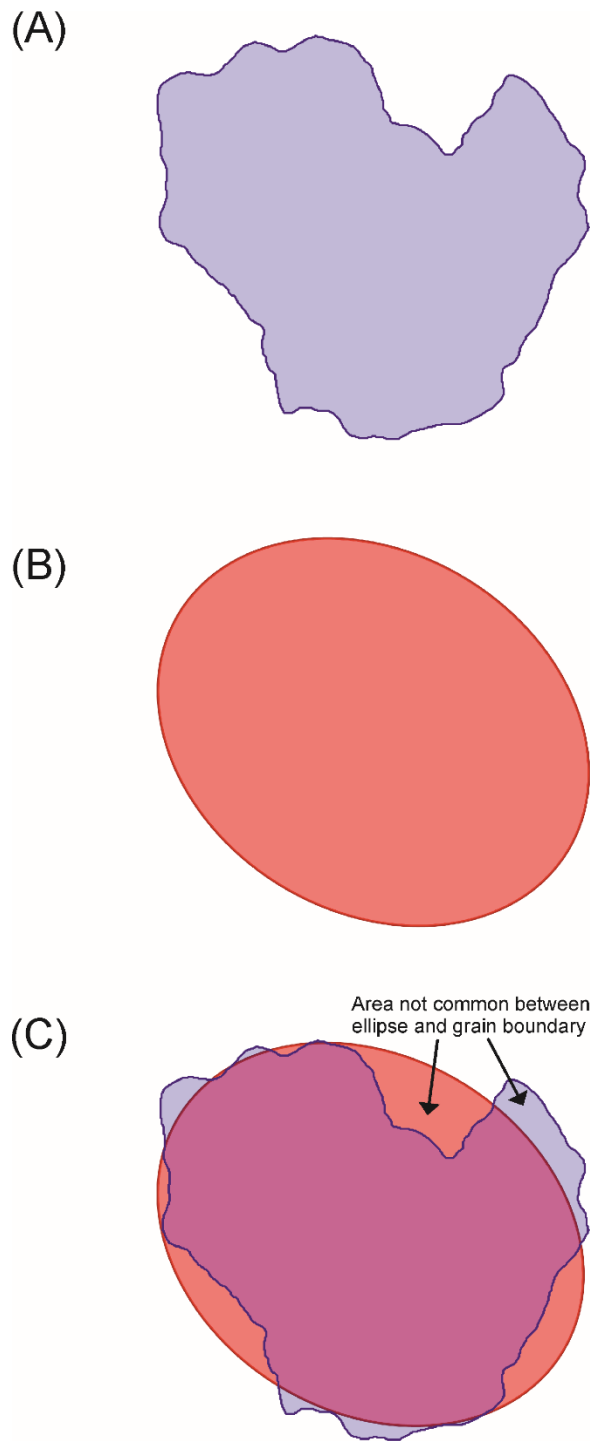


*Figure 3.6: Irregularity measurement of a grain. (a) showing the grain boundary to be measured; (b) the best fit ellipse for the grain; and (c) showing the overlap between the best fit ellipse and the grain. Area not common between best fit ellipse and the grain represents the indentations and projections of the grain with respect to the best fit ellipse. The ratio of this area divided by the area of the best fit ellipse gives the value of irregularity.*

### 3.3.2.5 Fractal Dimension

The concept of fractal dimensions was developed by Mandelbrot (1982) and is used as a measure for boundary roughness. Divider and Box counting methods have been used previously to analyse grain shapes (Orford and Whalley, 1983; Hyslip and Vallejo, 1997). After testing both methods on geometrical shapes, the divider method was empirically found to be more robust in terms of characterising shape and was thus adopted here. In the divider method, the perimeter of the grain boundary is measured using a varying length scale (see Fig. 3.7). The relationship between the measured profile of grain and the length scales gives the fractal dimension as follows:

$$P(\lambda) = K \lambda^{1-D}$$

where  $P(\lambda)$  is the profile of grain measured using  $\lambda$  length scale,  $D$  is the fractal dimension and  $K$  is constant.

### 3.3.2.6 Other parameters

A list of simple shape parameters is described in Table 3.2. and were also calculated for each grain. These parameters are not popular in sedimentology but have been used in civil engineering (Cox and Budhu, 2008). They are included here for completeness and also to evaluate their usefulness in textural analysis.

Shape Parameter	Formula	Description
Aspect Ratio	$L_{\text{major}}/L_{\text{minor}}$	Length of major axis by length of minor axis
Compactness	$\sqrt{4A/\pi}/L_{\text{major}}$	Diameter of circle of equivalent area to grain by length of major axis
ModRatio	$2R_i/\text{Feret}$	Diameter of largest inscribed circle by feret diameter
Solidity	$A/A_{\text{convex}}$	Area by convex area
Convexity	$P_{\text{convex}}/P$	Convex perimeter by perimeter of grain
Rectangularity	$A/A_{\text{BR}}$	Area of grain by area of bounding rectangle

*Table 3.2: Table of simple geometrical parameters used in the study.*

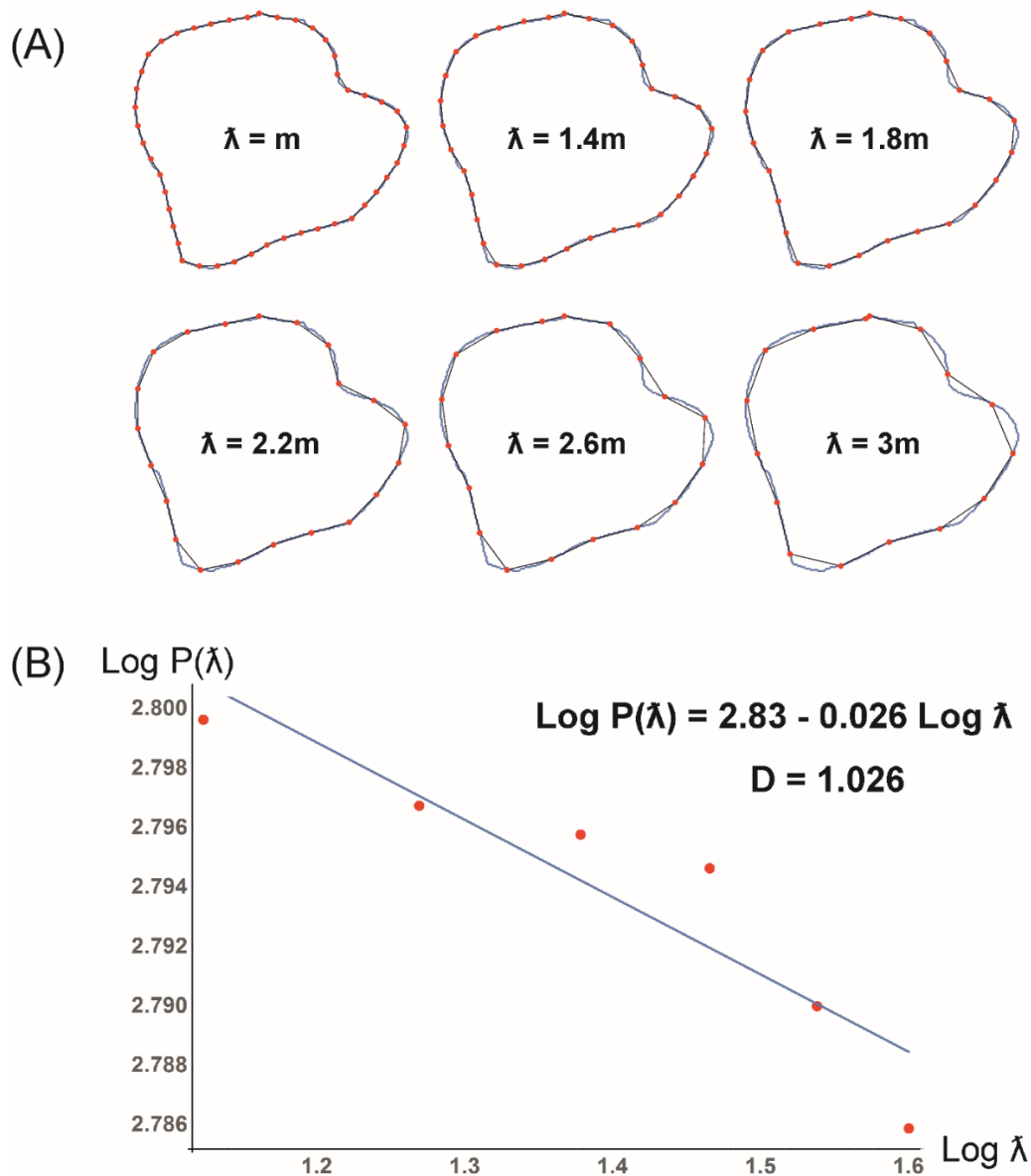


Figure 3.7: Fractal dimension calculation for a grain using the divider method. (a) show the boundary length  $P(\lambda)$  of grain measured using increasing unit length  $\lambda$ . (b) Plot of  $\text{Log } P(\lambda)$  versus  $\text{Log } \lambda$ . Slope of the best fit line over the points gives the fractal dimension of the grain  $D$  as 1.026.

### 3.3.3 Statistical analysis

For each of the 20 samples obtained 200 grains were analysed and 11 shape parameters were calculated for each grain, giving a total of 44,000 data points. To understand this



data a number of standard statistical tools were employed using the 'R' statistical software package. For clarity, a shape parameter distribution refers to the collection of values of a specific shape parameter for an individual sample. Each shape parameter distribution was checked for normality by visually examining each distribution's histogram and corresponding Gaussian curve as well as Q-Q plot and application of the Kolmogorov–Smirnov and Shapiro-Wilk tests. Bivariate plots comparing means of shape parameter distributions for all the samples were plotted. Further, the Pearson correlation matrix was computed for the complete dataset to investigate the correlation between shape parameters.

The Kruskal Wallis test, a non-parametric test, was selected to compare multiple shape parameter distributions within an environment, i.e. it is applied to a group of samples collected within a known individual environment (e.g., roundness for glacial samples G1, G2, G3 and G4). This test compares two or more independent distributions and examines if they originate from the same distribution (Corder and Foreman, 2009; Mangiafico, 2016). If a significant p-value emerges from the Kruskal-Wallis test, then at least one distribution is significantly different to the other distribution(s). The Dunn test is then applied pair-wise to the samples in order to determine where the difference(s) occur and how many difference(s) occur amongst the sample pairs (Mangiafico, 2016). Based on the non-parametric test results, a subset of shape parameters which are useful for ranking of textural maturity can be identified and patterns of textural maturity within environments can be examined.

Hierarchical clustering was applied to summary statistics of samples (mean, standard deviation, 1st quartile, median and 3rd quartile of the shape parameter distribution). k-means clustering is applied to the entire grain dataset, independent of sample, to check if grains form clusters related to sedimentary environment (Hair et al., 2010).

Decision Tree classifiers are used to make predictive models to determine which shape parameters are more or less important in various classification schemes for sediments. Three classifications of sediments used here are 1) based on the individual samples 2) based on the environment type 3) based on the grouping of textural maturity (from hierarchical clustering). The analysis uses a subset of shape parameters identified above for the entire set of grains together with the known subdivision into the three classifications. The entire dataset is randomly divided into a training dataset and a test

dataset (70:30) and a predictive model is constructed using the training dataset. Both the Random Forests (Liaw and Wiener, 2002) and Classification And Regression Tree analysis (CART, David et al., 1998) methods were applied to the training dataset and their respective error was analysed based on their confusion matrix when the predictive model was applied to test data for the three classification schemes.

### 3.4 Results

Apart from a few exceptions in roundness distributions, the majority of shape parameter distributions for different shape parameters are not normally distributed. This is independent of sample and environment. Box-plots for the most important parameters from all the samples are shown in Figure 3.8. Distributions of roundness tend to show reasonable symmetry for all samples (see Fig. 3.8(a)). Angularity, irregularity and fractal distributions are positively skewed for all samples (see Fig. 3.8(c), 3.8(d) and 3.8(e)). On the other hand, circularity, solidity and rectangularity distributions are negatively skewed across all samples (see Fig. 3.8(b), 3.8(f) and 3.8(h)). Distributions of convexity are both positively and negatively skewed (see Fig. 3.8(g)).

A strong linear trend is observed on bivariate plots of shape parameters means for all the samples (see Fig. 3.9). Roundness versus angularity, fractal dimension versus solidity and rectangularity versus convexity are some examples of such a relationship where the order of the samples on this linear trend appears to be uniform. The aeolian samples A1, A2 and A3 consistently appeared on one extreme with highest mean values of roundness, solidity, convexity and rectangularity, and lowest mean values for angularity and fractal dimension. Sample B1, G1 and G4 are part of the other extreme of the spectrum. This coherency in linear progression of mean shape parameter values points to a progression in level of textural maturity from lower in samples B1, G1 and G4 to higher in A1, A2 and A3. The relationship between different shape parameters for all the grains is displayed as a Pearson correlation matrix (see Table 3.3). It shows that aspect ratio, circularity and compactness are highly correlated with each other. Fractal dimension has high to moderate correlation with convexity, roundness, angularity and solidity. Angularity also shows moderate correlation with roundness and solidity. The rest of the shape parameters show very low to moderate correlation with each other.

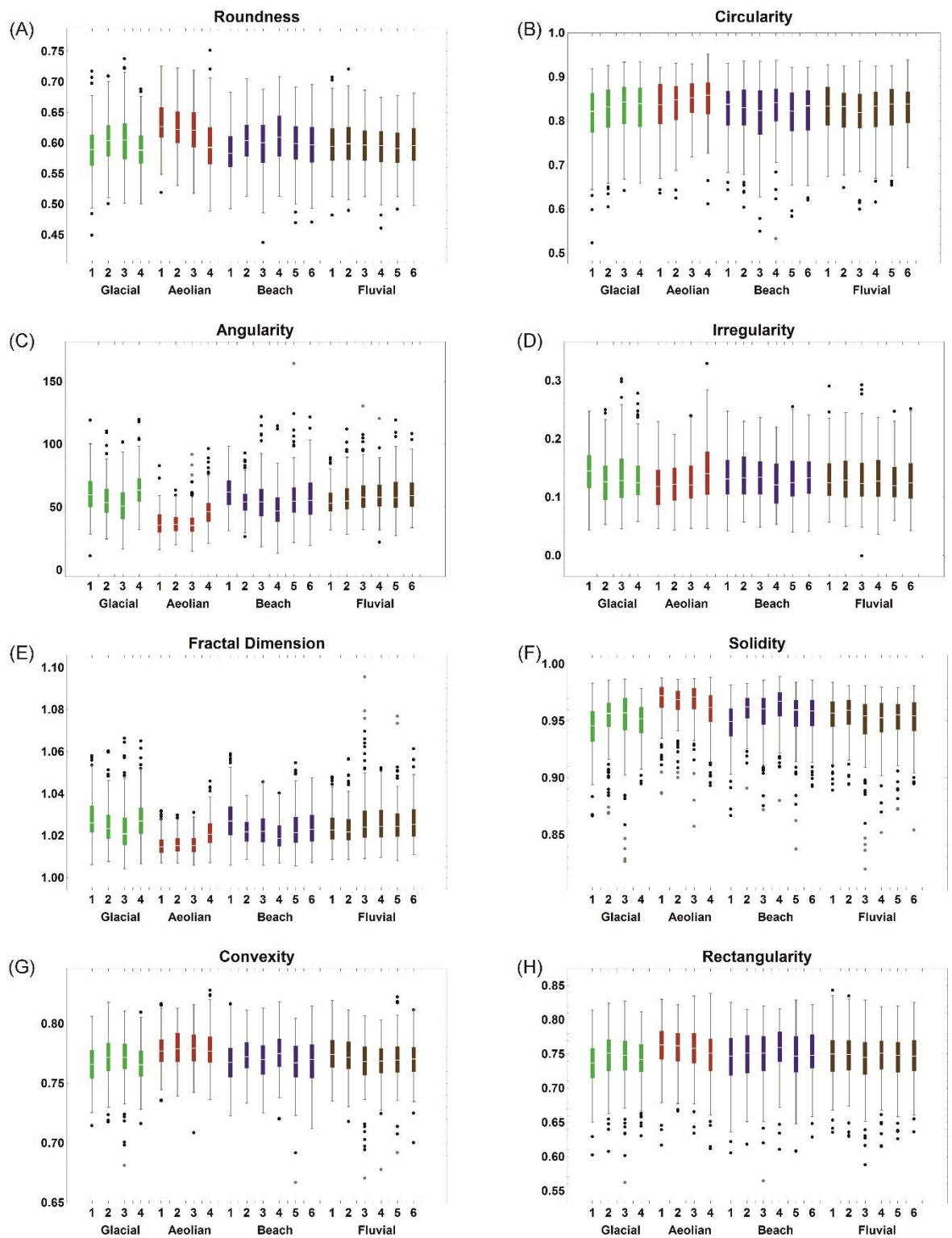


Figure 3.8: Box-plot for all the 20 samples showing the shape parameter distributions of (a) roundness, (b) circularity, (c) angularity, (d) irregularity, (e) fractal dimension, (f) solidity, (g) convexity and (h) rectangularity.

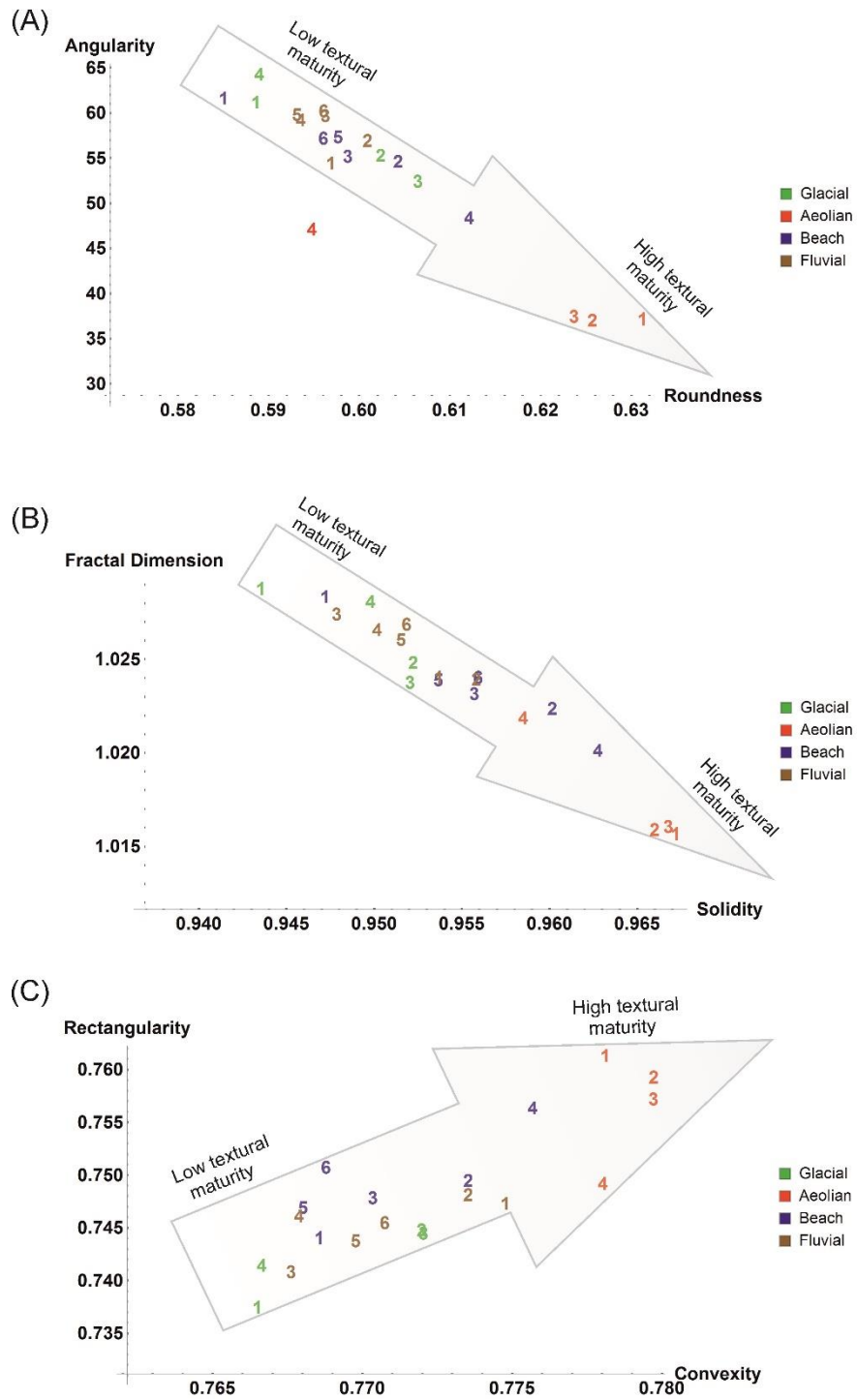


Figure 3.9: Bivariate plots of comparing mean of shape parameters for all the samples. Linear trend in the plots represent the progression of textural maturity for the samples (a) Compares mean roundness of the samples with mean angularity, (b) bivariate plot of mean solidity versus fractal dimension; and (c) comparison between mean convexity and mean rectangularity.

	Round.	Angul.	Fractal	Irreg.	Circul.	AspectR.	Comp.	Convex.	ModR.	Rect.	Solid.
Round.		-0.51	-0.55	-0.26	-0.22	0.30	-0.26	0.35	0.49	0.21	0.43
Angul.	-0.51		0.71	0.17	-0.14	0.05	-0.08	-0.47	-0.19	-0.28	-0.58
Fractal	-0.55	0.71		0.33	-0.20	0.07	-0.11	-0.49	-0.24	-0.38	-0.74
Irreg.	-0.26	0.17	0.33		-0.26	0.05	-0.17	-0.19	-0.24	-0.60	-0.60
Circul.	-0.22	-0.14	-0.20	-0.26		-0.94	0.97	0.13	-0.44	0.34	0.38
AspectR.	0.30	0.05	0.07	0.05	-0.94		-0.97	-0.03	0.47	-0.24	-0.19
Comp.	-0.26	-0.08	-0.11	-0.17	0.97	-0.97		0.06	-0.44	0.33	0.26
Convexity	0.35	-0.44	-0.49	-0.19	0.13	-0.03	0.06		0.09	0.27	0.50
ModR.	0.49	-0.19	-0.24	-0.24	-0.44	0.47	-0.44	0.09		0.17	0.17
Rect.	0.21	-0.28	-0.38	-0.60	0.34	-0.24	0.33	0.27	0.17		0.54
Solid.	0.43	-0.58	-0.74	-0.60	0.38	-0.19	0.26	0.50	0.17	0.54	

Table 3.3: Pearson's correlation matrix showing correlation between shape parameters based on the complete dataset of 4000 grains.

	Glacial	Aeolian	Beach	Fluvial
Roundness	G1,G4 < G2,G3	A4<A1,A2,A3	B1<B3,B5,B6<B2<B4	
Angularity	G1,G4 > G2,G3	A4>A1,A2,A3	B1>B3,B5,B6,B2>B4	
Circularity	G1<G2,G4<G3	A1<A2<A3<A4	B3,B5<B1,B2,B6<B4	
Irregularity	G1>G2,G3,G4	A4>A1,A2,A3		
Fractal	G1,G4 > G2,G3	A4>A1,A2,A3	B1>B3,B5,B6,B2>B4	F4,F6>F3,F5>F1>F2
Aspect Ratio		A1>A2>A3>A4		
Modratio		A1>A2>A3>A4		
Compactness		A1<A2<A3<A4		
Rectangularity	G1<G4 < G2,G3	A4<A3<A1,A2	B1<B5,B6,B3,B2<B4	
Convexity	G1,G4 < G2,G3		B1,B5,B6<B3<B2<B4	F3,F4<F5<F6<F2<F1
Solidity	G1<G4 < G2,G3	A4<A1,A2,A3	B1<B5,B6<B3<B2<B4	F3,F4<F5,F6,F1<F2
	Box Colour			
	Explanation	Kruskal-Wallis test with p-value > 0.05	Kruskal-Wallis test with p-value < 0.05	

Table 3.4: Comparative results for the Kruskal-Wallis and ad hoc Dunn tests performed on the median (the mean produced the same results) of 11 grain shape parameters used to describe grains from four differing depositional environments. The samples are compared within each environment type. Significance of the Kruskal-Wallis test is indicated by the fill colours. Where a significant difference is present, the Dunn test shows how different each sample is to every other sample. Thus, for example, for the roundness distributions in beach samples, the Dunn test indicates

*that, samples B1, B2 and B4 show significant difference compared to each other and the rest of the samples. Samples B3, B5 and B6 do not show significant difference amongst themselves, but they are significantly different than B1, B2 and B4. Mean and median of sample B4 is higher than sample B2, which is higher than the samples in group {B3, B4, B5}. Sample B1 shows the lowest mean and median value.*

Results obtained for both the Kruskal-Wallis and the post hoc Dunn test are summarised in Table 3.4. There is a demonstrable pattern for variation of textural maturity that emerges between the samples within a sedimentary environment. In glacial samples, the sample pair {G2, G3} has textural maturity greater than the pair {G1, G4}. Samples A1, A2 and A3 show similar textural maturity, greater than sample A4, in the aeolian environment. For beach samples, B4 depicts the highest and B1 indicates the lowest textural maturity, whereas the fluvial samples all have similar textural maturity. Circularity, aspect ratio, modratio and compactness do not conform to the textural maturity pattern within the sedimentary environment. Hence, they are discarded from further analysis.

Amongst the glacial samples, the Kruskal-Wallis test indicates significant differences ( $p < 0.05$ ) for roundness, angularity, circularity, irregularity, fractal dimension, rectangularity, convexity and solidity distributions. However, aspect ratio, modratio and compactness show non-significant difference ( $p > 0.05$ ). The Dunn test indicates a non-significant difference for the pairs {G1, G4} and {G2, G3} in terms of roundness, angularity, fractal dimension and convexity distributions. The pair {G1, G4} has lower values for the mean and median values for roundness and convexity compared to the pair {G2, G3}. For angularity and fractal dimension the mean and median for pair {G1, G4} is higher than that for {G2, G3}.

For aeolian samples, only convexity demonstrates a non-significant difference across all samples. For roundness, angularity, irregularity, fractal dimension and solidity, sample A4 is significantly different to the other three samples. A4 shows lower mean and median values for roundness and solidity compared to the rest of the samples (A1, A2 and A3). A4 has a higher mean and median for distributions of angularity, irregularity and fractal dimension compared to other aeolian samples.

There is a non-significant difference amongst beach samples for irregularity, aspect ratio, mod ratio and compactness distributions. The sample B1 and B4 are significantly different to each other and to the rest of beach samples for roundness, angularity, fractal dimension, rectangularity and solidity distributions. The mean and median of sample B1 is lowest and that of sample B4 is highest for roundness, rectangularity and solidity. On the other hand, sample B1 exhibits the highest and sample B4 has the lowest mean and median values for angularity and fractal dimension. The sample pair {B5, B6} show non-significant difference for roundness, angularity, fractal dimension, rectangularity, convexity and solidity distributions.

The Kruskal-Wallis test indicates non-significant difference amongst fluvial samples for roundness, angularity, circularity, irregularity, aspect ratio, modratio, compactness and rectangularity distributions. There is no clear pattern for the rest of the shape parameter distributions.

A hierarchical clustering dendrogram based on the sample-level data is shown in Figure 3.10. To avoid confusion, clusters established using this analysis are termed groups and the term cluster is reserved for k-means clustering analysis below. Overall three main groups of samples are established with this analysis. Aeolian samples A1, A2 and A3 form group 1 which is clearly distinct from all other samples. Samples A4, B4, G3, B3, G2 and B2 make up group 2 and samples G1, B1, F3, G4, F6, F4, F5, B5, B6, F1 and F2 comprise group 3.

Hierarchical clustering established the presence of three groups, thus three clusters form the basis for the k-means clustering analysis. This technique matches grains from each environment to their respective clusters. Glacial grains fall under cluster 1 with 27.5 % grains, 51 % grains in cluster 2 and 21.75 % in cluster 3. Aeolian grains are divided in clusters with 73.5% grains in cluster 1, 24.25 % grains in cluster 2 and 2.5 % grains in cluster 3. Beach grains are clustered with 31.42 % grains in cluster 1, 49.67 % grains in cluster 2 and 18.92 % grains in cluster 3. Grains from fluvial environment are classified with 20.75 % grains in cluster 1, 56.25 % grains in cluster 2 and 23 % grains in cluster 3. As is best practice k-means clustering analysis was also performed assuming more than 3 clusters, however, this did not improve the analysis.

## Heirarchical Clustering

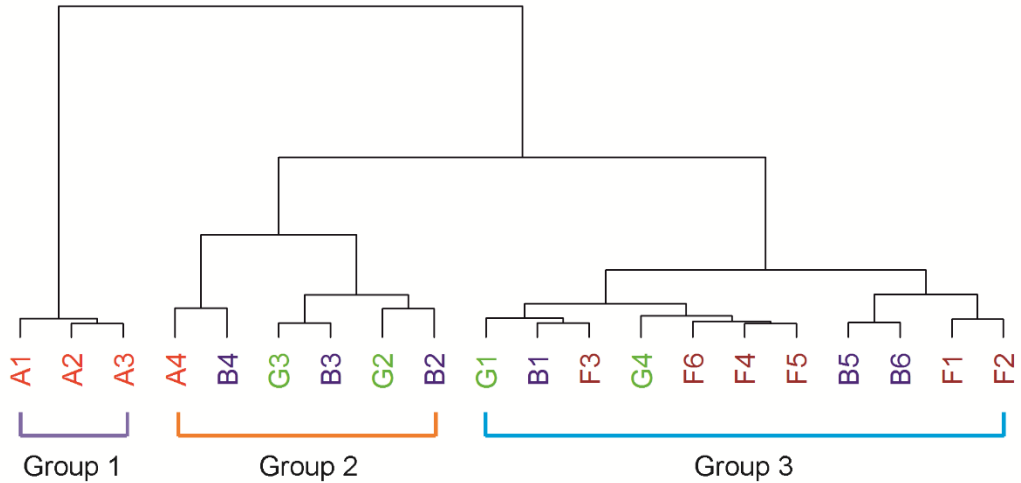


*Figure 3.10: Dendrogram showing proximal relationship amongst the samples based on Hierarchical analysis using summary statistics value of roundness, angularity, irregularity, fractal dimension, convexity, rectangularity and solidity.*

Decision Tree classifiers are applied for roundness, angularity, irregularity, fractal dimension, rectangularity, convexity and solidity. Predictive models for CART and Random Forests are developed with the three known classification schemes: individual sample group (20 samples), environment (4 environments) and grouping based on hierarchical clustering (3 groups). When the predictive model based on individual sample classification is applied to test data, CART and Random Forests give an error of 92.61 % and 92.12 % respectively. The error for CART and Random Forests predictive model based on the environmental classification is 62.07 % and 62.41 % respectively. On the basis of textural maturity grouping classification, the CART and Random Forests methods give an error of 41.58 % and 42.66 % respectively. According to the Random Forests method applied for textural maturity grouping, the usefulness of a parameter to classify a grain into its given group of textural maturity is denoted by ‘parameter importance’ and summarised in Table 3.5. Angularity and fractal dimension are the two most important parameters identified for textural maturity classification.



<b>Shape Parameter</b>	<b>Importance</b>
Angularity	470.56
Fractal Dimension	321.06
Solidity	291.89
Irregularity	268.68
Roundness	254.46
Convexity	251.26
Rectangularity	237.94

*Table 3.5: Importance of each shape parameter in categorising a grain to a given sample, independent of its environment, given by Random Forests method. Higher values indicate greater importance.*

### 3.5 Discussion

In this study, a definite pattern of textural maturity has emerged for shape distributions of roundness, angularity, irregularity, fractal dimension, rectangularity, convexity and solidity (Table 3.4). Increasing textural maturity is correlated with increasing roundness, rectangularity, convexity and solidity. Also angularity, fractal dimension and irregularity tend to decrease with increasing textural maturity for the samples studied. Circularity and aspect ratio are correlated with each other by virtue of their definition and are independent of textural maturity. Aspect ratio has already been shown by Campaña et al. (2016) to be unrelated to maturity and this study confirms this conclusion. Despite not being found useful for textural analysis of samples in this study, shape parameters such as circularity, aspect ratio, mod ratio and compactness may still be of some use in other textural analysis contexts.

Textural maturity trends have been studied within a single environment. Parameter distributions for roundness, angularity, fractal dimension, irregularity, rectangularity, convexity and solidity are used to study these trends. In the glacial environment G2

and G3 clearly show higher textural maturity than G1 and G4. Aeolian samples A1, A2 and A3 from Bikaner, Jaisalmer and Salasar show remarkably high textural maturity and low variation within each sample for the shape parameters. However, sample A4 from Jodhpur differs significantly from the other samples and presents a population distribution consistent with intermediate textural maturity. In the beach environment sample B4 from Lumsdin Bay exhibits the highest textural maturity and is significantly different to the rest of the beach samples. Sample B2 from Ballycotton shows the next highest textural maturity after B4. Shape parameter distributions indicate that sample B3 is significantly different to B4. Sample B5 and B6 are texturally similar and fairly immature. B1 from Kilkee show the lowest textural maturity. Fluvial samples from the River Lee comprise highly variable grain parameter distributions but there is little difference between the samples. These samples are homogenous as a group but individually quite mixed in terms of shape parameters and it is difficult to rank them in terms of textural maturity.

The entire dataset indicates that shape parameters (i.e. roundness, angularity, fractal dimension, irregularity, rectangularity, convexity and solidity) can collectively indicate the textural maturity of a sample. However, significant within-environment variation is observed and suggests that a direct link to environment may not always be valid.

A key part of this study is to rank the effectiveness of each shape parameter in characterising grains between samples, environment and textural maturity grouping using machine learning algorithms. A predictive model by Random Forests method suggests that angularity and fractal dimension are the most important parameter for assigning a grain into its' respective textural maturity classification scheme. This is an unexpected result and indicates that angularity and fractal dimension may be extremely useful for textural analysis of sedimentary grains. Fractal dimension, which is the second most important parameter according to Random Forests, has not been employed much since the study of Cox and Budhu, (2008). A recent study by Sochan et al. (2015) tried to apply fractal dimension but did not obtain satisfying results. This suggests that a standardised methodology and availability of a comprehensive shape measurement toolset for the wider sedimentology community is needed.

There has been a long debate in sedimentology about the usefulness of grain shape in identifying sedimentary environments. A recent study (Suzuki et al., 2015) used 15 grains per sample and applied a combination of elliptical Fourier descriptor and principal component analysis in an attempt to discriminate sedimentary environment based on grain shape. Their data and analysis resulted in clean, well-separated clusters by environment. In the current study, a multivariate approach is used to group samples with similar shape properties into clusters by employing hierarchical analysis. In contrast to Suzuki et al. (2015) three major groups of samples are present for four environments and two of the groups are mixed by environment. However, the grouping established here, corresponds directly with levels of textural maturity and a pattern can be seen in a bivariate plot of mean angularity versus mean fractal dimension (see Fig. 3.11). Despite the parameters being defined very differently, mean angularity and fractal dimension are strongly correlated (Pearson coefficient = 0.94). Such strong collinearity suggests that mean angularity and mean fractal dimension are good indicators of textural maturity. This analysis supports the use of shape parameters for textural analysis but recommends caution when attempting to distinguish sedimentary environment.

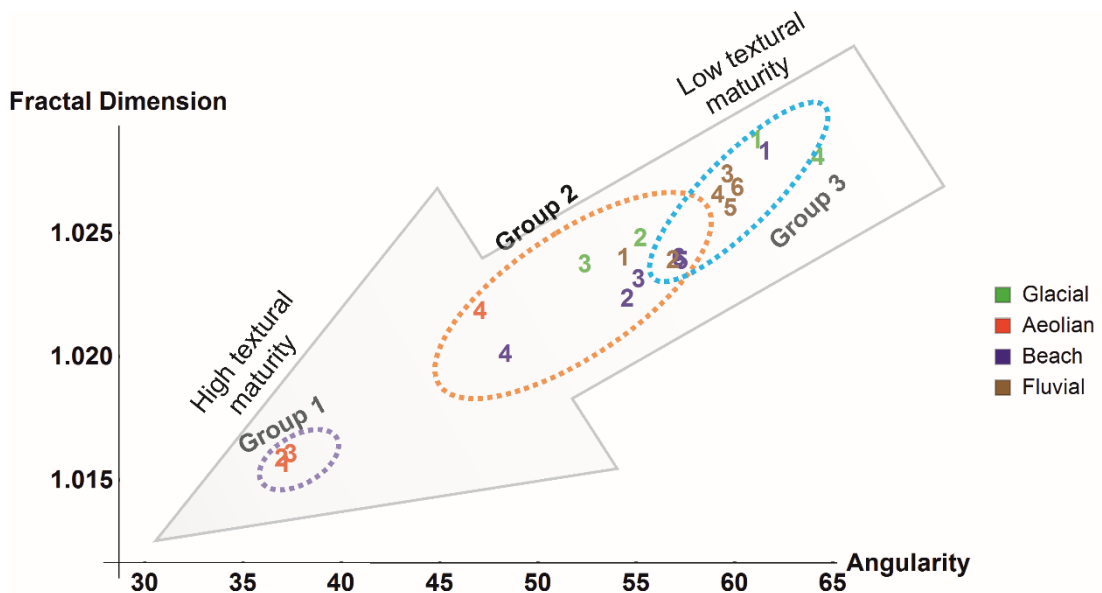


Figure 3.11: Bivariate plot for mean angularity versus mean fractal dimension of all the samples. Three group of samples relates to the groups formed in hierarchical clustering (refer to Fig. 3.10).

Furthermore, application of k-means clearly demonstrates that glacial, fluvial and beach environments display similar distribution of grains into the three clusters, however aeolian samples are quite distinct. This implies that there is large overlap within the grains of glacial, beach and fluvial environments. Cluster 1 represents the most mature grains, cluster 2 intermediate maturity and cluster 3 with the least mature. It is reasonable to expect a mixing of textural maturities in a given sample from glacial, beach and fluvial environments. This goes a long way towards explaining why fully objective population-based shape parameter data tends to overlap between different sedimentary environments. It would be surprising if distinct, easily separated clusters were discovered.

This study emphasises the usefulness of quantitative analysis over qualitative analysis of grain shapes. Traditionally overlooked shape parameter such as fractal dimension is demonstrated here to be of importance in textural analysis. On the other hand, circularity, which has been much discussed and used in sedimentology, as well as aspect ratio, mod ratio and compactness do not conform to the textural patterns observed collectively in other shape parameters. Non-conventional shape parameters such as convexity, solidity and rectangularity are found useful along with the traditional shape parameters such as roundness, angularity and irregularity. Using a large population of grains from different depositional environments, it has been demonstrated that quantitative shape analysis is useful in ranking textural maturity of different samples. However, it is not possible to confidently discriminate between depositional environments on the basis of large populations of grain shapes.

The methodology described in this paper to compare, group and in some cases, rank the samples on the basis of grain shape data is rapid and computationally inexpensive. It can be extended to any population of clastic particles with size greater than 250 microns. This is because the smaller sized grains may not experience abrasion and grinding action during transport (Rogers et al., 1963). The methods presented here can be applied to increase the speed of shape parameter analysis, extract statistically significant data sets and improve accuracy of results. This will be of use to researchers in sedimentology wishing to use the approach developed. For example, recent suitable studies include efforts to clarify the history of basin evolution and identify stratigraphic discontinuities (Kleesment, 2009) or elucidate palaeoenvironmental conditions (Dadd and Foley, 2016).

### 3.6 Conclusion

The data presented in this study clearly illustrates that shape parameters for populations of grains are characterised by significantly variable distributions. The data strongly suggests that quantitative shape parameter analysis is a useful approach to textural analysis of a large population of grains despite large variation within data populations. Roundness, angularity, irregularity, fractal dimension, convexity, solidity and rectangularity are identified to be the useful shape parameters for textural characterisation of sediments. A solid relationship between textural maturity of samples and shape parameter distributions is evident. Angularity and fractal dimension are found to be the most important shape parameters for categorising a single sediment grain into its textural maturity classification. The data establishes that a pair of samples that exhibit similar shape parameter characteristics is more likely to be due similar textural maturity rather than depositional environment type. Furthermore, there is overlap between shape parameter characteristics of grains from different sedimentary environments, and this suggests that it is not always possible to rigorously discriminate between sedimentary environments on the basis of textural analysis alone. However, many of the aeolian samples form a distinct group but this is readily explained by their high levels of textural maturity.

Further shape parameter distribution studies on many more samples from a variety of known sedimentary environments are required to build on and tease out the relationship between shape parameters, textural maturity and environment established here. The results reported should bring a fresh impetus to grain shape analysis as a tool for petrographic studies. This study demonstrates the merit of quantitative population-based shape parameter based analysis of texture and indicates that it may play a key role in characterising both loose and consolidated sediments.

### 3.7 Acknowledgement

The authors are grateful to the reviewers Simon Blott and Andrzej Bieganowski, the Chief Editor Nigel Mountney and the Associate Editor Subhasish Dey for suggestions that have significantly improved the original manuscript. Ed Jarvis and Anil Kumawat are thanked for their help in sample collection. This project is funded by the Irish Shelf Petroleum Studies Group (ISPSG) of the Irish Petroleum Infrastructure Programme

(PIP) Group 4. The ISPSG comprises: Atlantic Petroleum (Ireland) Ltd, Cairn Energy Plc, Chrysaor E&P Ireland Ltd, Chevron North Sea Limited, ENI Ireland BV, Europa Oil & Gas (Holdings) plc, ExxonMobil E&P Ireland (Offshore) Ltd., Kosmos Energy LLC, Maersk Oil North Sea UK Ltd, Petroleum Affairs Division of the Department of Communications, Energy and Natural Resources, Providence Resources plc, Repsol Exploración SA, San Leon Energy Plc, Serica Energy Plc, Shell E&P Ireland Ltd, Sosina Exploration Ltd, Statoil (UK) Ltd, Tullow Oil Plc and Woodside Energy (Ireland) Pty Ltd.

### 3.8 References

**Al-Rousan, T., Masad, E., Tutumluer, E. and Pan, T.** (2007) Evaluation of image analysis techniques for quantifying aggregate shape characteristics. *Construction and Building Materials*, **21**, 978-990.

**Barrett, P.J.** (1980) The shape of rock particles, a critical review. *Sedimentology*, **27**, 291-303.

**Blatt, H.** (1992) *Sedimentary Petrology*. W. H. Freeman and Company, New York, 514 pp.

**Blatt, H., Middleton, G.V. and Murray, R.C.** (1972) *Origin of sedimentary rocks*. Prentice-Hall Inc., New Jersey, 634 pp.

**Blott, P.J. and Pye, K.** (2008) Particle shape: a review and new methods of characterization and classification. *Sedimentology*, **55**, 31-63.

**Boggs, S.** (2009) *Petrology of sedimentary rocks*. Cambridge University Press, Cambridge, UK, 600 pp.

**Campaña, I., Benito-Calvo, A., Pérez-González, A., Bermúdez de Castro, J.M. and Carbonell, E.** (2016) Assessing automated image analysis of sand grain shape to identify sedimentary facies, Gran Dolina archaeological site (Burgos, Spain). *Sedimentary Geology*, **346**, 72-83.

**Corder, G.W. and Foreman, D.I.** (2009) Comparing More than Two Unrelated Samples: The Kruskal–Wallis H-Test. In: *Nonparametric Statistics for Non-Statisticians*, pp. 99-121. John Wiley & Sons, Inc., New Jersey, USA.

**Cox, M.R. and Budhu, M.** (2008) A practical approach to grain shape quantification. *Engineering Geology*, **96**, 1-16.

- Dadd, K. and Foley, K.** (2016) A shape and compositional analysis of ice-rafted debris in cores from IODP Expedition 323 in the Bering Sea. *Deep-Sea Research II*, **125**, 191-201.
- David, G.T.D., Mallick, B.K. and Adrian, F.M.S.** (1998) A Bayesian CART Algorithm. *Biometrika*, **85**, 363-377.
- Eamer, J.B.R., Shugar, D.H., Walker, I.J., Lian, O.B. and Neudorf, C.M.** (2017) Distinguishing Depositional Setting For Sandy Deposits In Coastal Landscapes Using Grain Shape. *Journal of Sedimentary Research*, **87**, 1-11.
- Ehlers, E.G. and Blatt, H.** (1982) *Petrology: Igneous, Sedimentary, and Metamorphic*. W. H. Freeman and Company, San Francisco, 732 pp.
- Farrington, A.** (1960) The Lee Basin: Part 2, the Drainage Pattern. *Proceedings of Royal Irish Academy*, **61**, 233-253.
- Folk, R.L.** (1951) Stages of textural maturity in sedimentary rocks. *Journal of Sedimentary Research*, **21**, 127-130.
- Friedman, G.M. and Sanders, J.E.** (1978) *Principles of Sedimentology*. John Wiley & Sons, New York, 792 pp.
- Hair, J.F., Anderson, R.E., Babin, B.J. and Black, W.C.** (2010) *Multivariate data analysis: A global perspective*. Pearson Upper Saddle River, NJ, 785 pp.
- Hyslip, J.P. and Vallejo, L.E.** (1997) Fractal analysis of the roughness and size distribution of granular materials. *Engineering Geology*, **48**, 231-244.
- Kleesment, A.** (2009) Roundness and surface features of quartz grains in Middle Devonian deposits of the East Baltic and their palaeogeographical implications. *Estonian Journal of Earth Science*, **58**, 71-84.
- Krumbein, W.C.** (1941) Measurement and geological significance of shape and roundness of sedimentary particles. *Journal of Sedimentary Research*, **11**, 64-72.
- Liaw, A. and Wiener, M.** (2002) Classification and regression by randomForest. *R news*, **2**, 18-22.
- Lira, C. and Pina, P.** (2009) Automated grain shape measurements applied to beach sands. *Journal of Coastal Research Special Issue*, **56**, 1527-1531.
- Mandelbrot, B.B.** (1982) *The Fractal Geometry of Nature*. W. H. Freeman and Company, New York, 468 pp.
- Mangiafico, S.** (2016) Summary and Analysis of Extension Program Evaluation in R, version 1.6.19. . Available: [rcompanion.org/documents/RCompanionBioStatistics.pdf](http://rcompanion.org/documents/RCompanionBioStatistics.pdf).(January 2016).

- Mulchrone, K.F. and Choudhury, K.R.** (2004) Fitting an ellipse to an arbitrary shape: implications for strain analysis. *Journal of Structural Geology*, **26**, 143-153.
- Ó Cofaigh, C., Telfer, M.W., Bailey, R.M. and Evans, D.J.A.** (2012) Late Pleistocene chronostratigraphy and ice sheet limits, southern Ireland. *Quaternary Science Reviews*, **44**, 160-179.
- Orford, J.D. and Whalley, W.B.** (1983) The use of the fractal dimension to quantify the morphology of irregular-shaped particles. *Sedimentology*, **30**, 655-668.
- Pant, R.** (1993) Spread of loess and march of desert in western India. *Current Science*, **64**, 841-847.
- Pettijohn, F.J.** (1957) *Sedimentary Rocks*. Harper and Row Publishers, New York, 718 pp.
- Pettijohn, F.J., Potter, P. and Siever, R.** (1972) *Sand and Sandstone*. Springer-Verlag, New York, 618 pp.
- Powers, M.C.** (1953) A new roundness scale for sedimentary particles. *Journal of Sedimentary Research*, **23**, 117-119.
- Pracht, M., Sleeman, A., Wright, G. and Cox, W.** (2002) A Geological Description of West Cork and Adjacent parts of Kerry to Accompany the Bedrock Geology 1: 100,000 Scale Map Series, Sheet 24, West Cork, with Contributions by G. *With accompanying contributions by G. Wright (Groundwater) and W. Cox (Minerals)*, Geological Survey of Ireland, 79pp.
- Pulham, A.J.** (1989) Controls on internal structure and architecture of sandstone bodies within Upper Carboniferous fluvial-dominated deltas, County Clare, western Ireland. *Geological Society, London, Special Publications*, **41**, 179-203.
- Rao, C., Tutumluer, E. and Kim, I.T.** (2002) Quantification of Coarse Aggregate Angularity Based on Image Analysis. *Journal of the Transportation Research Board*, **1787**, 117-124.
- Reineck, H. and Singh, I.** (1975) *Depositional Sedimentary Environments*. Springer—Verlag, New York, 439 pp.
- Riley, N.A.** (1941) Projection sphericity. *Journal of Sedimentary Research*, **11**, 94-97.
- Rogers, J.J., Krueger, W.C. and Krog, M.** (1963) Sizes of naturally abraded materials. *Journal of Sedimentary Research*, **33**, 628-632.



- Roussillon, T., Piegay, H., Sivignon, I., Tougne, L. and Lavigne, F.** (2009) Automatic computation of pebble roundness using digital imagery and discrete geometry. *Computers and Geosciences*, **35**, 1992-2000.
- Singhvi, A. and Kar, A.** (2004) The aeolian sedimentation record of the Thar Desert. *Proceedings of the Indian Academy of Sciences - Earth and Planetary Sciences*, **113**, 371-401.
- Sochan, A., Zieliński, P. and Bieganski, A.** (2015) Selection of shape parameters that differentiate sand grains, based on the automatic analysis of two-dimensional images. *Sedimentary Geology*, **327**, 14-20.
- Suzuki, K., Fujiwara, H. and Ohta, T.** (2015) The evaluation of macroscopic and microscopic textures of sand grains using elliptic Fourier and principal component analysis: Implications for the discrimination of sedimentary environments. *Sedimentology*, **62**, 1184-1197.
- Tafesse, S., Robison Fernlund, J.M., Sun, W. and Bergholm, F.** (2013) Evaluation of image analysis methods used for quantification of particle angularity. *Sedimentology*, **60**, 1100-1110.
- Takashimizu, Y. and Iiyoshi, M.** (2016) New parameter of roundness R: circularity corrected by aspect ratio. *Progress in Earth and Planetary Science*, **3**, 1-16.
- Tietzsch-Tyler, D. and Sleeman, A.** (1994) A geological description of South Wexford and adjoining parts of Waterford, Kilkenny and Carlow to accompany the Bedrock Geology 1: 100,000 scale map series, Sheet 23, South Wexford. *Geological Survey of Ireland, Dublin*, 62 pp.
- Tucker, M.** (2001) *Sedimentary petrology: an introduction to the origin of sedimentary rocks*. Blackwell Science Ltd., Oxford, 262 pp.
- Wadell, H.** (1932) Volume, Shape, and Roundness of Rock Particles. *Journal of Geology*, **40**, 443-451.

## **4 A new approach to grain shape quantification using Inverse Radius of Curvature (IRC)**

*Mohit Tunwal<sup>1)2)</sup>\*, Kieran F. Mulchrone<sup>2)</sup> and Patrick A. Meere<sup>1)</sup>*

(Current status: ready for submission)

*<sup>1)</sup> School of Biological, Earth and Environmental Sciences, University College Cork, Distillery Fields, North Mall, Cork, Ireland*

*<sup>2)</sup> School of Mathematical Sciences, University College Cork, Western Gateway Building, Western Road, Cork, Ireland*

### **Abstract**

Sediment grain shape analysis provides important information regarding transport and deposition history. Recent developments in image analysis tools have led to renewed focus on developing quantitative shape measurement methods. However, most of the presently available methods commonly suffer from at least two shortcomings: (1) the parameter value is difficult to relate to physical attributes and (2) particles, which are visually distinct, are not easily distinguished. This contribution seeks to address these issues by introducing the Inverse Radius of Curvature (IRC) plot which can be used to identify grain corners and measure their sharpness. Using the IRC plot, four shape parameters are proposed: number of corners, cumulative angularity, sharpest corner and straight fraction. This methodology is applied to 4000 sand grains collected from glacial, aeolian, beach and fluvial environments. The results demonstrate that the four new shape parameters can be collectively used to quantitatively describe grain shape which correlates closely with visual perceptions. The proposed technique improves upon the use of subjective, qualitative comparison charts and furthermore opens the way for visually relevant automated shape analysis.

\*Corresponding author: [mohittunwal@gmail.com](mailto:mohittunwal@gmail.com)

Keywords: Grain shape, texture, roundness, image analysis, angularity, shape measurement, Inverse Radius of Curvature

## 4.1 Introduction

The shape of a grain can provide vital information regarding its transportation and depositional history (Pettijohn et al., 1972). Roundness of a grain, measured using average radius of curvature of the corners (Wadell, 1932), is the most widely used shape parameter by sedimentologists (Barrett, 1980; Blott and Pye, 2008). In the past, several researchers have also suggested using the sharpest corner for measuring particle roundness (Cailleux, 1947; Dobkins and Folk, 1970; Kuenen, 1956; Swan, 1974; Wentworth, 1919). Features of corners have been attributed a physical significance in understanding recent transport conditions (Barrett, 1980). However, these and many other shape parameters have (at least up until recently) the drawback of tedious and time consuming manual shape measurements. This effort is often mitigated by the utilisation of visual comparison charts (Krumbein, 1941; Powers, 1953). However, resulting qualitative shape measurements are subjective in nature and data are often irreproducible (Blatt, 1992; Blatt et al., 1972).

With recent rapid advancements in computational power and algorithms, image analysis techniques for measuring grain shape have been proposed (Roussillon et al., 2009; Sochan et al., 2015; Suzuki et al., 2015; Tafesse et al., 2013). However, this development exposes difficulties in interpreting numerical data concerning grain shape. Some measures are mathematically sophisticated and are difficult to relate to physical grain attributes. For example, Fourier analysis methods introduce as many numerical descriptors as desired, and the relationship of each one to grain shape is not often clear (Schwarcz and Shane, 1969; Suzuki et al., 2015; Thomas et al., 1995). Additionally, shape parameters struggle to reflect differences that are visually obvious. For example, according to Tafesse et al. (2013) angularity parameters are not “capable of separating particles with similar angularities, such particles that are rounded from those that are sub-rounded or sub-angular, in a manner that would yield comparable results to that of visual classification”. A possible explanation is that the current shape parameters tend to measure the form of the grain (i.e., macro features like circularity (Takashimizu and Iiyoshi, 2016)) and/or surface irregularities in addition to the

angularity (Al-Rousan et al., 2007; Tafesse et al., 2013). For example, Figure 4.1 shows a range of grain shapes with same numerical value of roundness calculated using the method of Roussillon et al. (2009). However, they are visually quite distinct.

Recent studies have indicated that there is a need for shape measurement algorithms/techniques that identify grain corners and measures their sharpness (Tafesse et al., 2013) and, in particular, detect the sharpest corner (Roussillon et al., 2009). In addition, in a review study, it was recommended that more than one shape parameter ought to be used in order to discriminate between particles (Blott and Pye, 2008).

The broad objective of this work is to present an approach for shape quantification that relates directly to the visual perception of grain shape in 2-Dimensions. Thus, this paper aims to:

- 1) propose a methodology to identify the corners of a particle and measure their sharpness.
- 2) present a suite of new shape parameters using this methodology that can collectively represent a grain boundary in a visually meaningful way.
- 3) assess the shape quantification methodology proposed here by application to a natural dataset
- 4) demonstrate the relationship between the proposed parameters and the visual perception of grain shape.

In this paper, a new grain shape quantification methodology using the inverse radius of curvature is proposed and a set of shape parameters are suggested. The method is applied to loose sediment samples from a variety of sedimentary environments. This approach provides an avenue for utilising image analysis tools to quantify shape such that parameters can be related to visual examination.

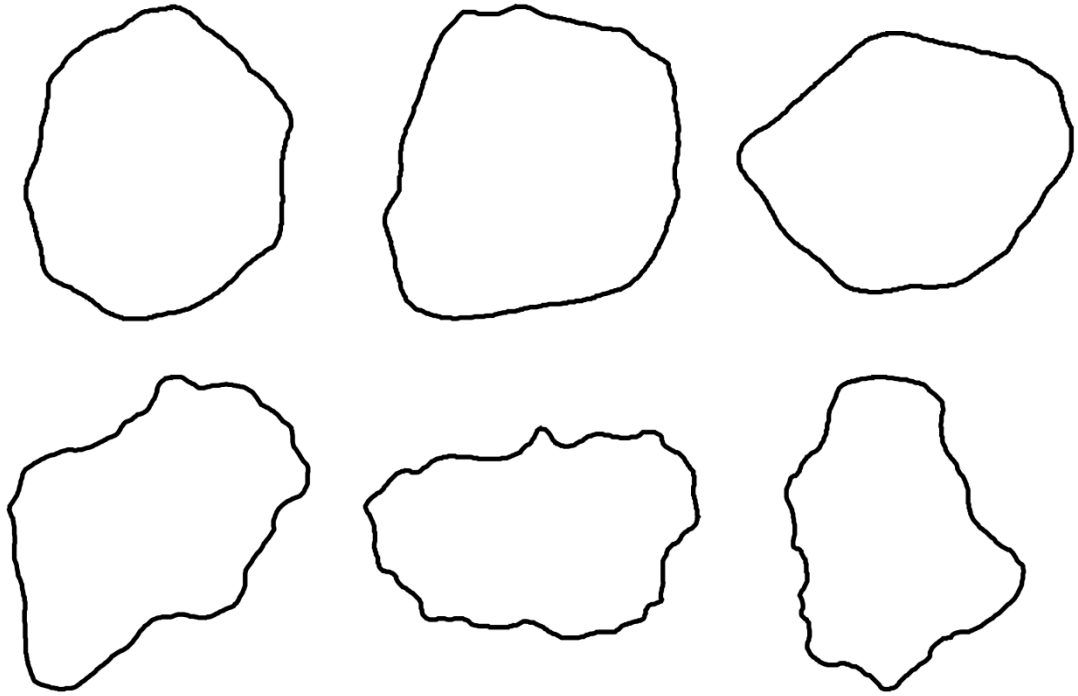


*Figure 4.1: Example of grain boundaries with roundness value of 0.60 calculated using Roussillon et al. (2009) method.*

## 4.2 Shape quantification method

Most standard shape parameters are independent of the size of the grain. However, the grain shape quantification technique described in this paper is based on the measurement of radius of curvature at each point on the grain boundary. Therefore, the absolute size of the grain has implications for calculations based on the radius of curvature. Thus, it is necessary to scale grain boundaries such that their sizes are equivalent.

### 4.2.1 Scaling of grain boundary

To scale a set of grains, one feature must be selected and made equal for all grains. Some possible features are: 1) radius of the equivalent disc area, 2) average distance from centre of grain to the boundary, 3) perimeter of grain boundary or 4) caliper length of grain boundary. All four possibilities have been tested empirically and caliper length is found to give the best results in the sense that all grains are of a comparable size.

Caliper length ( $c$ ), which is defined to be the radius of the smallest circumscribing circle, is measured for the grain boundary. Next, the scaling factor ( $sf$ ) is defined as  $2/c$  which ensures that the radius of the smallest circumscribing circle for all the scaled grains is of unit length. Each grain is translated such that its centroid coincides with the origin and then the  $x$  and  $y$  coordinates of the grain boundary points are scaled by  $sf$ . Finally, a fixed number of boundary points (510 was optimal in this study) are regularly sampled along the grain boundary. Thus, scaling of the grain boundary guarantees that the size of all grain boundaries are comparable and the number of boundary points is constant.

#### 4.2.2 Inverse Radius of Curvature (IRC) plot

After scaling the grain boundary, the radius of curvature at each boundary point is calculated using two nearby points (Roussillon et al., 2009). In detail, the radius of curvature at point  $i$  is the radius of the circle that fits the boundary points  $i-j$ ,  $i$  and  $i+j$ . The ratio of number of boundary points to  $j$  was found to be optimal at 30 for the amplitude of IRC representing the corners. Thus  $j$  for this study was taken as 17, other possible set of values for number of boundary points and  $j$  can be  $\{600,20\}$ ,  $\{450,15\}$  and likewise. Next, the Inverse Radius of Curvature (IRC) is calculated as  $1/(\text{radius of curvature})$  for all the boundary points (see Fig. 4.2). IRC is a better measure than the radius of curvature because in a natural grain, straight sections are expected and thus the radius of curvature tends to infinity which is difficult to handle in a practical sense. Furthermore, on a graph showing IRC versus grain boundary point (see Fig. 2), boundary points, indexed from 1 to 510, correspond directly to position 0 and 1 along the  $x$ -axis i.e. the axis is normalised to unit length. A bilateral filter (Paris et al., 2009) is applied to smoothen the plot. In Fig. 4.3 raw data is plotted in thin blue line and smoothened data is plotted in thick red line. The smoothing simply removes high frequency noise from the data. It is argued here that the IRC plot is an important tool from which information regarding the shape of a grain can be obtained quantitatively.

#### 4.2.3 Corner identification

Peaks in the IRC plot are associated with corners in the grain. The sharper the corner the higher the peak. Additionally, lower peaks may signify either wide corners or the jaggedness of the grain boundary. Therefore, it is important to identify and pick out

peaks corresponding to significant corner regions of the grain. This is achieved using a simple threshold ( $t$ ) given by:

$$t = Q_{20} + b$$

where  $Q_{20}$  is the 20th quantile of the smoothed dataset (i.e. after applying the bilateral filter) and  $b$  is a constant (an appropriate value for  $b$  was found to be 2). Sections of the IRC curve above this threshold, represented by dotted green line on the IRC plots (Fig. 4.3), are selected as peaks. It is worth noting that in case of a perfectly round boundary, e.g. a circle, no corners will be identified.

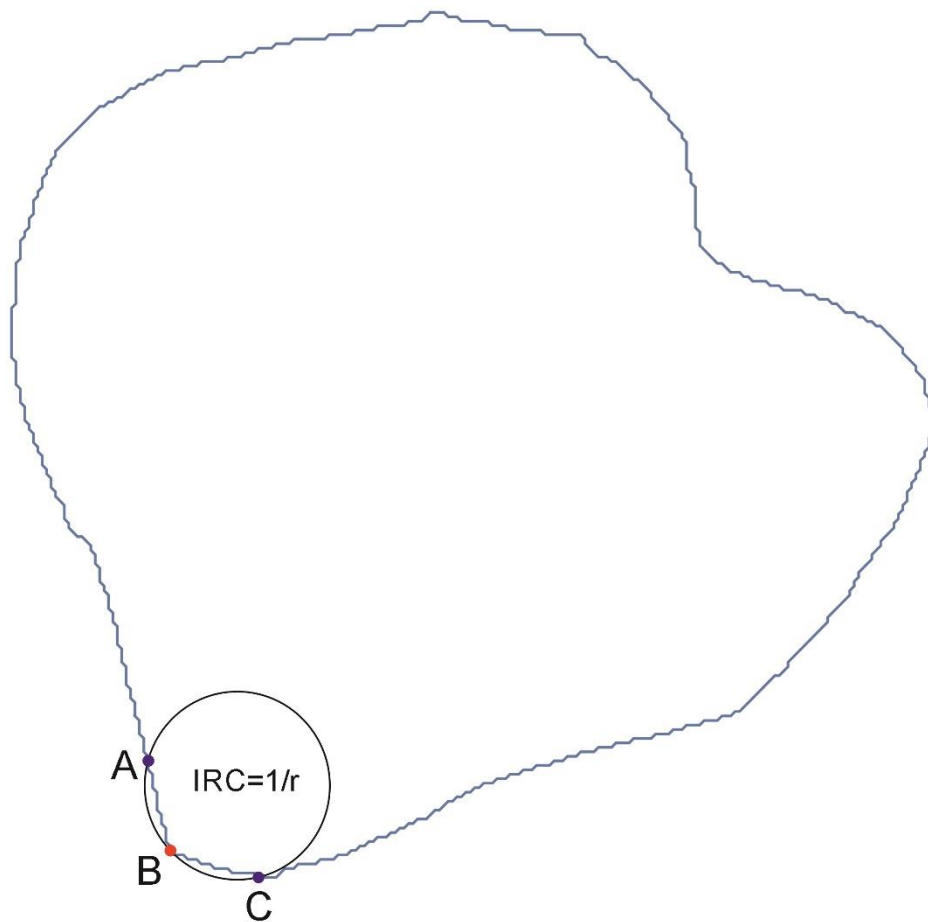


*Figure 4.2: Inverse Radius of curvature (IRC) at each individual boundary point of the grain is calculated. In this case, radius of curvature is calculated at point B using the circle formed by the three points A, B and C. IRC value at point B is 1 divided by the radius of curvature.*

## 4.2.4 Shape Parameters for grain characterisation using the IRC

### 4.2.4.1 Number of Corners ( $v$ )

The number of peaks lying above the threshold on the IRC plot are counted as the number of corners in the grain boundary. A higher  $v$  value represents a grain boundary typically consisting of large number of indentations and projections (see Fig. 4.3 (c)). Whereas, a lower  $v$  value represents fewer corners in the grain boundary (see Fig. 4.3 (a)). A very rounded grain can be expected to show no above-threshold peaks in its IRC plot (see Fig. 4.3 (d)).

### 4.2.4.2 Cumulative Angularity ( $\alpha$ )

The individual height of a peak is related to the sharpness of the corner in the grain. The sum of all peak heights (IRC values) identified gives the  $\alpha$  value for the grain boundary. This value represents the overall level of angular features in a grain. A high  $\alpha$  value denotes either a few very sharp corners or large numbers of less-sharp corners or a mixture of both (see Fig. 4.3 (b) and 4.3 (c)).

### 4.2.4.3 Sharpest Corner ( $\eta$ )

IRC value of the highest peak in the IRC plot represents the acuteness of the sharpest corner in the grain boundary (see Fig. 4.3 (b)). This information along with number of peaks and cumulative angularity gives an overall quantitative representation of the corners. A grain which has no above-threshold peak is assigned zero value for the highest peak.

### 4.2.4.4 Straight Fraction ( $\phi$ )

Low values on the IRC plot typically correspond to straight parts of the grain boundary (see Fig. 4.3 (a)). The percentage of boundary points with IRC value below 0.5 (threshold represented by dotted brown line on IRC plot in Fig. 4.3) gives the fraction of the grain boundary which is relatively straight. This is important information which is not identified by existing shape parameters. It is important to note that both high and low  $\phi$  values can occur in both round and angular grains.



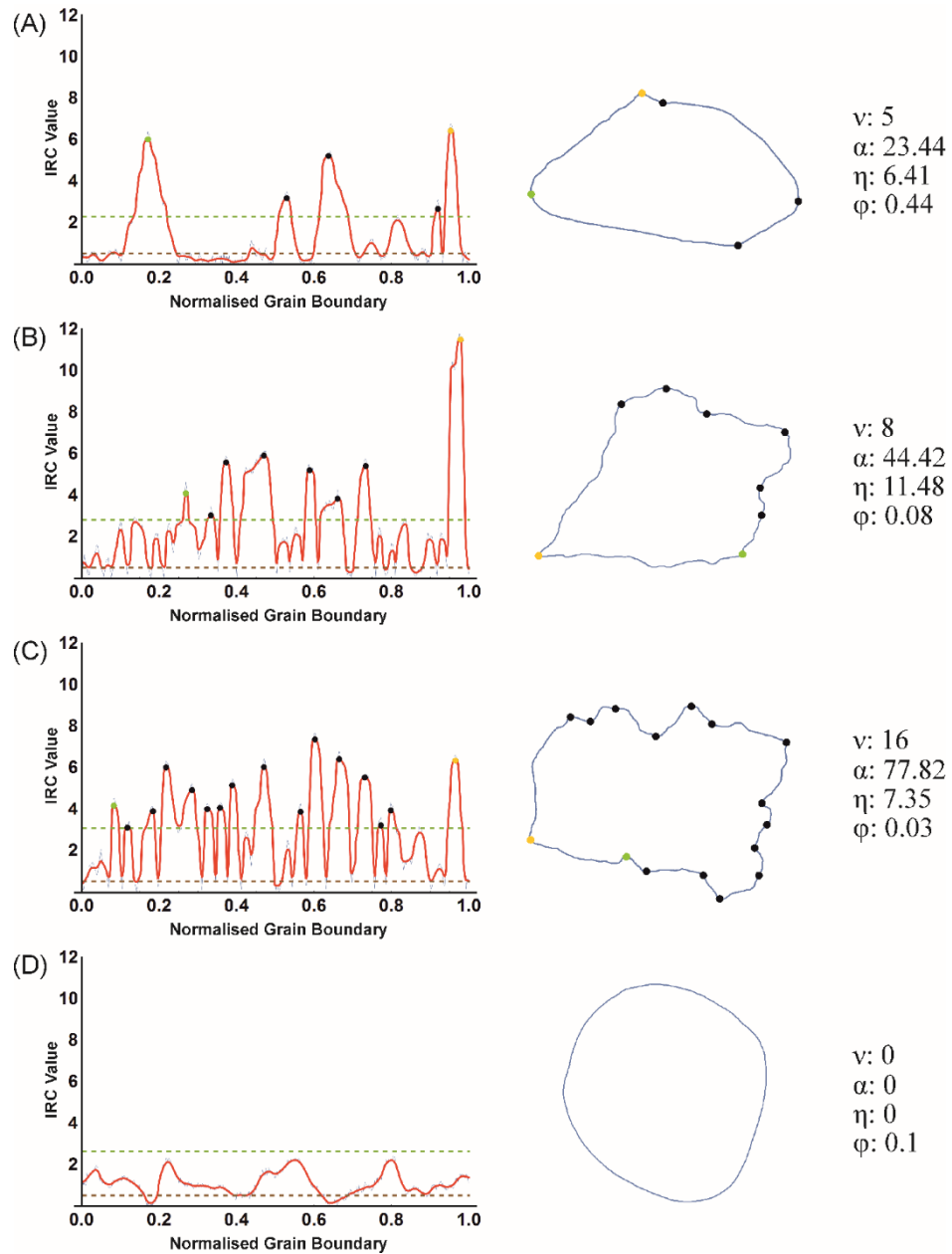


Figure 4.3: IRC plot on the left with corresponding grain boundaries on the right. Original data of IRC values is denoted by thin blue line. Smoothened IRC values are represented by thick red line. Lower threshold for peak identification is shown by dotted green line. Peaks identified here corresponds to corners of particle boundary. Dotted brown line represents the upper threshold for straight fraction regions. (a) grain with 5 identified peaks in the IRC plot with 0.44  $\phi$  value (b) grain with  $\eta$  value of 11.48, 8  $v$  value and 44.42  $\alpha$  value (c) grain with 16  $v$  value and 77.82  $\alpha$  value (d) perfectly rounded grain without any identified peak.

### 4.3 Application to natural grains

A total of 20 loose sediment samples were collected from glacial, aeolian, beach and fluvial environments (see Table 4.1). For the same depositional environment, multiple samples were collected to analyse the grain shape variation within environments as well as between them. Grains in all samples had a sedimentary provenance. This reduces potential influences of source lithology variation on observed grain shapes.

#### 4.3.1 Sampling Sites

Glacial samples derived from Devonian-Carboniferous siliciclastic source rocks were sampled from the Late Pleistocene deposits of the Last Glacial Maximum (LGM) in County Cork, Ireland (Ó Cofaigh et al., 2012). These samples were collected from glacial tills at Myrtleville (G1 and G2), Ballycotton (G3) and Church Bay (G4).

Aeolian samples were collected at Bikaner (A1), Jaisalmer (A2), Salasar (A3) and Jodhpur (A4) in the Thar Desert, India. Unconsolidated alluvial sediments, subsequently reworked by aeolian processes, are thought to be source of the aeolian sand (Pant, 1993). Dune types present at Jodhpur and Jaisalmer are sand sheets, at Salasar there are parabolic dunes and at Bikaner there are transverse dunes (Singhvi and Kar, 2004).

Beach samples were sampled from Kilkee, Co. Clare, Ballycotton, Co. Cork and Hook Peninsula, Co. Wexford, Ireland. Onshore outcrops in proximity of the beach are assumed to be the source lithology of the sediments. These are grey Upper Carboniferous siliciclastic rocks in the case sample B1 from Kilkee beach (Pulham, 1989). Red Upper Devonian siliciclastic rocks provide the source material for sample B2 from Ballycotton Bay (Pracht et al., 2002) and samples B3 and B5 from the Hook Peninsula (Tietzsch-Tyler and Sleeman, 1994). Whereas, Lower Carboniferous rocks are believed to be the source rocks for beach samples B4 and B6 from the Hook Peninsula.

A total of 6 fluvial samples were gathered from the River Lee, Co. Cork, Ireland. They were collected at regular intervals starting from Inishcarra to the source of the river at Gougane Barra (F1 to F6 upstream) for a 55 Km. stretch. The River Lee flows in an W-E direction with an average gradient of  $0.18^\circ$ . Upper Devonian Old Red Sandstone clastic sedimentary bedrock provides the source of the sediments (Farrington, 1960).

Environment	Locality	Sample no.	Latitude and Longitude	Source of sediments
Glacial	Myrtleville, Ireland	G1, G2	51°46'59.0"N 8°17'43.2"W	Sedimentary rocks
	Ballycotton, Ireland	G3	51°49'34.7"N 8°00'05.7"W	
	Churchbay, Ireland	G4	51°47'39.9"N 8°16'50.5"W	
Aeolian	Bikaner, India	A1	27°58'50.6"N 73°16'44.9"E	Alluvial deposits
	Jaisalmer, India	A2	26°54'00.7"N 70°54'42.9"E	
	Salasar, India	A3	27°43'25.6"N 74°42'18.7"E	
	Jodhpur, India	A4	26°20'43.8"N 73°01'27.2"E	
Beach	Kilkee, Ireland	B1	52°40'47.5"N 9°39'02.7"W	Sedimentary rocks
	Ballycotton, Ireland	B2	51°49'35.5"N 8°00'03.5"W	
	Hookhead, Ireland	B3,B4,B5,B6	52°09'22.3"N-52°09'39.8"N 6°52'56.6"W- 6°54'01.0"W	
Fluvial	River Lee, Ireland	F1, F2, F3, F4, F5, F6	51°50'02.8"N-51°54'12.9"N 8°37'54.2"W-9°19'52.8"W	Sedimentary rocks

*Table 4.1: Details of samples collected for the study.*

#### 4.3.2 Sample treatment and Image acquisition

The sediment samples were dried in an oven at 40°C for 24 hours to measure their dry weight. The samples were then wet sieved and washed to make sure that they were deflocculated and free from clay particles. The samples were further treated with 10% dilute HCL to dissolve any organic content present. The size fraction of 250-500 um was chosen for each sample for consistency.

Images of loose sediments were taken in a set of 5-7 non touching grains per photomicrograph using a Leica VZ700C microscope (Leica Microsystems, Germany). High resolution images of 1200\*1600 pixel were taken at magnification of 140X for a field of view (1640um\*2186um) assuring that high level of boundary details of the sand grains were captured. The sand grains were settled on the microscopic stage to

allow their projection along the longest and intermediate axis to be imaged using a transmitted light source beneath the stage. Overall 200 grains per sample were imaged. Each photomicrograph was processed using code developed in Mathematica by the authors to binarize them and identify boundaries of the individual grains (see Tunwal et al., in print).

## 4.4 Results

### 4.4.1 Assessment of Shape Parameters

The Pearson Correlation matrix depicting the relationship between the four shape parameters amongst themselves as well as a list of various other shape parameters (Cox and Budhu, 2008; Hyslip and Vallejo, 1997; Rao et al., 2002; Riley, 1941; Roussillon et al., 2009; Tunwal et al., in print) is shown in Table 4.2. There is a positive correlation between  $v$ ,  $\eta$  and  $\alpha$ , with  $v$  and  $\alpha$  being highly correlated (0.94) and  $\eta$  showing moderate relationship with  $v$  and  $\alpha$  (0.44 and 0.63 respectively). In contrast,  $\phi$  is negatively correlated with  $v$ ,  $\eta$  and  $\alpha$ , with low to moderate relationship (-0.39, -0.19 and -0.42 respectively).  $v$ ,  $\eta$  and  $\alpha$  show moderate to strong relationship with roundness, angularity, fractal dimension, convexity, rectangularity and solidity. On the other hand,  $\phi$  is poorly to moderately related with the rest of the shape parameters.

Bivariate plots showing the distribution of the entire grain dataset for combinations of shape parameters are presented in Figure 4.4. These plots visually illustrate the variations of shape parameters for natural grains. Numbered grain boundary images are inset around the bivariate plots and are referenced on the plots for visual appraisal. Individual grains are referred to by a concatenation of figure number, subplot letter and grain number. For example, 4a1 refers to the grain shown in box 1 of Figure 4.4 (a).

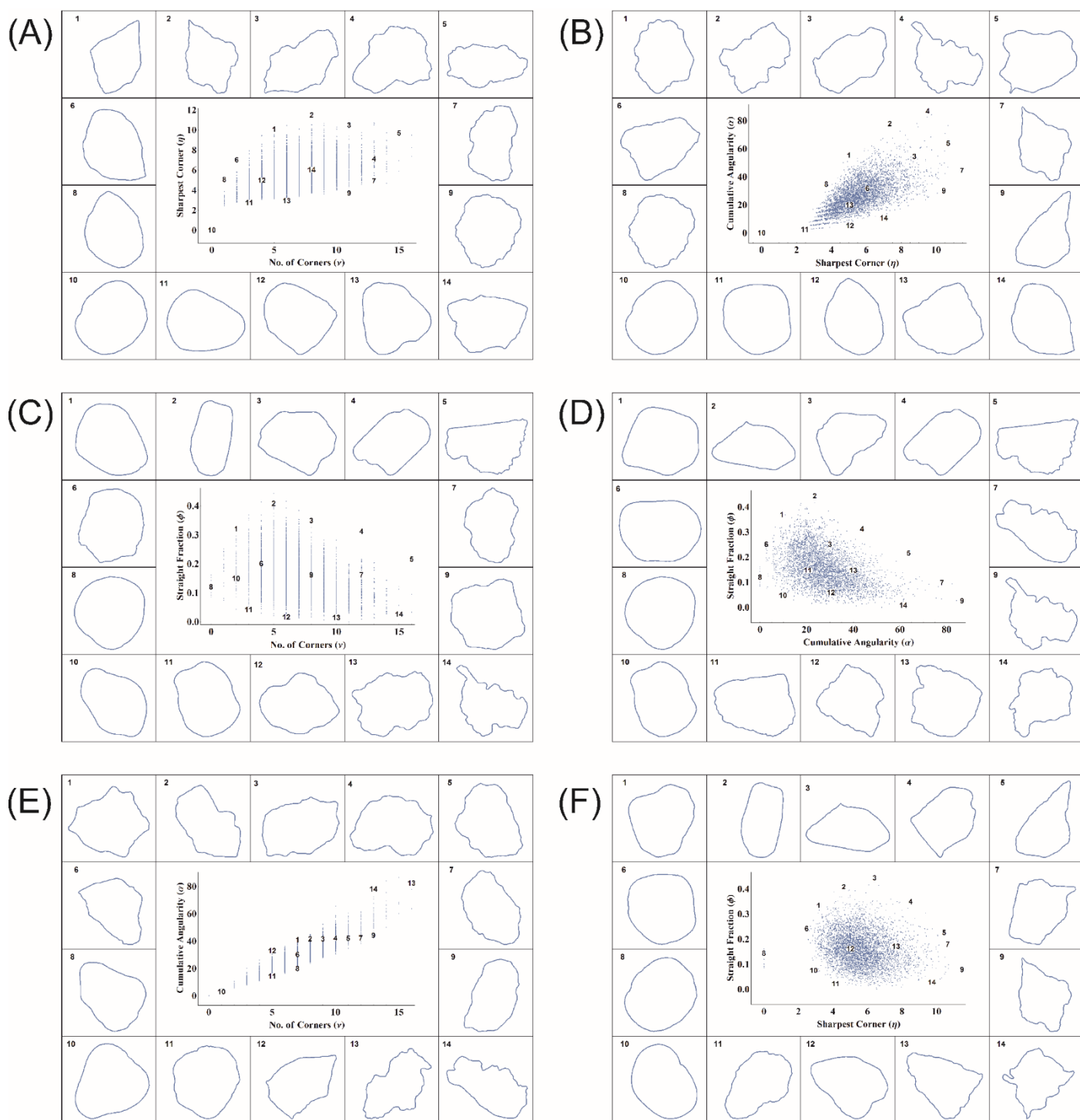


Figure 4.4: Bivariate plots showing distribution of the 4000 grains in (a)  $\eta$ - $\nu$  plot (b)  $\alpha$ - $\eta$  plot (c)  $\phi$ - $\nu$  plot (d)  $\phi$ - $\alpha$  plot (e)  $\alpha$ - $\nu$  plot and (f)  $\phi$ - $\eta$  plot. The 14 insets around each subplot display boundary of grain which is represented by the inset number on the bivariate plot.

The visual comparison of grain boundaries by varying shape parameters values is now considered:

#### 4.4.1.1 $\eta$ vs $v$ plot

High  $\eta$  value grains are represented by 4a1, 4a2, 4a3 and 4a5 in increasing order of their  $v$  values. The sharpest corner present in these grain boundaries are comparable, whereas, the number of corners increases from 5 in 4a1 to 15 in 4a5. Grain boundaries 4a8 and 4a6 corresponds to the intermediate IRC value for  $\eta$  along with low  $v$  value (1 and 2 peaks respectively). While 4a11, 4a13 and 4a9 exemplifies grain boundaries with low  $\eta$  value with an increasing  $v$  value.

#### 4.4.1.2 $\alpha$ vs $\eta$ plot

Grains 4b9 and 4b7 show high  $\eta$  value (10.44 and 11.48 respectively) with low to moderate  $\alpha$  value (30.00 and 44.42 respectively). On the other hand, grains 4b8 and 4b1 have comparable  $\alpha$  value but a low  $\eta$  value. It can be noticed that 4b8 and 4b1 possess a jagged grain boundary without any sharp corner, whereas, grains 4b7 and 4b9 consist of an acute corner with relatively smoother grain boundary. Grain 4b10 doesn't consist of any corner, while grains 4b11 and 4b12 consist of only one corner with their  $\eta$  value equal to their  $\alpha$  value. Grains 4b10, 4b11, 4b12, along with 4a14 shows smooth grain boundaries with low  $\alpha$  value and increasing order of  $\eta$  value. On the other hand, 4b4 and 4b5 represents grains with high  $\alpha$  and  $\eta$  value.

#### 4.4.1.3 $\phi$ vs $v$ plot

Grains having high proportion of straight edges or a high  $\phi$  value ( $>0.3$ ) are represented by 4c1, 4c2, 4c3 and 4c4. These grain boundaries are in order of increasing  $v$  value. Grain boundary 4c5 shows an extreme case of very high  $v$  value (16) along with greater than 0.20  $\phi$  value. On the other hand, grains 4c11, 4c12, 4c13 and 4c14 show low  $\phi$  value ( $<0.05$ ) in an increasing order of  $v$  values from 3 to 15.

#### 4.4.1.4 $\phi$ vs $\alpha$ plot

With a low  $\alpha$  value ( $<10$ ), grains 4d10, 4d8, 4d6 and 4d1 show smooth grain boundaries with an increasing order of  $\phi$  value. On the higher side of the  $\alpha$  value range, grain 4d14 shows a low  $\phi$  value, whereas 4d5 has a similar  $\alpha$  value but a higher  $\phi$  value. Compared to 4d5, grains 4d3 and 4d6 have comparable  $\phi$  values. However, grains 4d5, 4d3 and 4d6 exhibit decreasing  $\alpha$  values.

#### 4.4.1.5 $\alpha$ vs $\nu$ plot

The variation of an increasing  $\alpha$  value for a set of grains with constant  $\nu$  value is shown by the following groups: 4e11 and 4e12; 4e8, 4e6 and 4e1; 4e9 and 4e14. By contrast, for a similar  $\alpha$  value in the range of 40-42, the grains 4e1, 4e2, 4e3, 4e4, 4e5, 4e7 and 4e9 displays the affect of increasing  $\nu$  value.

#### 4.4.1.6 $\phi$ vs $\eta$ plot

Grains 4f1, 4f2, 4f3 and 4f4 consists of high proportion of straight edges ( $\phi > 0.33$ ). However, they vary in terms of  $\eta$  value with 4f1 showing low IRC value for its sharpest corner contrasted to an acute corner present in 4f4. On the higher side of  $\eta$  value ( $>9.5$ ), grains 4f14, 4f9, 4f7 and 4f5 consist of at least one acute corner. However, the fraction of straight edges increase from the grain 4f14 ( $\phi = 0.03$ ) to the grain 4f5 ( $\phi = 0.23$ ).

	No. of Corners ( $\nu$ )	Sharpest Corner ( $\eta$ )	Cumulative Angularity ( $\alpha$ )	Straight Fraction ( $\phi$ )
No. of Corners ( $\nu$ )		0.44	0.94	-0.39
Sharpest Corner ( $\eta$ )	0.44		0.64	-0.19
Cumulative Angularity ( $\alpha$ )	0.94	0.64		-0.42
Straight Fraction ( $\phi$ )	-0.39	-0.19	-0.42	
Roundness	-0.54	-0.43	-0.60	0.05
Angularity	0.68	0.55	0.76	-0.42
Fractal Dimension	0.66	0.62	0.78	-0.40
Irregularity	0.18	0.38	0.28	-0.04
Circularity	-0.26	-0.42	-0.37	0.13
AspectRatio	0.16	0.35	0.25	-0.07
Compactness	-0.20	-0.39	-0.29	0.09
Convexity	-0.48	-0.32	-0.55	0.33
ModRatio	-0.11	-0.31	-0.18	0.04
Rectangularity	-0.32	-0.42	-0.41	0.21
Solidity	-0.63	-0.58	-0.75	0.46

*Table 4.2: Pearson Correlation table showing relation amongst the new shape parameters as well as between the new and existing parameters based on 4000 grain dataset.*

#### 4.4.2 Variation of shape parameters within samples

Box-Whiskers plots showing variation of the different shape parameters are presented in Figure 4.5. Probability distribution plots of the shape parameters for the four sedimentary environments are shown in Figure 4.6. The Kruskal Wallis test (see Tunwal et al., in print) demonstrates that a statistically significant difference ( $p$  value  $<0.05$ ) exists amongst the samples for each of the shape parameters. This implies that the twenty samples are not derived from the same distribution.

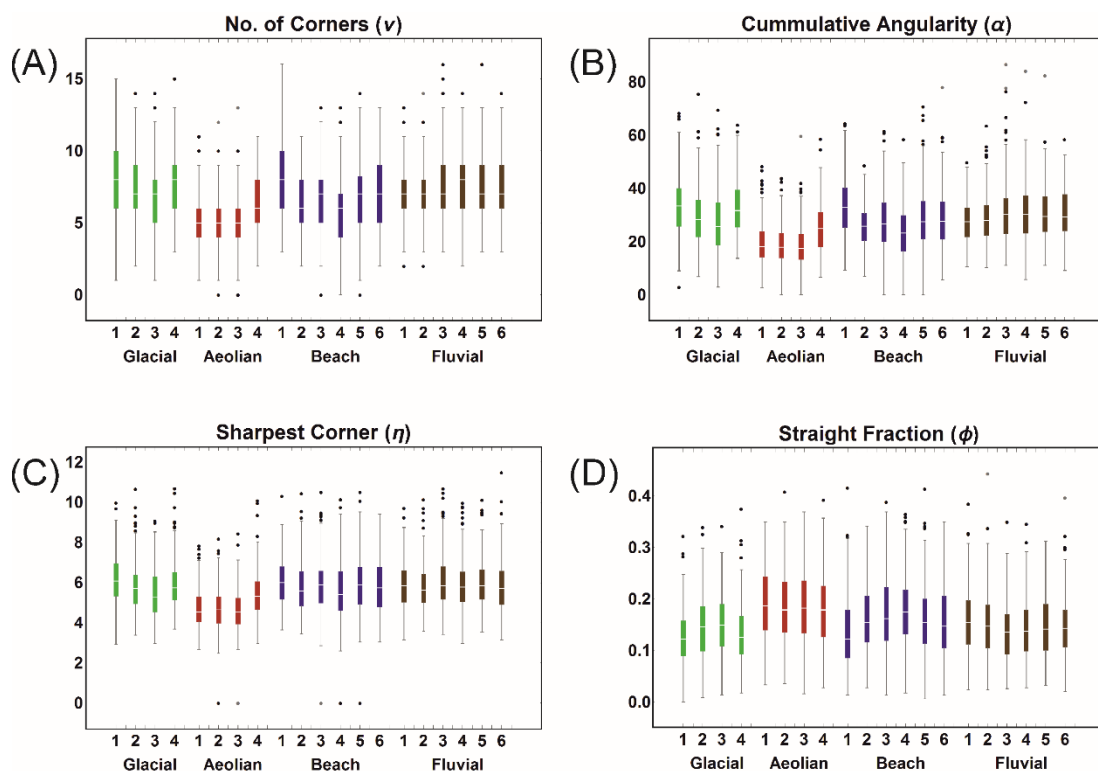


Figure 4.5: Box-Whiskers plot showing distribution of  $v$ ,  $\alpha$ ,  $\eta$  and  $\phi$  values for the 20 samples. Each sample consist of 200 grains.

Aeolian grains tend to exhibit lower  $v$ ,  $\eta$  and  $\alpha$  values compared to rest of the samples, whereas,  $\phi$  values for aeolian samples are relatively higher. There is a considerable overlap for the four shape parameter values for the glacial, beach and fluvial environment. Glacial samples G2 and G3 show lower  $v$ ,  $\eta$  and  $\alpha$  values compared to G1 and G4. On the other hand, G1 and G4 have lower values of straight fraction compared to the samples G2 and G3. Sample B1 shows higher values of  $v$  and  $\alpha$ , and



lower  $\phi$  values compared to the other beach samples. By contrast, sample B4 has lower values of  $v$  and  $\alpha$ , and higher  $\phi$  values. There is no immediately demonstrable pattern observed in fluvial samples for any of the shape parameters.

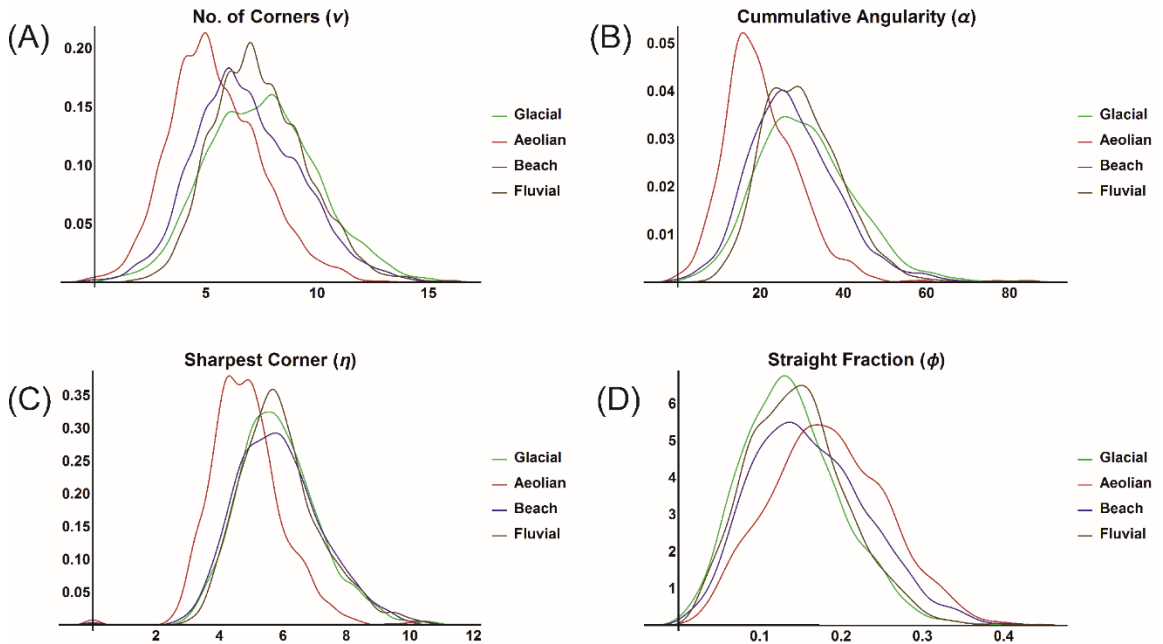


Figure 4.6: Probability distribution plot based on Kernel Density Estimation showing distribution of  $v$ ,  $\alpha$ ,  $\eta$  and  $\phi$  values for the 4 sedimentary environments. Area under each curve is unity.

A Dendrogram was calculated using hierarchical clustering, based on the mean, standard deviation, median, first quantile and third quantile of all four shape parameters for the 20 samples (see Fig. 4.7). Three distinct groups of samples emerge in the dendrogram. Aeolian samples A1, A2 and A3 form the only mono specific environmental group. The remaining two groups consist of samples from multiple sedimentary environments. Furthermore, k-means clustering applied on the entire grain dataset forms three clusters (see Table 4.3). Each cluster consists of grains from each of the sedimentary environments. A higher percentage of aeolian grains are present in cluster 3 and a lower proportion of grains from aeolian environment are part of cluster 1 and 2. On the other hand, grains from glacial, beach and fluvial are present in the 3 clusters in comparable proportions.

## Heirarchical Clustering

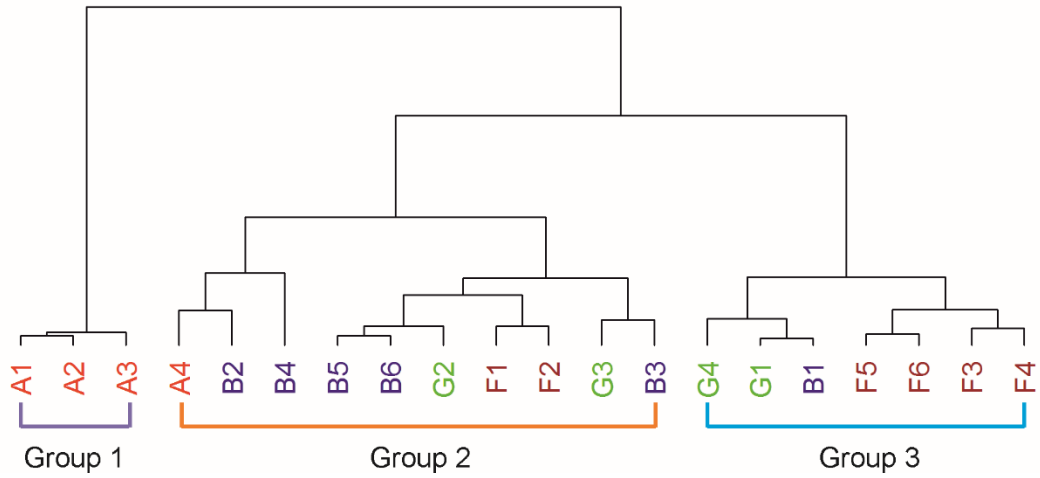


Figure 4.7: Dendrogram showing proximal relationship between the 20 samples based on the summary statistics data (mean, median, average, 1<sup>st</sup> quantile and 3<sup>rd</sup> quantile) of the of  $v$ ,  $\alpha$ ,  $\eta$  and  $\phi$  values for each sample. The three groups formed here corresponds to the increasing order of textural maturity from Group 1 to Group 3 (see Tunwal et al.,(in print) for details).

	Glacial (n=800)	Aeolian (n=800)	Beach (n=1200)	Fluvial (n=1200)
Cluster 1	46.13	29.13	45.58	51.58
Cluster 2	28.87	5.12	20.50	24.00
Cluster 3	25.00	65.75	33.92	24.42

Table 4.3: Table showing percentage of sediment grains from each environment falling into the three clusters formed on the basis of k-means clustering.

## 4.5 Discussion

The methodology presented in this paper allows effective use of image analysis tools for grain shape quantification. The three main steps leading to measurement of shape features involve scaling of the grain boundary, making an IRC plot and identifying peaks in the IRC plot. The shape parameters proposed in this paper are discussed on the basis of their application to a 4000 grain dataset.

The peaks identified in an IRC plot is demonstrated to be characteristic of the grain boundary corners. However, the number of corners ( $v$ ) can't be solely used to describe the boundary features. For example, the grain 4a6 with only 2 corners consists of an acute corner. On the other hand, a grain with high number of peaks may not be very angular (eg., 4a9). Even though there is high correlation between  $v$  and  $\alpha$  (0.94), the two shape parameters compliment each other with the type of shape information they provide. With same  $v$  value, grains 4e11 and 4e12 comprise of the same number of corners. However, due to high variation in their  $\alpha$  value it can be seen that the grain 4e12 is much more angular than 4e11.

A high  $\eta$  value signifies that the grain has at least one sharp corner in its boundary. Therefore, irrespective of the  $v$  and  $\alpha$  values, it is safe to assume that the grain consists of angular feature with high  $\eta$  value (see Fig. 4.8). On the other hand, a low  $\eta$  value doesn't necessarily typify a smooth grain. For example, the grain 4a9/4b8 has lower  $\eta$  value compared to the grain 4a8/4b12 (in which there is only one corner), yet 4a9/4b8 has more irregular boundary compared to 4a8/4b12 owing to its comparatively higher  $\alpha$  value.

The  $\alpha$  value needs to be dealt with the most caution as it is affected by both the number of corners and their individual sharpness. A low  $\alpha$  value may have a sharp corner (for eg., grain 4b14). In contrast, a grain may have a moderately high  $\alpha$  value due to its irregular boundary but could be devoid of any sharp corners. For example, the grain 4b8 has higher  $\alpha$  value compared to the grain 4b14. However, this is due to presence of high number of low IRC value corners in the grain 4b8 which increases its  $\alpha$  value, whereas there is one sharp corner in an otherwise smooth boundary in the grain 4b14. In yet another example, for a comparable  $\alpha$  value, the grains 4e1 and 4e9 differ in terms of sharpness of corners present due to the large difference in their  $v$  value.

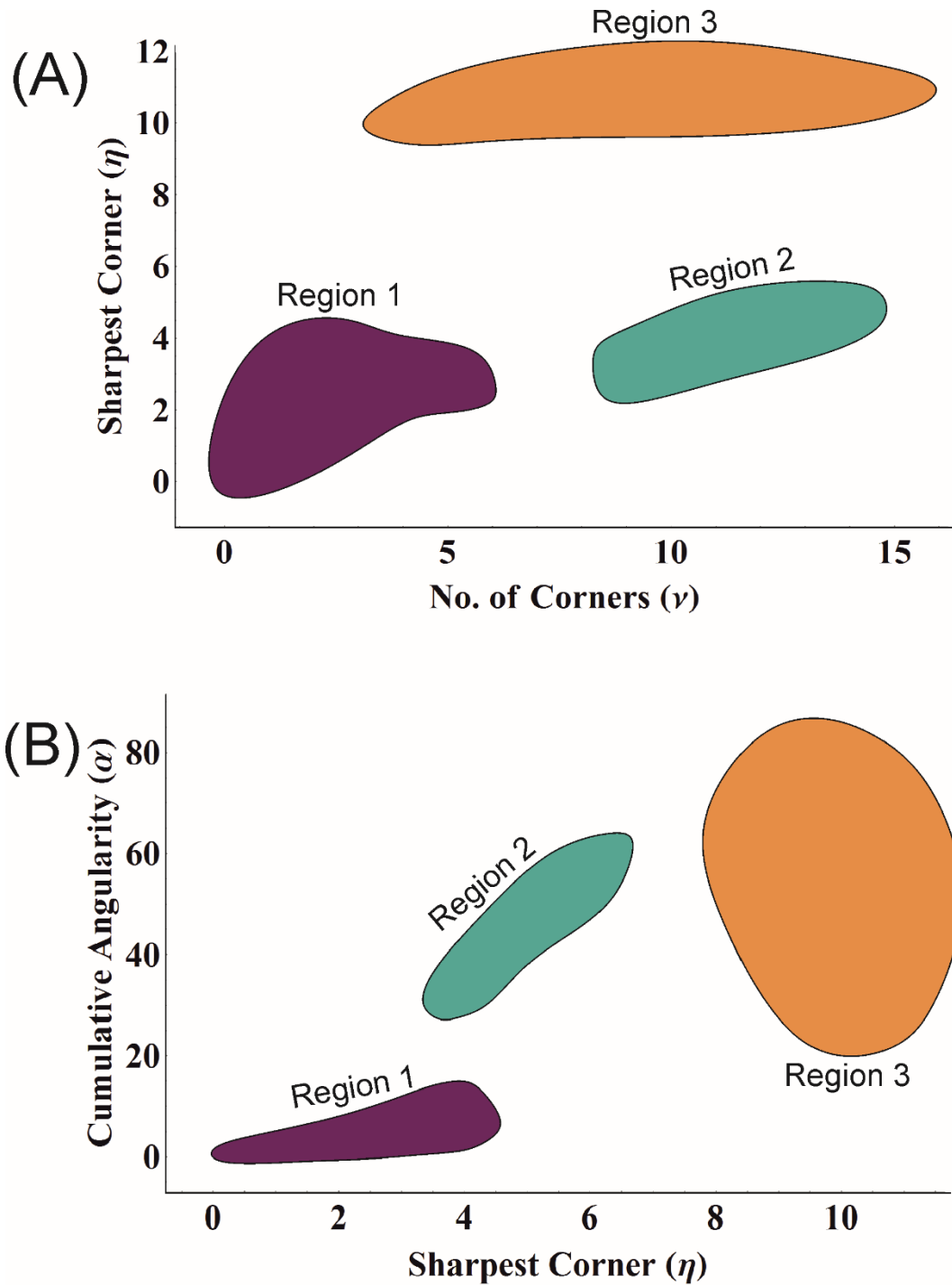


Figure 4.8: Regions within the bivariate plots indicating the grain shape characteristics for: (a)  $\eta$  vs  $\nu$ ; and (b)  $\alpha$  vs  $\eta$ . Region 1 consists of well rounded grains, Region 2 signifies highly irregular grains devoid of any sharp corner Region 3 typifies a highly angular and immature grain boundary.

Straight fraction value is the most unique feature of a grain boundary quantified using the IRC plot. It is largely unrelated to any commonly used shape parameters or the ones discussed in this paper (see Table 4.2). A high  $\phi$  value is indicative of higher proportion of straight edge(s) present in the boundary. This is irrespective of the number or the type of corners present. A typical example of a grain with high  $\phi$  value along with high  $v$  and  $\alpha$  value is the grain 4c5. Similarly, it is possible for a grain boundary with lower  $v$  and  $\alpha$  value to have higher  $\phi$  value (for example, 4c1 or 4d1). On the other hand, a low  $\phi$  value can be present in a highly round (grain 4c8) as well as highly angular grain boundary (4c14). Due to such unique independent attribute of the  $\phi$  value, it should not be used to construe the smoothness and/or roundedness of a grain boundary.

The shape of the grains can be interpreted with reasonable confidence in certain ranges of  $v$ ,  $\eta$  and  $\alpha$  values (see Fig. 4.8). Very high  $\eta$  value will signify a very angular grain irrespective of its  $v$  and  $\alpha$  value (Region 3). Whereas, lower  $\eta$  value along with lower  $v$  and  $\alpha$  value represents a rounded grain (Region 1). A grain with lower  $\eta$  value but higher  $v$  and  $\alpha$  values corresponds to a highly irregular grain boundary without any sharp corner (Region 2). Grains lying on the remaining area of the bivariate plots of Figure 4.8, which do not fall under any of the above discussed regions, should be interpreted with all the three  $v$ ,  $\eta$  and  $\alpha$  values collectively.

The shape parameters introduced in this paper, apart from straight fraction, show some correlation with the existing shape parameters (Table 4.2). This is expected since corner information captured in  $v$ ,  $\eta$  and  $\alpha$  values are bound to be linked to some of the existing parameters. However, a lot of information is uniquely described by the new set of shape parameters which otherwise may have been missed. The two most commonly used shape parameters, roundness and circularity, are compared to the new set of shape parameters (see Fig. 4.4) on the basis of visual grain examples presented in Figure 4.9. In most cases of differences noted in the form of Table 4.4, grains plotted in the roundness-circularity bivariate plot are very similar but have different value(s) for the new shape parameter(s). However, it should be noted that the new shape parameters do not capture the circularity aspect of the grain shape. Therefore, if circularity (or Aspect Ratio) is to be considered then it should be measured separately for the analysis.

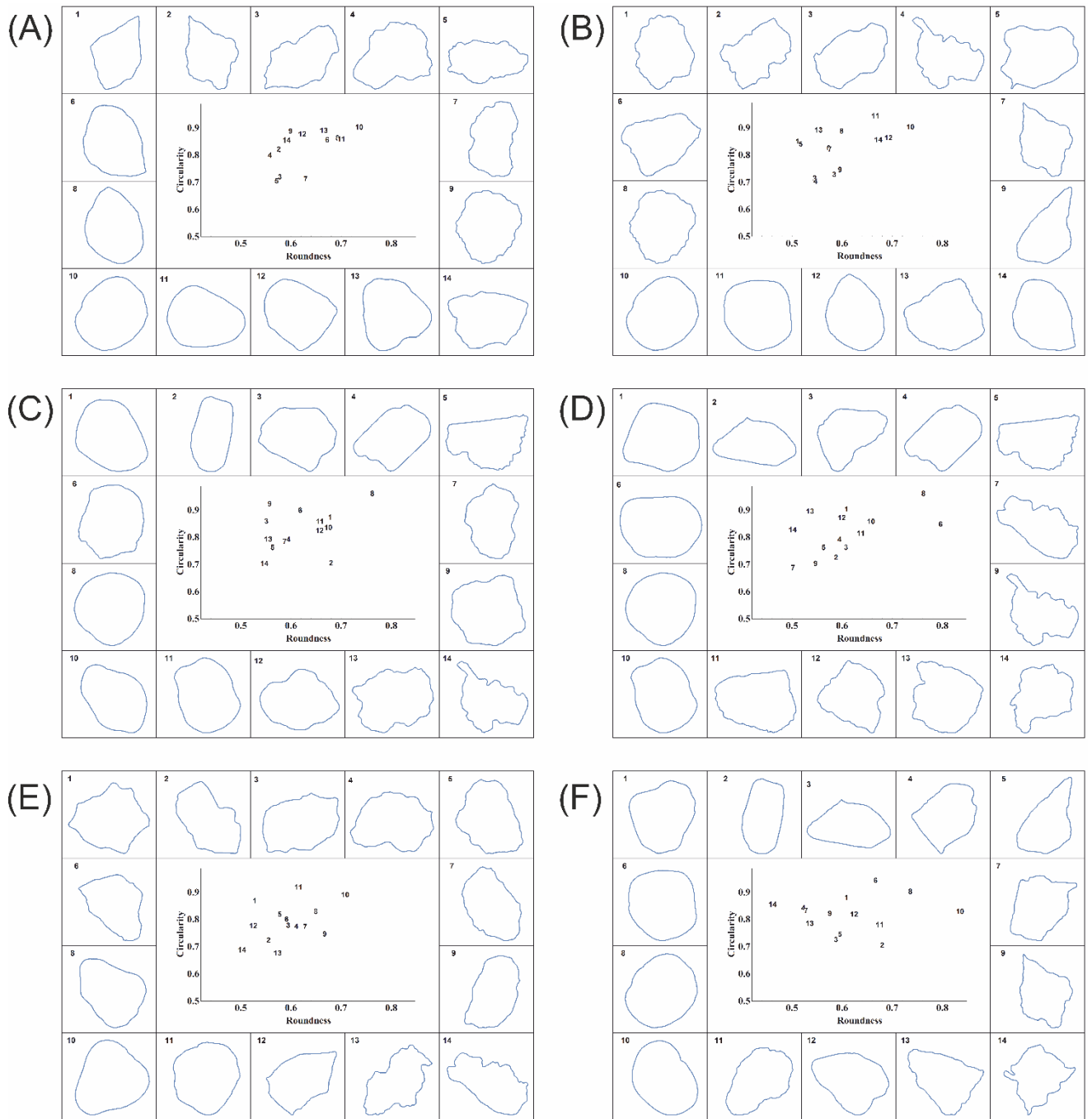


Figure 4.9: Bivariate plots of circularity and roundness for grains displayed in the inset of each subplot of Fig. 4.4. Grains in each subplot (a-f) corresponds to the grains in each subplot of Fig. 4.4.

No.	Subplot (Fig. 4.4 and 4.9)	Grain no.	Remarks
1	a	9, 12	Visually different in smoothness of boundary but similar roundness and circularity values
2	a	6, 13	Acute corner of grain 6 not differentiated from grain 13 in the roundness-circularity plot
3	b	1,5	Grain 5 consisting of a pointed corner has similar roundness and circularity value to grain 1
4	c	5, 13	Grain 5 consisting high straight fraction has similar roundness and circularity values compared to grain 13
5	c	1, 10, 12	The three grains have comparable roundness and circularity values even though they differ visually and have different $\phi$ and $v$ values
6	c	2,3	Grains have comparable $\phi$ and $v$ values but distinct circularity and roundness values
7	d	1, 12	Grains 1 and 12 have similar values of roundness and circularity but look different visually and have large difference in their $\phi$ and $\alpha$ values
8	e	1,2	Grains have comparable $\alpha$ and $v$ values but differ largely on circularity parameter
9	f	3,5,7	Grain 3 has similar roundness and circularity value compared to grain 5 but vary largely on $\phi$ - $\eta$ plot. In contrast, grain 5 has similar $\phi$ - $\eta$ value compared to grain 7 but their roundness and circularity values are distinct.
10	f	10, 11	There is similarity in $\phi$ - $\eta$ values of the grains 10 and 11. However, they have large difference in the roundness values.

*Table 4.4: Some examples of grain pairs (or triplets) from inset of Fig. 4.4 and Fig. 4.9 showing contrasting results from the new shape parameters and existing roundness and circularity parameter.*

The significant differences between the samples based on the set of shape parameters is probably due to the differences in their textural maturity. The overall population level differences in samples within an environment (for eg., G1 and G4 having higher values of  $v$ ,  $\eta$  and  $\alpha$ , and lower  $\phi$  values compared to G2 and G3) conforms to the results from roundness, angularity, irregularity, fractal dimension, solidity, convexity and compactness (refer to Tunwal et al. (in print) for details). This similarity of trends between samples within an environment could be due to corners present in grain boundary affecting both the new as well as some existing shape parameters. However, distribution of  $\phi$  values need to be interpreted carefully since they are largely unrelated to the corners present in a grain.

The grouping of samples based on hierarchical clustering is comparable to the one formed by existing shape parameters (Tunwal et al., in print), with some minor differences in group 2 and group 3. This shows that the aeolian samples A1, A2 and A3 are consistently different than rest of the samples based on the existing as well as new set of shape parameters. This can be further confirmed with the differences in the probability distribution plots for the four environments (Fig. 4.6). Furthermore, the results from k-means clustering indicates that grains from glacial, beach and fluvial environments show similar grain shape variation, thus falling in similar proportions in the clusters formed.

A major advantage of using the proposed shape parameters is that their values can be directly correlated to the visual descriptions of the grain. The representation of a grain shape in four components ( $v$ ,  $\alpha$ ,  $\eta$  and  $\phi$  values) is a major departure from the point of view where grain shape was quantified in a single value (for eg., roundness, circularity). The IRC plot, which lies at the heart of this methodology, can be further utilised according to any other specific shape quantification requirement. This methodology thus has the potential to bring a radical change in the way shape is quantified.

## 4.6 Conclusion

A new approach to grain shape quantification is introduced in this paper. IRC plot proposed here can be used to identify corners and measure their sharpness. A suite of shape parameters correlating directly with the corners (Number of corners ( $v$ ), Cumulative Angularity( $\alpha$ ) and Sharpest Corner( $\eta$ )) and straight fraction ( $\phi$ ) present



in grain boundary is presented. In comparison to existing shape parameters, the newly proposed parameters provide information regarding the grain boundary which may have been otherwise missed. These parameters are applied to natural grains from glacial, aeolian, beach and fluvial environment, thus assessing their utility in grain shape description, textural maturity analysis and sedimentary environment discrimination. The textural maturity of samples agrees with a previous study of the data using existing shape parameters. It is demonstrated here that there exists a relationship between the proposed set of parameters and the visual perception of grain shape.

The IRC plot introduced in this paper is applied to quantify grain shape from a sedimentological perspective. The information derived from such a plot has the potential to be applied in other shape specific applications. Further studies with higher numbers of samples and different research perspectives needs to be done to test this methodology and ensure that the results obtained are reproducible. This paper hopes to open up the avenue for a shape measurement approach where the quantified numbers can be visually justified.

#### 4.7 Acknowledgement

This project is funded by the Irish Shelf Petroleum Studies Group (ISPSG) of the Irish Petroleum Infrastructure Programme (PIP) Group 4. The ISPSG comprises: Atlantic Petroleum (Ireland) Ltd, Cairn Energy Plc, Chrysaor E&P Ireland Ltd, Chevron North Sea Limited, ENI Ireland BV, Europa Oil & Gas (Holdings) plc, ExxonMobil E&P Ireland (Offshore) Ltd., Kosmos Energy LLC, Maersk Oil North Sea UK Ltd, Petroleum Affairs Division of the Department of Communications, Energy and Natural Resources, Providence Resources plc, Repsol Exploración SA, San Leon Energy Plc, Serica Energy Plc, Shell E&P Ireland Ltd, Sosina Exploration Ltd, Statoil (UK) Ltd, Tullow Oil Plc and Woodside Energy (Ireland) Pty Ltd.

## 4.8 References

- Al-Rousan, T., Masad, E., Tutumluer, E. and Pan, T.** (2007) Evaluation of image analysis techniques for quantifying aggregate shape characteristics. *Construction and Building Materials*, **21**, 978-990.
- Barrett, P.J.** (1980) The shape of rock particles, a critical review. *Sedimentology*, **27**, 291-303.
- Blatt, H.** (1992) *Sedimentary Petrology*. W. H. Freeman and Company, New York, 514 pp.
- Blatt, H., Middleton, G.V. and Murray, R.C.** (1972) *Origin of sedimentary rocks*. Prentice-Hall Inc., New Jersey, 634 pp.
- Blott, P.J. and Pye, K.** (2008) Particle shape: a review and new methods of characterization and classification. *Sedimentology*, **55**.
- Cailleux, A.** (1947) L'indice d'emousse: definition et premiere application. *CRS Soc. géol*, 250-252.
- Cox, M.R. and Budhu, M.** (2008) A practical approach to grain shape quantification. *Engineering Geology*, **96**, 1-16.
- Dobkins, J.E. and Folk, R.L.** (1970) Shape development on Tahiti-nui. *Journal of Sedimentary Research*, **40**, 1167-1203.
- Farrington, A.** (1960) The Lee Basin: Part 2, the Drainage Pattern. *Proceedings of the Royal Irish Academy. Section B: Biological, Geological, and Chemical Science*, **61**, 233-253.
- Krumbein, W.C.** (1941) Measurement and geological significance of shape and roundness of sedimentary particles. *Journal of Sedimentary Research*, **11**, 64-72.
- Kuenen, P.H.** (1956) Experimental abrasion of pebbles: 2. Rolling by current. *The Journal of Geology*, **64**, 336-368.
- Ó Cofaigh, C., Telfer, M.W., Bailey, R.M. and Evans, D.J.A.** (2012) Late Pleistocene chronostratigraphy and ice sheet limits, southern Ireland. *Quaternary Science Reviews*, **44**, 160-179.
- Pant, R.** (1993) Spread of loess and march of desert in western India. *Current Science* **64**, 841-847.
- Paris, S., Kornprobst, P., Tumblin, J. and Durand, F.** (2009) Bilateral filtering: Theory and applications. *Foundations and Trends® in Computer Graphics and Vision*, **4**, 1-73.

- Pettijohn, F.J., Potter, P. and Siever, R.** (1972) *Sand and Sandstone*. Springer-Verlag, New York, 618 pp.
- Powers, M.C.** (1953) A new roundness scale for sedimentary particles. *Journal of Sedimentary Research*, **23**, 117-119.
- Pracht, M., Sleeman, A., Wright, G. and Cox, W.** (2002) A Geological Description of West Cork and Adjacent parts of Kerry to Accompany the Bedrock Geology 1: 100,000 Scale Map Series, Sheet 24, West Cork, with Contributions by G. *With accompanying contributions by G. Wright (Groundwater) and W. Cox (Minerals)*, Geological Survey of Ireland, 79pp.
- Pulham, A.J.** (1989) Controls on internal structure and architecture of sandstone bodies within Upper Carboniferous fluvial-dominated deltas, County Clare, western Ireland. *Geological Society, London, Special Publications*, **41**, 179-203.
- Rao, C., Tutumluer, E. and Kim, I.T.** (2002) Quantification of Coarse Aggregate Angularity Based on Image Analysis. *Journal of the Transportation Research Board*, **1787**, 117-124.
- Riley, N.A.** (1941) Projection sphericity. *Journal of Sedimentary Research*, **11**, 94-97.
- Roussillon, T., Piégay, H., Sivignon, I., Tougne, L. and Lavigne, F.** (2009) Automatic computation of pebble roundness using digital imagery and discrete geometry. *Computers & Geosciences*, **35**, 1992-2000.
- Schwarcz, H.P. and Shane, K.C.** (1969) Measurements of particle shape by Fourier analysis. *Sedimentology*, **13**.
- Singhvi, A. and Kar, A.** (2004) The aeolian sedimentation record of the Thar Desert. *Journal of Earth System Science*, **113**, 371-401.
- Sochan, A., Zieliński, P. and Bieganski, A.** (2015) Selection of shape parameters that differentiate sand grains, based on the automatic analysis of two-dimensional images. *Sedimentary Geology*, **327**, 14-20.
- Suzuki, K., Fujiwara, H. and Ohta, T.** (2015) The evaluation of macroscopic and microscopic textures of sand grains using elliptic Fourier and principal component analysis: Implications for the discrimination of sedimentary environments. *Sedimentology*, **62**, 1184-1197.
- Swan, B.** (1974) Measures of particle roundness: a note. *Journal of Sedimentary Research*, **44**, 572-577.

- Tafesse, S., Robison Fernlund, J.M., Sun, W. and Bergholm, F.** (2013) Evaluation of image analysis methods used for quantification of particle angularity. *Sedimentology*, **60**, 1100-1110.
- Takashimizu, Y. and Iiyoshi, M.** (2016) New parameter of roundness R: circularity corrected by aspect ratio. *Progress in Earth and Planetary Science*, **3**, 2.
- Thomas, M.C., Wiltshire, R.J. and Williams, A.T.** (1995) The use of Fourier descriptors in the classification of particle shape. *Sedimentology*, **42**, 635-645.
- Tunwal, M., Mulchrone, K.F. and Meere, P.A.** (in print) Quantitative characterisation of grain shape: Implications for textural maturity analysis and discrimination between depositional environments. *Sedimentology*.
- Tietzsch-Tyler, D. and Sleeman, A.** (1994) A geological description of South Wexford and adjoining parts of Waterford, Kilkenny and Carlow to accompany the Bedrock Geology 1: 100,000 scale map series, Sheet 23, South Wexford. *Geological Survey of Ireland, Dublin*.
- Wadell, H.** (1932) Volume, Shape, and Roundness of Rock Particles. *The Journal of Geology*, **40**, 443-451.
- Wentworth, C.K.** (1919) A laboratory and field study of cobble abrasion. *The Journal of Geology*, **27**, 507-521.

## 5 Constraining basin parameters using a known subsidence history

*Mohit Tunwal<sup>1)2)</sup>\*, Kieran F. Mulchrone<sup>2)</sup> and Patrick A. Meere<sup>1)</sup>*

(Current status: ready for submission)

*<sup>1)</sup> School of Biological, Earth and Environmental Sciences, University College Cork, Distillery Fields, North Mall, Cork, Ireland*

*<sup>2)</sup> School of Mathematical Sciences, University College Cork, Western Gateway Building, Western Road, Cork, Ireland*

### Abstract

Subsidence modelling is an important part of basin analysis to better understand the tectonic evolution of sedimentary basins. The McKenzie model has been widely applied for subsidence modelling and stretching factor estimation for sedimentary basins formed in an extensional tectonic environment. In this contribution, a numerical model is presented that takes into account the effect of sedimentary cover on stretching factor estimation.

Subsidence modelling requires values of physical parameters (crustal thickness, lithospheric thickness, stretching factor, etc.) which may not be always available. With a given subsidence history of a basin estimated using a stratigraphic backstripping method, these parameters can be estimated by quantitatively comparing the known subsidence curve with modelled subsidence curves. In this contribution, a method to compare known and modelled subsidence curves is presented aiming to constrain valid combinations of stretching factor, crustal thickness and lithospheric thickness of a basin.

The parameter fitting method presented here is first applied to synthetically generated subsidence curves. Next, a case study using a known subsidence curve from the Campos Basin, offshore Brazil is considered. The range of stretching factors estimated for the Campos basin from this study is in accordance with previous work, with an

additional estimate of corresponding lithospheric thickness. This study provides insights into the dependence of subsidence modelling methods on assumptions about input parameters as well as allowing for the estimation of valid combinations of physical lithospheric parameters, where the subsidence history is known.

\*Corresponding author: [mohittunwal@gmail.com](mailto:mohittunwal@gmail.com)

Keywords: basin subsidence, numerical modelling, McKenzie model, rift basin

## 5.1 Introduction

The geodynamic evolution history of a sedimentary basin has significant implications for its hydrocarbon bearing potential. McKenzie (1978) provided the first physical concept for the formation of sedimentary basins in an extensional setting. In McKenzie's model, pure shear was assumed to act during uniform instantaneous stretching and was followed by a gradual thermal cooling of the lithosphere. Following this seminal work, a number of variations on the McKenzie model were suggested. Some considered simple shear (Wernicke, 1981; Wernicke, 1985), a combination of pure and simple shear (Kusznir et al., 1991), flexural response of the lithosphere to sediment loading (Stephenson et al., 1989; Watts et al., 1982), non-uniform stretching of the lithosphere (Rowley and Sahagian, 1986; Royden and Keen, 1980), non-instantaneous (finite) stretching time (Jarvis and McKenzie, 1980), the blanketing effect of sediments (Lucazeau and Le Douaran, 1985; Wangen, 1995), the effect of radiogenic heat production (Hantschel and Kauerauf, 2009), the effect of magmatic activity (White and McKenzie, 1989) and depth of lithospheric necking along with rift shoulder erosion (Kooi et al., 1992; van Balen et al., 1995).

McKenzie's model presents an analytical solution for basin subsidence (Wangen, 2010). Numerical modelling allows relaxation of certain assumptions which were necessary to derive an analytical solution (Burov and Poliakov, 2001; Hantschel and Kauerauf, 2009). A numerical model in 1-Dimension is presented here which considers the effect of sediment cover during thermal subsidence. Subsidence models, whether analytical or numerical, are as good as the assumptions they use. All of these

models depend upon the values taken for physical parameters such as density and thickness of crust and lithosphere. The aim of this paper is to compare subsidence profiles estimated through the backstripping method (Hölzel et al., 2008; Steckler and Watts, 1978) with forward subsidence models (i.e., McKenzie's analytical model and the numerical model introduced here) and to explore optimum estimation of values for stretching factor, crustal and lithospheric thickness. These estimates may feed into more comprehensive and sophisticated basin models (e.g. Chen et al. (2013); Lee et al. (2016)).

In this paper, a numerical approach which incorporates the effect of sedimentary cover is first presented. Next, a simple quantitative method for comparing measured subsidence curves with numerical and/or analytical outputs is proposed over the sample space of stretching factor, crustal and lithospheric thickness. Finally, the methodology is tested using synthetic data and is then applied to a natural subsidence dataset obtained from the Campos basin, offshore Brazil (Contreras et al., 2010) to estimate a range of stretching factors and lithospheric thicknesses suitable for basin modelling.

## 5.2 Numerical model

Subsidence of a sedimentary basin in an extensional setting is modelled by two separate stages (i) instantaneous stretching of the lithosphere followed by (ii) gradual thermal cooling. It is assumed that the basin is nourished with sediments and subsidence is closely accompanied by sedimentation. Furthermore, it is assumed that:

- 1) Uniform instantaneous stretching for the initial phase is by pure shear
- 2) A constant asthenospheric temperature is maintained at a fixed depth equal to initial position of the base of the lithosphere.
- 3) Radiogenic heat production is ignored.

### 5.2.1 Initial Stretching

First, the instantaneous stretching phase is considered (see Fig. 5.1).

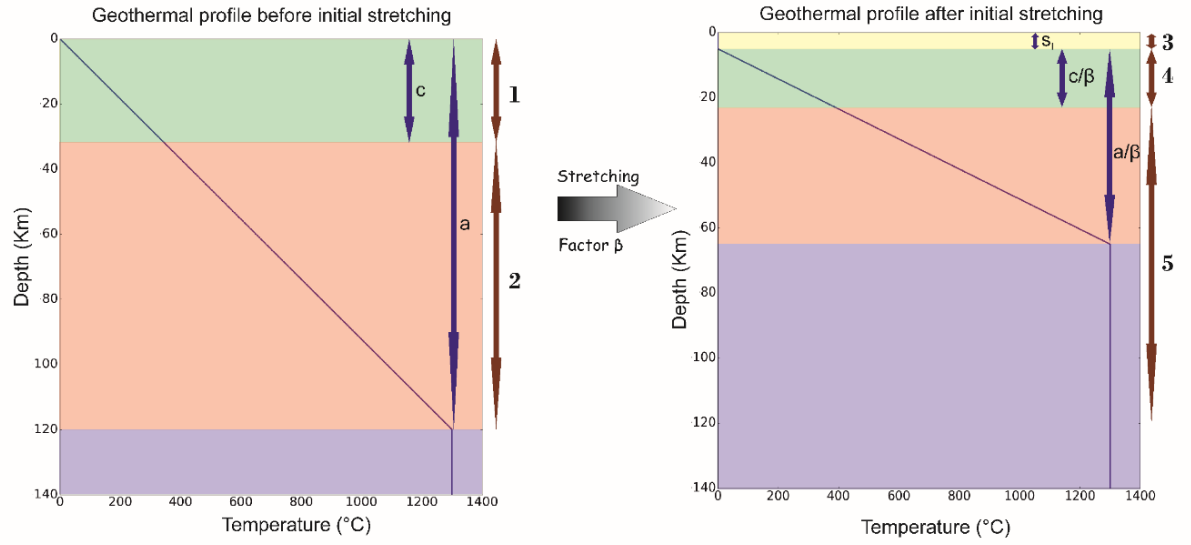


Figure 5.1: Thermal gradient before and after uniform instantaneous stretching by a factor  $\beta$ . The integrals of eq. 5.3 are annotated in front the respective layers (sediment layer, crust, lithospheric mantle and asthenospheric mantle are represented by yellow, green, orange and purple colour respectively). The crustal thickness is taken as 32 Km, lithospheric thickness before stretching is 120 Km and  $\beta$  is 2. The initial subsidence from eq. 5.7 is estimated to be 5.078 Km.

The sedimentary layer ( $s_l$ ) deposited during the instantaneous lithospheric extension is assumed to remain at the surface temperature ( $T_s$ ) during the stretching phase, whereas, the temperature of the asthenosphere remains constant at  $T_a$ . The density of crust and mantle at any temperature ( $T$ ) is given by the first order approximation:

$$\rho_c(T) = \rho_{c,0}(1 - \alpha T) \quad \text{Eq. 5.1}$$

$$\rho_m(T) = \rho_{m,0}(1 - \alpha T) \quad \text{Eq. 5.2}$$

where  $\alpha$  is the thermal expansion factor and,  $\rho_{c,0}$  and  $\rho_{m,0}$  are the density of crust and mantle respectively at 0°C. The density of sediments ( $\rho_s$ ) is assumed to remain



constant. Due to the rise of lithospheric temperature after stretching (see Fig. 5.1), the density of the crust and mantle will decrease. However, the thinning of the lithosphere leads to an initial subsidence in order to maintain isostatic equilibrium. The isostasy equation for the pressure at the depth  $a$  is given by:

$$\begin{aligned}
 & \int_0^c \rho_c(T_U(z))dz + \int_c^a \rho_m(T_U(z))dz = \\
 & \qquad \qquad \qquad \mathbf{1} \qquad \qquad \qquad \mathbf{2} \\
 & \int_0^{s_I} \rho_s dz + \int_{s_I}^{s_I + \frac{c}{\beta}} \rho_c(T_I(z))dz + \int_{s_I + \frac{c}{\beta}}^a \rho_m(T_I(z))dz \quad Eq. 5.3 \\
 & \qquad \qquad \qquad \mathbf{3} \qquad \qquad \qquad \mathbf{4} \qquad \qquad \qquad \mathbf{5}
 \end{aligned}$$

where  $c$  and  $a$  are thickness of crust and lithosphere respectively prior to stretching. The stretching factor  $\beta$  is defined to be the pre stretched lithosphere thickness divided by the post initial stretching lithospheric thickness. The left hand-side of the Eq. 5.3 represents the pressure at the boundary of lithosphere and asthenosphere at depth  $a$  before stretching. The temperature dependence of crust and mantle is based on thermal profile  $T_U(z)$  which is thermal gradient at undisturbed state prior to stretching (Eq. 5.5). On the right hand-side of the Eq. 5.3 denotes the pressure after uniform instantaneous stretching. The thermal gradient at this state is  $T_I(z)$  for density estimation of crust and mantle. The integrals terms of Eq. 5.3 are shown in Figure 5.1 for visualisation. Replacing the density terms in Eq. 5.3 from Eq. 5.1 and Eq. 5.2 gives:

$$\int_0^c \rho_{c,0}(1 - \alpha T_U(z))dz + \int_c^a \rho_{m,0}(1 - \alpha T_U(z))dz =$$

$$\int_0^{s_I} \rho_s dz + \int_{s_I}^{s_I + \frac{c}{\beta}} \rho_{c,0}(1 - \alpha T_I(z))dz + \int_{s_I + \frac{c}{\beta}}^a \rho_{m,0}(1 - \alpha T_I(z))dz \quad Eq. 5.4$$

The thermal gradients  $T_U$  and  $T_I$  (see Fig. 5.1) as depth dependent function is given by:

$$T_U(z) = \begin{cases} \frac{(T_a - T_s)}{a}z + T_s, & 0 \leq z < a \\ T_a, & a \leq z \end{cases} \quad Eq. 5.5$$

$$T_I(z) = \begin{cases} T_s, & 0 \leq z < s_I \\ \frac{\beta}{a}(T_a - T_s)(z - s_I) + T_s, & s_I \leq z < s_I + \frac{a}{\beta} \\ T_a, & s_I + \frac{a}{\beta} \leq z \end{cases} \quad Eq. 5.6$$

Replacing the terms  $T_U(z)$  and  $T_I(z)$  in eq. 5.4 by eq. 5.5 and eq. 5.6 gives the initial subsidence ( $s_I$ ) as:

$$s_I = \frac{(-1 + \beta)(c(2a - c\alpha T_a + (-2a + c)\alpha T_s)\rho_c + (-2ac + (a^2 + c^2)\alpha T_a - (a - c)^2\alpha T_s)\rho_m)}{2a\beta(\rho_s + (-1 + \alpha T_a)\rho_m)}$$

Eq. 5.7

### 5.2.2 Gradual Subsidence

After instantaneous stretching there is a gradual conductive cooling of the lithosphere, which leads to an increase in crustal and mantle density (*Eq.s* 5.1 and 5.2). In order to maintain an isostatic balance, the basin gradually subsides. The model developed here maintains two boundary conditions: 1) at a depth  $a$  and below, the asthenospheric mantle is at a constant temperature  $T_a$  throughout the stretching and cooling phase; and 2) the surface temperature remains constant at  $T_s$ .

The 1-dimensional equation for conductive cooling is given by:

$$\frac{\partial T}{\partial t} - \kappa \frac{\partial^2 T}{\partial z^2} = 0 \quad \text{Eq. 5.8}$$

where  $\kappa$  is the thermal diffusivity, a material property, which is taken to be the same for all layers. This thermal diffusion equation is solved using an Implicit Euler's method (Holmes, 2007).

Ongoing basin development due to thermal subsidence leads to the deposition of a thickening sedimentary layer ( $s_t$  at any given time  $t$ ) on top of the initially deposited sediments,  $s_l$  (see Fig. 5.2). During each small time step  $\Delta t$ , the basin subsides by a small depth  $\Delta s$  and is instantaneously infilled by sediment. Therefore  $s_t$  is the sum of each  $\Delta s$  for each  $\Delta t$  up to  $t$ . The calculation of  $\Delta s$ , at each time step, depends upon the isostatic balance of pressure at the depth  $a$ . The isostasy equations at time  $t$  and  $t + \Delta t$  are given by *Eq. 5.9* and *Eq. 5.10* respectively.

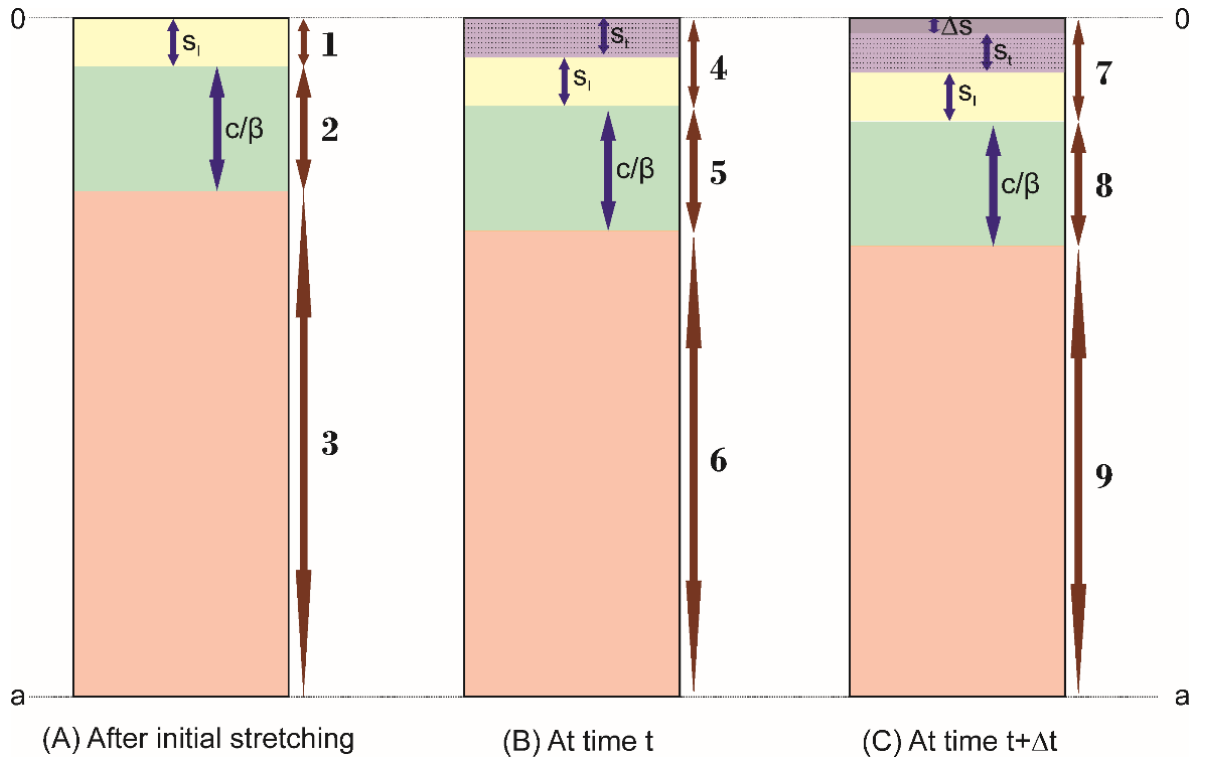


Figure 5.2: Schematic diagram, not to scale, showing subsidence of thinned crust of thickness  $(c/\beta)$  and sediments deposited during initial subsidence ( $s_1$ ), as the model progresses (they are of constant thickness throughout). The integrals terms along with the different layers in the diagram correspond to their individual pressure as used in the eq.9 and eq.10. (a) shows basin configuration just after initial subsidence. (b) represents subsidence of thinned crust and  $s_1$  at some time  $t$  after instantaneous stretching.  $s_t$  denotes sedimentary layer deposited during time  $t$  due to thermal subsidence. (c) shows addition of sedimentary layer of thickness  $\Delta s$  during the time  $\Delta t$  after time  $t$ . Sediments deposited at each time step  $\Delta t$  fill up the space generated due to thermal subsidence during time  $\Delta t$ .

The equations compare pressure at depth  $a$  after initial stretching at the start of thermal cooling (on the left hand-side) and pressure at the same depth at time  $t$  (Eq. 5.9) and  $t + \Delta t$  (Eq. 5.10) respectively. At any time  $t$ , the isostasy equation is:

$$\int_0^{s_I} \rho_s dz + \int_{s_I}^{s_I + \frac{c}{\beta}} \rho_c(T_I(z)) dz + \int_{s_I + \frac{c}{\beta}}^a \rho_m(T_I(z)) dz =$$

**1                      2                                      3**

$$\int_0^{s_I + s_t} \rho_s dz + \int_{s_I + s_t}^{s_I + s_t + \frac{c}{\beta}} \rho_c(T(z, t)) dz + \int_{s_I + s_t + \frac{c}{\beta}}^a \rho_m(T(z, t)) dz \quad \text{Eq. 9}$$

**4                                      5                                      6**

The integral terms are annotated in the Figure 5.2 to their corresponding layers present in the system. The includes the term  $T(z, t)$ , the thermal transient profile at time at any time  $t$ . The isostasy equation at the time  $t + \Delta t$  is given by:

$$\int_0^{s_I} \rho_s dz + \int_{s_I}^{s_I + \frac{c}{\beta}} \rho_c(T_I(z)) dz + \int_{s_I + \frac{c}{\beta}}^a \rho_m(T_I(z)) dz = \quad \text{Eq. 5.10}$$

**1                      2                                      3**

$$\int_0^{s_I + s_t + \Delta s} \rho_s dz + \int_{s_I + s_t + \Delta s}^{s_I + s_t + \Delta s + \frac{c}{\beta}} \rho_c(T(z, t + \Delta t)) dz + \int_{s_I + s_t + \Delta s + \frac{c}{\beta}}^a \rho_m(T(z, t + \Delta t)) dz$$

**7                                      8                                      9**

By replacing density terms by *Eq. 5.1* and *Eq. 5.2* in *Eq. 5.10* gives:

$$\int_0^{s_I} \rho_s dz + \int_{s_I}^{s_I + \frac{c}{\beta}} \rho_{c,0} (1 - \alpha T_I(z)) dz + \int_{s_I + \frac{c}{\beta}}^a \rho_{m,0} (1 - \alpha T_I(z)) dz = \quad \text{Eq. 5.11}$$

$$\int_0^{s_I + s_t + \Delta s} \rho_s dz + \int_{s_I + s_t + \Delta s}^{s_I + s_t + \Delta s + \frac{c}{\beta}} \rho_{c,0} (1 - \alpha T(z, t + \Delta t)) dz + \int_{s_I + s_t + \Delta s + \frac{c}{\beta}}^a \rho_{m,0} (1 - \alpha T(z, t + \Delta t)) dz$$

The thermal profile of the isostatic system considered during the cooling stage is affected by the sediments deposited after initial stretching and during the thermal subsidence phase. This can be noted from the inter-dependency of terms  $s_t$  and  $T(z, t)$  in the *Eq. 5.9* and the terms  $s_t + \Delta s$  and  $T(z, t + \Delta t)$  in the *Eq. 5.10* and *Eq. 5.11*. Using the *Eq. 5.8*, the thermal profile is calculated numerically at each time step (see appendix). Next, the thermal subsidence  $\Delta s$  is calculated for the time step. This layer of sediment  $\Delta s$  is then added to the system for lithospheric cooling and the thermal profile is calculated for the next time step. However, since  $\Delta s$  is dependent upon the integral of the term  $T(z, t + \Delta t)$  in *Eq. 5.11*, the following simplifying approximations are required to solve the equation:

$$q_1 = \rho_{c,0} \cdot \alpha \int_{s_I + s_t + \Delta s}^{s_I + s_t + \Delta s + \frac{c}{\beta}} T(z, t + \Delta t) dz \cong \rho_{c,0} \cdot \alpha \int_{s_I + s_t}^{s_I + s_t + \frac{c}{\beta}} T(z, t) dz \quad \text{Eq. 5.12}$$

$$q_2 = \rho_{m,0} \cdot \alpha \int_{s_I + s_t + \Delta s + \frac{c}{\beta}}^a T(z, t + \Delta t) dz \cong \rho_{m,0} \cdot \alpha \int_{s_I + s_t + \frac{c}{\beta}}^a T(z, t) dz \quad \text{Eq. 5.13}$$

In other words the temperature profile in the lithosphere and asthenosphere throughout the time step i.e. from  $t$  to  $t + \Delta t$ , is approximated by the profile at time  $t$ . Using the

approximations in Eq. 5.12 and Eq. 5.13, the thermal subsidence for a given time step is calculated as:

$$\Delta S = \frac{c_1 + \alpha T_a \rho_{m,0} (a - s_t) - s_t (\rho_{m,0} - \rho_s) - q_1 - q_2 + c_2}{\rho_{m,0} - \rho_s} \quad Eq. 5.14$$

where the term  $c_1$  and  $c_2$  are constants given by:

$$c_1 = \frac{\alpha T_a (c^2 (\rho_{c,0} - \rho_{m,0}) - a^2 \rho_{m,0})}{2a\beta} \quad Eq. 5.15$$

$$c_2 = \frac{\alpha \cdot T_s (c \cdot \rho_{c,0} (2a - c) + \rho_{m,0} (a - c)^2)}{2a\beta} \quad Eq. 5.16$$

The thickness of the sedimentary layer deposited during thermal subsidence ( $s_t$ ) varies from 0 at the start of cooling to  $s_{Ft}$  at  $t \rightarrow \infty$ . The depth  $a$  in the mantle is assumed to remain at constant temperature  $T_a$  according to the boundary condition. Thus at  $t \rightarrow \infty$  with the thermal equilibrium of the cooling system, the final thermal profile for this model will be  $T_F(z) = T_a z/a$ . Please note that the final thermal profile  $T_F(z)$  is same as the thermal profile of the system before initial stretching  $T_U(z)$ . Another numerical model was considered (see appendix) in which the uppermost point in asthenosphere which remains at constant temperature  $T_a$  subsides with the rate of thermal subsidence. However, it was found that the subsidence results do not vary significantly from the model presented here.

### 5.3 Curve fitting method

Subsidence modelling, either analytical (McKenzie's model) or numerical, requires constant numerical values of model parameters for calculation. Some of the typical parameters used in the models are: stretching factor ( $\beta$ ), lithospheric thickness ( $a$ ),

crustal thickness ( $c$ ), density of sedimentary layer ( $\rho_s$ ), crust ( $\rho_c$ ) and mantle ( $\rho_m$ ), constants for thermal expansibility ( $\alpha$ ) and thermal diffusivity ( $\kappa$ ). Density of the different layers as well as thermal expansibility and diffusivity constant can be provided with known and estimated values of the parameters (Wangen, 2010). In the case of crustal thickness prior to stretching, estimates from deep seismic imaging and gravity profiling of adjoining unstretched crust can be used as proxies (Lebedev et al., 2013; Mohriak et al., 1990). In absence of such geophysical measurements, it is difficult to estimate either the crust or the stretching factor. The initial lithospheric depth, however, is difficult to estimate and there appears to be no immediate guidance on how to find location specific values.

The fitting method described below uses a known subsidence history which can be estimated using the stratigraphic backstripping technique. Values of lithospheric thickness, stretching factor or crustal thickness can be estimated using the fitting method described here. For a fixed value of crustal thickness, lithospheric thickness is varied from 100 Km to 200 Km with a 5 Km step. In case of the stretching factor, the range is 1.25 to 4.00 with an increment of 0.05 at each step. The subsidence models are run for 1176 (21\*56) combinations of lithospheric depth and stretching factor and for a fixed value of crustal depth.

For each parameter combination, the fit between the calculated subsidence curve and the known subsidence curve is estimated. The error between the two curves is estimated by:

$$E_1 = \sum_{i=0}^n (Sk_i - Sm_i) \quad Eq. 5.17$$

$$E_2 = \sum_{i=0}^n (Sk_i - Sm_i)^2 \quad Eq. 5.18$$

where  $Sk_i$  and  $Sm_i$  are the known subsidence and modelled subsidence at time step  $i$  respectively. The modelled subsidence values may be from either the McKenzie model or the numerical model or some other model variation (not considered here). The variable  $i$  goes from 0 to  $n$  which is the total number of time steps in the model. In the domain space for lithospheric thickness and stretching factor values, the minimum  $E_1$



region represented by a zero-line on a contour plot corresponds to the region where the sum of the difference between subsidence and modelled subsidence curves is zero. It is not necessarily the best fit curve. Whereas, the minima of  $E_2$  in the parameter domain represents best fit curve can be quite an extensive region. Our results indicate that the minimum  $E_1$  curve typically lies within the region of the minimum best fit curve (the minimum  $E_2$  region) and that the zero-line of  $E_1$  represents a good approximation for the lithospheric thickness and the corresponding stretching factor value for the best fit case. However, it must be checked that the zero-line of  $E_1$  lies within the minima region of  $E_2$  contour plot. The above steps can be repeated for different value of crustal thickness.

Synthetic subsidence profiles are generated and used to estimate the suitable best fit lithospheric thickness and stretching factors for a set of crustal thickness values (32 Km, 40 Km and 48 Km). The subsidence profiles were created by randomly generating intervals of subsidence rates for the time period 130 My to present. The first 20 my is assumed to be for initial subsidence by stretching and the remaining 110 My for thermal subsidence. These values are chosen because they are of the same order of magnitude of typical extensional basin systems (Allen and Allen, 2013; Xie and Heller, 2009) and match the primary example system investigated in this paper.

The curve fitting method is applied to a synthetic subsidence profile shown in Figure 5.3 (a). The contour-plots in Figure 5.3(b), 5.3(d) and 5.3(f) show the result of  $E_1$  values for the McKenzie model in the parameter domain space (Lithosphere-Stretching Factor) for 32 Km, 40 Km and 48 Km of crustal thickness respectively. Similarly, Figure 5.3(c), 5.3(e) and 5.3(g) depict the  $E_2$  values for Numerical model comparison with known subsidence curve of Figure 5.3(a). The zero line transient of  $E_1$  values, with varying crustal thickness, for the two models are shown in the Figure 5.3(h) and 5.3(i). It is to be noted that with an increasing crustal thickness, a lower stretching factor is required for the same lithospheric thickness. On the other hand, a higher value of lithospheric thickness is required in the case of a constant stretching factor for increasing crustal thickness.

Furthermore, four synthetic subsidence curves are generated (see Fig. 5.4(a), 5.4(d), 5.4(g) and 5.4(j)) and their subsidence history is compared for the models. The summary of best fit zero curve of  $E_1$  values for both the models for each synthetic curve

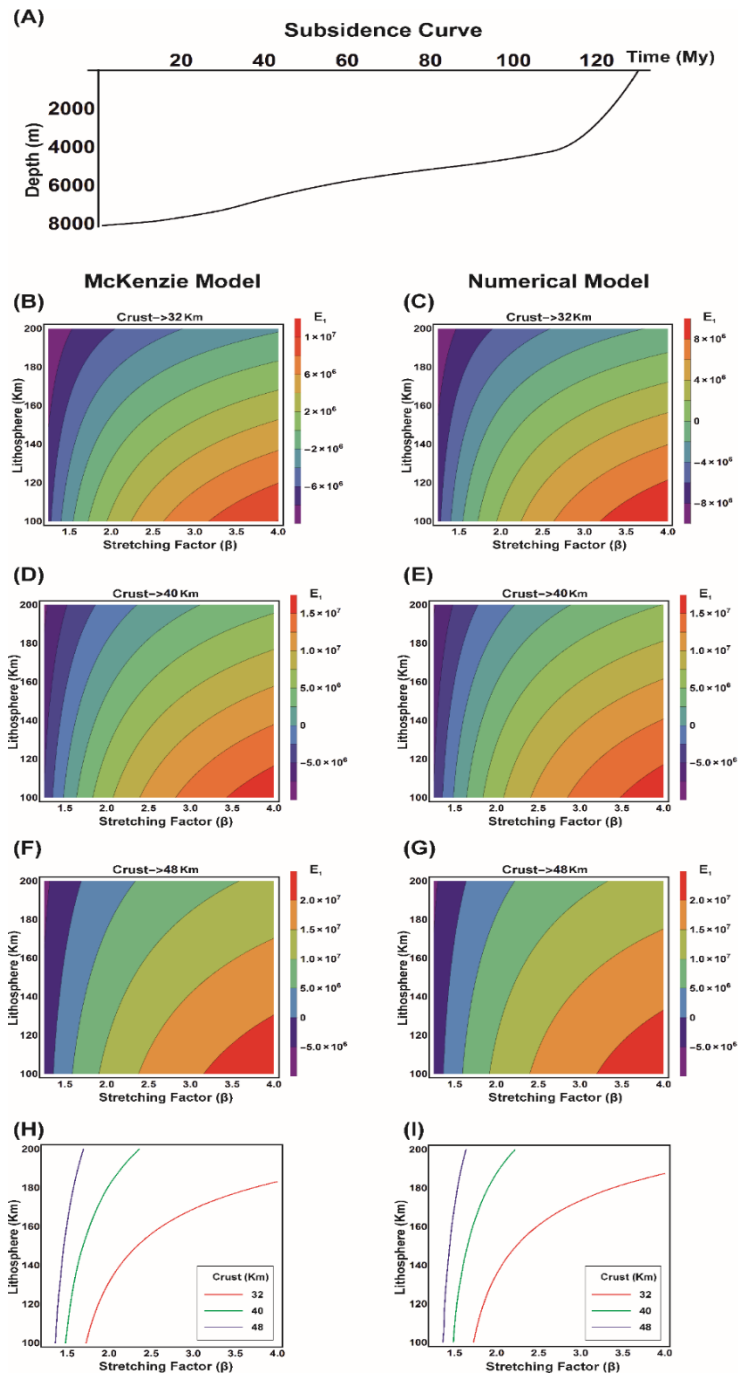


Figure 5.3: Comparison of known subsidence profile with the curves generated from subsidence models are shown in form of Contour-Plot of  $E_i$  values. (a) Shows a synthetically generated subsidence curve of 130 My with first 20 My in the initial subsidence phase. The comparison results for the McKenzie model are shown for crustal thickness (b) 32 Km; (d) 40 Km and (f) 48 Km. The numerical model results of  $E_i$  values for the numerical model is shown for crustal thickness (c) 32km; (e) 40 Km; and (g) 48 Km. The zero-curve for the varying crustal thickness are presented for (h) McKenzie model; and (i) numerical model.

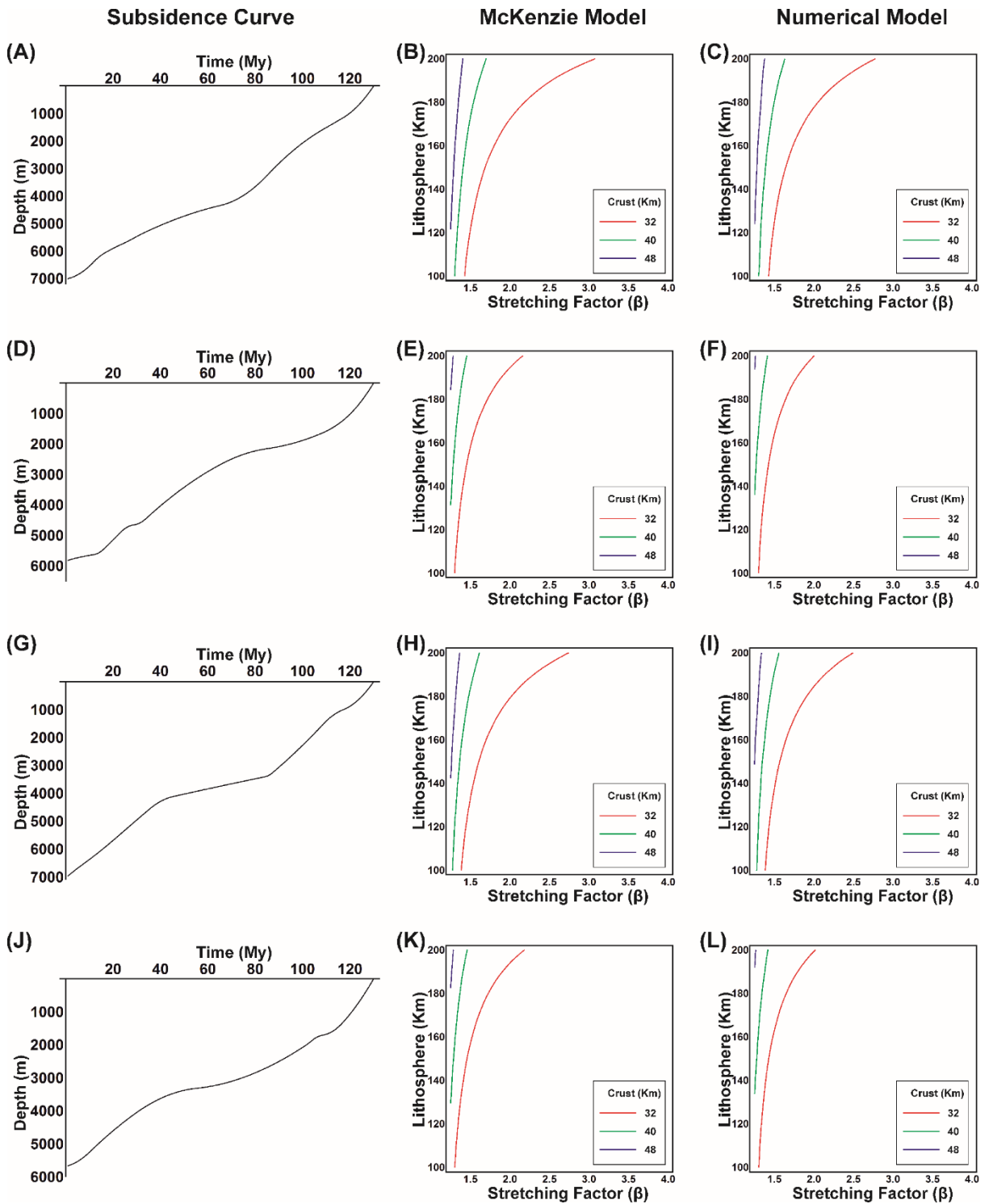


Figure 5.4: Four synthetically generated subsidence curves are shown in (a), (d), (g) and (j). The results on comparison with the McKenzie model gives best fit curve in (b), (e), (h) and (k). The best fit  $E_i$  curves for the numerical model for the four synthetic subsidence curves are presented in (c), (f), (i) and (l) respectively.

is shown in Figure 5.4. It is worthy to note that with the same lithospheric thickness, a higher value of stretching factor is required for fitting the subsidence curve. This is due to the effect of sediments considered during the thermal cooling stage and the different crustal and mantle density considered in the numerical model compared to the McKenzie model.

## 5.4 Case study

In this section, subsidence history from the Campos Basin, offshore Brazil, is used to apply the curve fitting method described in the previous section. Due to its hydrocarbon prospects, the geodynamic evolution and stratigraphy is well studied (Contreras et al., 2010; Guardado et al., 1989; Karner and Driscoll, 1999; Mohriak et al., 1990b). This basin experienced a rapid initial rifting phase (Contreras et al., 2010), thus suggesting that the assumption of instantaneous stretching is valid (Jarvis and McKenzie, 1980).

The formation of Campos Basin is related to the Mesozoic break up of Gondwana and opening of the South Atlantic. The rifting within Gondwana initiated from the southern South Atlantic during Triassic-Early Jurassic (220-200 Ma) and propagated northwards along the North Argentinian margin during the middle Jurassic (180-160 Ma). The intra continental rifting reached the south-eastern Brazilian margin during late Jurassic-Early Cretaceous (140-132 Ma). The geodynamic evolution of the sedimentary basins along the southern Brazilian Atlantic margin are described in five tectonic phases (Cainelli and Mohriak, 1999; Mohriak et al., 2008).

The first is the pre-rift extensional phase that led to the onset of the separation between South America and Africa during the Late Jurassic-Berriasian. The second phase represents the rapid lithospheric stretching and passive upwelling of asthenosphere during the Berriasian to late Barremian. This phase is associated with magmatic activity resulting in tholeiitic basalts flows along the newly formed continental margin. The third phase from Late Barremian to Late Aptian characterises the syn rift sag period and marks the end of extension in the region. Transitional to marine sediments were deposited during this phase. The fourth is the post rift stage from early to mid-Albian which marks the development of mid Atlantic ridge and spreading of the sea floor. The thermal subsidence in the basins were typical of passive continental margins. Carbonates deposited during this phase signifies deepening of the basin. The

final phase stretches from late Albian to Holocene, characterising an increase in the bathymetry with time and resulting in deposition of deep water carbonates.

The subsidence rate for the depo-centre of the Campos basin was recently estimated by a study using backstripping and an inverse numerical modelling method (Contreras et al., 2010). This subsidence rate is used in this study to compare with the thermo-tectonic subsidence generated by the McKenzie model and the numerical model introduced in this study (see Fig. 5.5 (a)). The initial crustal thickness used for forward basin modelling is 32 km based on the result of deep seismic survey in the onshore region (Mohriak et al., 1990a). From the same study, values of sediment, crustal and mantle density were used as 2300 kg/m<sup>3</sup>, 2800 kg/m<sup>3</sup> and 3300 kg/m<sup>3</sup> respectively. The constant for thermal expansion and thermal diffusivity are used as  $3.28 \times 10^{-5} / ^\circ\text{C}$  and  $10^{-6} \text{ m}^2/\text{sec}$  respectively.

The result of comparing the subsidence trends provided from backstripping and the forward subsidence modelling for varying lithospheric thicknesses and stretching factors is shown in Figure 5.5 (b). For 32 Km of crustal thickness, the zero curve of  $E_1$  values vary within 1.25 to 1.8 range. The corresponding lithospheric thickness increases with an increase in stretching factor from 100 Km for 1.25  $\beta$  value up to 200 for 1.8  $\beta$  value. For stretching factor in the range 1.5 to 1.8, the suitable range of lithospheric thickness lies within 180 to 200 Km. Towards higher value of lithospheric thickness, the difference between the best fit curves for the two models increases. The numerical model requires a lesser stretching factor for the same lithospheric thickness for the best fit curve.

In the past, Mohriak et al. (1990b) using visual comparison between the backstripped subsidence and McKenzie subsidence curve estimated the stretching factor to be 1.7 for the Campos basin. This lies within the range given in this study. However, an important distinction between the two comparisons is that thermal subsidence, in addition to initial subsidence, is calculated starting from the rift phase by Mohriak et al. (1990b), whereas, it is estimated from post rift phase in this study.

A major outcome from this study is the estimation of lithospheric thickness together with the stretching factor. It can be noted from the case of 1-D model presented here, a variation in value of lithospheric thickness can change the model output substantially. Thus, the estimation of lithospheric thickness is important for using the

value as model input for further complex and sophisticated 2-D and 3-D thermo-tectonic numerical models. In a comparative study (Xie and Heller, 2009), it has been shown that the subsidence patterns of sedimentary basins follow a pattern for certain tectonic settings. Thus, subsidence history can be used for tectonic interpretation based on subsidence curves.

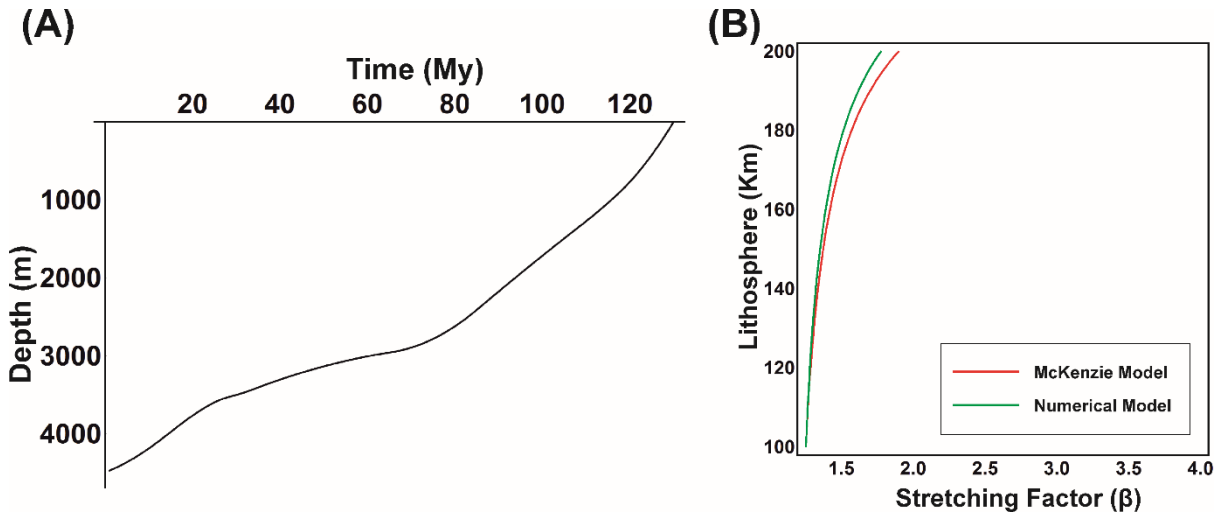


Figure 5.5: (a) Subsidence curve for Campos Basin from Lower Cretaceous to present. The post rift thermal subsidence onsets during the mid-Albian. (b) The best fit zero-curve line for comparison between the known subsidence curve and the curves generated from the models. The crustal thickness is considered to be 32 Km.

## 5.5 Conclusion

A numerical approach to subsidence modelling in an extensional tectonic regime has been presented. The difference between the numerical model developed here and the traditional McKenzie model indicates that taking account of sedimentation during initial and thermal subsidence means that a lower stretching factor is required to explain same level of subsidence. This discrepancy can have implications on basin subsidence histories and heat flow analysis.

Further, synthetically generated subsidence curves are compared with curves generated by the mathematical models using a least squares type approach. This allows estimation of valid combinations of stretching factor, crustal and lithospheric thickness in basin models. If one of these parameters is known, i.e. crustal thickness from seismic reflection analysis, then the other two parameters can be tightly

constrained. This approach is used to fit model parameters to a known subsidence curve calculated from data gathered in the Campos Basin. The results indicate possible ranges of stretching factor values between 1.25 to 1.8 and corresponding lithospheric thickness between 100 to 200 Km for the basin.

## 5.6 Acknowledgement

This project is funded by the Irish Shelf Petroleum Studies Group (ISPSG) of the Irish Petroleum Infrastructure Programme (PIP) Group 4. The ISPSG comprises: Atlantic Petroleum (Ireland) Ltd, Cairn Energy Plc, Chrysaor E&P Ireland Ltd, Chevron North Sea Limited, ENI Ireland BV, Europa Oil & Gas (Holdings) plc, ExxonMobil E&P Ireland (Offshore) Ltd., Kosmos Energy LLC, Maersk Oil North Sea UK Ltd, Petroleum Affairs Division of the Department of Communications, Energy and Natural Resources, Providence Resources plc, Repsol Exploración SA, San Leon Energy Plc, Serica Energy Plc, Shell E&P Ireland Ltd, Sosina Exploration Ltd, Statoil (UK) Ltd, Tullow Oil Plc and Woodside Energy (Ireland) Pty Ltd.

## 5.7 References

- Allen, P.A. and Allen, J.R.** (2013) *Basin analysis: Principles and application to petroleum play assessment*. John Wiley & Sons, Malaysia, 619 pp.
- Burov, E. and Poliakov, A.** (2001) Erosion and rheology controls on synrift and postrift evolution: Verifying old and new ideas using a fully coupled numerical model. *Journal of Geophysical Research: Solid Earth*, **106**, 16461-16481.
- Cainelli, C. and Mohriak, W.U.** (1999) General evolution of the eastern Brazilian continental margin. *The Leading Edge*, **18**, 800-861.
- Chen, L., Zhang, Z., Song, H., Li, F. and Franke, D.** (2013) Numerical modeling of extensional sedimentary basin formation with MATLAB: Application to the northern margin of the South China Sea. *Computers & Geosciences*, **51**, 153-165.
- Contreras, J., Zühlke, R., Bowman, S. and Bechstädt, T.** (2010) Seismic stratigraphy and subsidence analysis of the southern Brazilian margin (Campos, Santos and Pelotas basins). *Marine and Petroleum Geology*, **27**, 1952-1980.

- Guardado, L.R., Gamboa, L.A. and Lucchesi, C.F.** (1989) Petroleum Geology of the Campos Basin, Brazil, a Model for a producing atlantic type basin: part 1. In: *Divergent/passive Margin Basins* (Eds J.D. Edwards and P.A. Santogrossi), pp. 3-80.
- Hantschel, T. and Kauerauf, A.I.** (2009) *Fundamentals of basin and petroleum systems modeling*. Springer Berlin, 475 pp.
- Holmes, M.H.** (2007) *Introduction to Numerical Methods in Differential Equations*. Springer-Verlag New York, New York, 239 pp.
- Hölzel, M., Faber, R. and Wagreich, M.** (2008) DeCompactionTool: Software for subsidence analysis including statistical error quantification. *Computers & Geosciences*, **34**, 1454-1460.
- Jarvis, G.T. and McKenzie, D.P.** (1980) Sedimentary basin formation with finite extension rates. *Earth and Planetary Science Letters*, **48**, 42-52.
- Karner, G.D. and Driscoll, N.W.** (1999) Tectonic and stratigraphic development of the West African and eastern Brazilian Margins: insights from quantitative basin modelling. *Geological Society, London, Special Publications*, **153**, 11-40.
- Kooi, H., Cloetingh, S. and Burrus, J.** (1992) Lithospheric necking and regional isostasy at extensional basins 1. Subsidence and gravity modeling with an application to the Gulf of Lions Margin (SE France). *Journal of Geophysical Research: Solid Earth*, **97**, 17553-17571.
- Kusznir, N.J., Marsden, G. and Egan, S.S.** (1991) A flexural-cantilever simple-shear/pure-shear model of continental lithosphere extension: applications to the Jeanne d'Arc Basin, Grand Banks and Viking Graben, North Sea. *Geological Society, London, Special Publications*, **56**, 41-60.
- Lebedev, S., Adam, J.M.C. and Meier, T.** (2013) Mapping the Moho with seismic surface waves: A review, resolution analysis, and recommended inversion strategies. *Tectonophysics*, **609**, 377-394.
- Lee, E.Y., Novotny, J. and Wagreich, M.** (2016) BasinVis 1.0: A MATLAB®-based program for sedimentary basin subsidence analysis and visualization. *Computers & Geosciences*, **91**, 119-127.
- Lucazeau, F. and Le Douaran, S.** (1985) The blanketing effect of sediments in basins formed by extension: a numerical model. Application to the Gulf of Lion and Viking graben. *Earth and Planetary Science Letters*, **74**, 92-102.
- McKenzie, D.** (1978) Some remarks on the development of sedimentary basins. *Earth and Planetary Science Letters*, **40**, 25-32.



- Mohriak, W., Nemčok, M. and Enciso, G.** (2008) South Atlantic divergent margin evolution: rift-border uplift and salt tectonics in the basins of SE Brazil. *Geological Society, London, Special Publications*, **294**, 365-398.
- Mohriak, W.U., Hobbs, R. and Dewey, J.F.** (1990a) Basin-forming processes and the deep structure of the Campos Basin, offshore Brazil. *Marine and Petroleum Geology*, **7**, 94-122.
- Mohriak, W.U., Mello, M.R., Dewey, J.F. and Maxwell, J.R.** (1990b) Petroleum geology of the Campos Basin, offshore Brazil. *Geological Society, London, Special Publications*, **50**, 119-141.
- Rowley, D.B. and Sahagian, D.** (1986) Depth-dependent stretching: A different approach. *Geology*, **14**, 32-35.
- Royden, L. and Keen, C.E.** (1980) Rifting process and thermal evolution of the continental margin of Eastern Canada determined from subsidence curves. *Earth and Planetary Science Letters*, **51**, 343-361.
- Steckler, M.S. and Watts, A.B.** (1978) Subsidence of the Atlantic-type continental margin off New York. *Earth and Planetary Science Letters*, **41**, 1-13.
- Stephenson, R.A., Nakiboglu, S.M. and Kelly, M.A.** (1989) Effects of Asthenosphere Melting, Regional Thermoisostasy, and Sediment Loading on the Thermomechanical Subsidence of Extensional Sedimentary Basins. In: *Origin and Evolution of Sedimentary Basins and Their Energy and Mineral Resources*, pp. 17-27. American Geophysical Union.
- van Balen, R.T., van der Beek, P.A. and Cloetingh, S.A.P.L.** (1995) The effect of rift shoulder erosion on stratal patterns at passive margins: Implications for sequence stratigraphy. *Earth and Planetary Science Letters*, **134**, 527-544.
- Wangen, M.** (1995) The blanketing effect in sedimentary basins. *Basin Research*, **7**, 283-298.
- Wangen, M.** (2010) *Physical principles of sedimentary basin analysis*. Cambridge University Press, Cambridge, 527 pp.
- Watts, A.B., Karner, G.D. and Steckler, M.S.** (1982) Lithospheric flexure and the evolution of sedimentary basins. *Philosophical Transactions of the Royal Society of London. Series A, Mathematical and Physical Sciences*, **305**, 249-281.
- Wernicke, B.** (1981) Low-angle normal faults in the Basin and Range Province: nappe tectonics in an extending orogen. *Nature*, **291**, 645-648.

**Wernicke, B.** (1985) Uniform-sense normal simple shear of the continental lithosphere. *Canadian Journal of Earth Sciences*, **22**, 108-125.

**White, R. and McKenzie, D.** (1989) Magmatism at rift zones: The generation of volcanic continental margins and flood basalts. *Journal of Geophysical Research: Solid Earth*, **94**, 7685-7729.

**Xie, X. and Heller, P.** (2009) Plate tectonics and basin subsidence history Basin subsidence. *GSA Bulletin*, **121**, 55-64.

## 6 Conclusion

The work presented in this thesis contributes to the development of methods for textural characterisation of sedimentary grains and basin modelling. In the introduction several aims were listed out for the two parts. The conclusions are discussed in the same order as the aims.

**Chapter 2**, concerned with the Mathematica code, provided:

- 1) roundness, angularity, irregularity and circularity as the conventional shape parameters. Mathematically sophisticated parameters such as Fourier descriptors and fractal dimensions were discussed along with a list of basic geometrical shape parameters (aspect ratio, mod ratio, rectangularity, convexity, solidity and compactness) for completeness.
- 2) improvement in the angularity and irregularity shape measurement method. For angularity, a modification of Rao et al. (2002) was suggested using average of 5 highest differences amongst consecutive internal angles of the grain. In the case of irregularity, the shape of a grain is compared with the best fit ellipse to calculate indentations and projections as a measure of irregularity.
- 3) a Mathematica code along with example analysis of loose sediment and this section samples for grain shape measurement. Roundness, angularity, irregularity and circularity and fractal dimension methods implemented here are tested on geometric shapes to assess their efficacy.

In **Chapter 3**, grain shape measurement for a collection of loose sediment samples allowed:

- 4) a selection of roundness, angularity, irregularity, fractal dimension, convexity, solidity and rectangularity as the most relevant shape parameters for textural characterisation of grains. The population level inference regarding relative textural maturity of the samples showed similar trends for all the above selected shape parameters.
- 5) ranking of large populations of grains on the basis of their textural maturity ranking within a given sedimentary environment. Samples within glacial,

aeolian and beach environments showed statistically significant differences amongst themselves. However, fluvial samples did not exhibit significant difference in the population level grain shape distribution.

- 6) discrimination between aeolian samples and the rest (glacial, fluvial and beach). However, there is a significant overlap in characteristics between grains from the glacial, fluvial and beach environment which does not allow for discrimination between these groups in this particular study.

A new methodology for quantitative shape measurement is proposed in **Chapter 4**. In this chapter:

- 7) Inverse Radius of Curvature (IRC) plot was proposed to identify corners in a particle boundary. The IRC plot is also used to measure sharpness of individual corners of a particle.
- 8) a suite of new shape parameters: number of corners ( $\nu$ ), cumulative angularity ( $\alpha$ ), sharpest corner ( $\eta$ ) and straight fraction ( $\phi$ ) were presented for collectively characterising grain boundary in a visually meaningful way.
- 9) the above proposed shape quantification method was applied to a natural dataset to assess their utility in textural maturity analysis and sedimentary environment discrimination. The textural maturity of the samples is in agreement to the analysis done in previous chapter (refer point 5) with existing shape parameters. It is found that aeolian samples can be discriminated from the fluvial, glacial and beach samples using the new shape parameters, however, the absolute discrimination amongst samples from fluvial, glacial and beach is not possible.
- 10) a relationship between the proposed set of shape parameter and the visual perception of a grain boundary is demonstrated.

The next part of the thesis dealing with basin subsidence modelling is covered in **Chapter 5**. In this chapter:

- 1) a 1-Dimensional numerical model for basin subsidence in an extensional setting is presented. This model takes into account the sedimentary cover during thermal subsidence.
- 2) a method to compare and fit forward subsidence model with known subsidence history of a basin is proposed. This curve fitting method is applied to the

synthetic subsidence curves to estimate stretching factor value and corresponding best fit crustal and lithospheric thickness values. The methodology is further applied to the case study of Campos Basin to estimate stretching factor in the range of 1.25 to 1.8 and a corresponding lithospheric thickness of between 100 to 200 Km.